UNIVERSITÀ DI SIENA 1240

Department of Experimental and Clinical Biomedical Sciences

University of Florence

Doctorate in Genetics, Oncology and Clinical Medicine

XXXVII Cycle

Coordinator: Prof.ssa Ilaria Meloni

Identification of novel therapeutic strategies through newly developed *in vivo* Tumor models

PhD Candidate

Michele Martinelli

Supervisor

Annarosa Arcangeli

University of Florence

Co-supervisor

Iacopo Petrini

University of Pisa

Michele Martinelli

Firmato digitalmente da Michele Martinelli
Data: 2024.12.09 17:27:49 +01'00'

Academic Year 2023/2024

Abstract

Preclinical studies are crucial to clinical research, yet 90% of drug candidates fail in trials. Reducing failure rates requires stringent criteria in preclinical settings, including new therapeutic strategies, better models mimicking in vivo cancer characteristics, and reliable Tumor identification and monitoring methods.

This work uses the VevoF2-LAZR-X system, combining photoacoustic and ultrasound imaging, to (a) generate a novel pancreatic cancer (PDAC) model, (b) test an innovative therapeutic strategy, and (c) characterize angiogenesis in an *in vivo* setting. We developed (a) orthotopic xenograft mice models of PDAC using the ultrasound-guided injection of PANC-1 cell line, (b) which are used for testing a bifunctional antibody (scDb-hERG1/β1) combined with different doses of Gemcitabine (sub-therapeutic and therapeutic). Our data show that scDb-hERG1/β1 plus sub-therapeutic gemcitabine has antitumoral effects comparable to therapeutic dose gemcitabine, with increased survival and reduced toxicity.

To better mimic *in vivo* PDAC characteristics, we developed (a) models with co-cultures of PANC-1 and pancreatic stellate cells (RLT-PSC). RLT-PSC contributes to the Tumor microenvironment by supplying nutrients and facilitating metastasis through collagen production. Our models included orthotopic injections of PANC-1, RLT-PSC, and mixed ratios of these cells at different ratio (1:1 and 1:5 PANC-1/RLT-PSC respectively). Ultrasound (US), photoacoustic imaging (PAI), and nonlinear contrast (CE-US) were then performed to compare those models in *in vivo* settings. It emerges that PANC-1/RLT-PSC 1:5 exhibited greater hypoxia and reduced vascular perfusion. Noteworthy, Tumor aggressiveness appeared to increase, as metastasis was found in the liver of these models, in contrast to PANC-1 and RLT-PSC alone where it doesn't occur.

We then move on to (c) evaluating Tumor angiogenesis focusing on colorectal cancer (CRC), whose management has evolved with anti-angiogenesis therapies like Bevacizumab. Using subcutaneous xenografts models, generated by the injection of HCT-116 wild-type (WT) and Bevacizumab-adapted (Beva/A) cell lines, we characterized Tumor volume, oxygen saturation, hypoxia, and perfusion through PAI

and CE-US. The two models, despite the similarities of the expression observed on *in vitro* conditions for the main angiogenetic-related genes, on *in vivo* settings exhibit differences. Although both models displayed similar Tumor growth, HCT116-Beva/A tumors showed higher oxygenation (sO_{2TOT}, sO_{2P}) and lower HIF-1α and VEGF-A levels, but no difference were observed for Hb_{tot}, suggesting more efficient oxygenation despite the same vascular density. From the perfusion analysis, little variation can be assessed, suggesting lower blood flow efficiency in the resistant tumors, supporting variation in the vessels network in the Beva-resistant models. As the hERG1/β1 complex promotes angiogenesis via the PI3K-Akt pathway and VEGF-A secretion, we proceed to test in these two models the impact of scDb-hERG1/β1 in combination with Bevacizumab. This had a much more pronounced effect on sO_{2TOT} and sO_{2P} in the HCT116-Beva/A tumors with both significantly decreasing, thus indicating increased tumour hypoxia due to increased tumour cell death with subsequent abnormal vessels collapse.

This is further supported by perfusion parameters that show the effect of combination treatment in Bevacizumab-resistant tumors. Increased levels of both PE and PI, and reduction in mTT and TTP suggests improved perfusion and blood flow following treatment, possibly as a result of vascular remodelling due to combined inhibition of angiogenesis pathways.

The following review shows the translational value of different advanced imaging modalities, including ultrasound and photoacoustic imaging techniques, to test novel therapeutic modalities in pancreatic ductal adenocarcinoma and colorectal carcinoma, particularly in their treatment-resistant models.

1. Introduction

1.1 Tumor and Preclinical Studies

1.1.1 Overview of Tumors and Public Health Challenges

Cancer is a complex and multifaceted disease that has long been a significant healthcare challenge, affecting millions of individuals worldwide[1]. According to data reported in 2022, an estimated incidence of 19 million new cancer cases were identified, with a mortality rate of 10 million deaths per year. The burden of cancer continues to grow rapidly, with projections indicating that the number of new cases could reach 29.5 million, and the number of deaths could rise to 16.3 million by 2040[2]. According to WHO, the most common types of cancer diagnosed were lung, breast, and colorectum cancer, accounting for 33.5% of total cancer diagnoses. Lung and

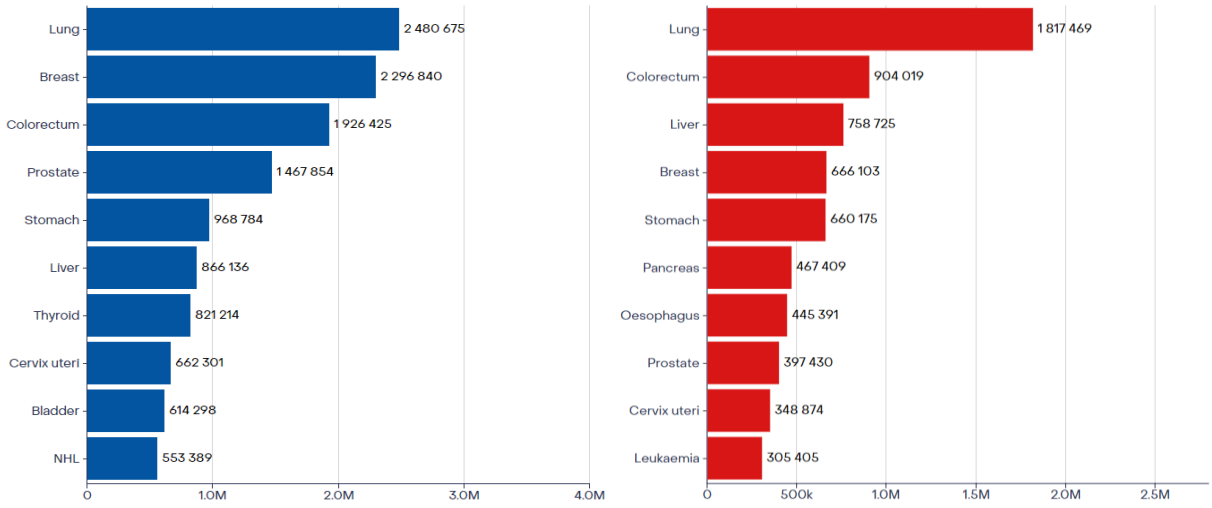

Figure 1 The absolute number of Incidences (blue bar) and mortality rate (red bar) worldwide in both sexes (Globocan 2022, IARC - https://gco.iarc.who.int)

colorectum cancer also retain the highest mortality rate, with a percentage of death up to 70% of all diagnoses. Some tumors are unlikely to be diagnosed at early stages due to lack of screening, such as liver and pancreatic cancer, contributing to the high mortality rates[3,4].

Cancer arises through the development of multiple mutations in normal cells to turn them into cancerous cells. The mutation process involves three categories of external factors: chemical carcinogens, physical carcinogens, and biological carcinogens[5].

- **Physical Carcinogens**. That includes ionizing and UV radiation.
- **Chemical carcinogens.** Asbestos, components of tobacco smoke, alcohol, aflatoxins, and arsenic.
- **Biological carcinogens**. Cancer-causing agents are a result of infections due to some viruses, bacteria, or parasites.

Cancer incidence is higher in older people, and it is due to accumulated exposure for a longer time to risk factors, which are paired with the reduced efficiency of repair mechanisms with aging. Smoking, alcohol consumption, unhealthy diet, and physical inactivity can increase the development and progression of cancer. It has been estimated that 30% to 50% of all cancers could be prevented by modifying or avoiding these risk factors, proof of the importance of public health interventions[6]. Also, early diagnosis is primary in treating cancer properly. Late-stage diagnosis leads to a reduced response to treatment and a lower survival rate. Early detection is essential to improve cancer outcomes by increasing survival rates and reducing the economic burden of the disease. Screening programs that can early diagnose cancer such as mammography for breast cancer or colonoscopy for colorectal cancer, have been effective in reducing mortality from these cancers[7]. Unfortunately, screening programs are not yet available for many cancer types in many countries, especially low-income nations. A correct cancer diagnosis is also crucial for giving the patient appropriate and effective treatment. They usually include surgery, chemotherapy, and systemic therapies like immunotherapy or targeted therapy[8]. Unfortunately, the risk of recidivism and metastasis is still high, mainly due to the genetic heterogeneity of cancer cells which can adapt to the treatment, especially when provided alone and not in combination.

This research concentrates on two deadly types of solid tumors, specifically pancreatic ductal adenocarcinoma (PDAC) and colorectal cancer (CRC). The prognosis and response of PDAC are typically poor compared to traditional therapies, with an overall survival rate that is less than 10% in 5 years. The lack of clear symptoms during the development stage of this malignancy makes it challenging to diagnose and restrict surgical options. Despite the potential for early diagnosis, CRC remains one of the most significant causes of cancer death, with treatment options including surgery and targeted biological treatments. The significance of angiogenesis in developing both neoplasms is undeniable, making it essential to investigate novel therapeutic approaches, such as bifunctional antibodies that can regulate tumor growth and resistance.

1.1.3 *Clinical Features and Progression of Pancreatic Ductal Adenocarcinoma (PDAC) and Colorectal Cancer (CRC)*

Table 1 Comparison between Pancreatic Ductal Adenocarcinoma (PDAC) and Colorectal Cancer (CRC)

Feature	Pancreatic Ductal Adenocarcinoma (PDAC)	Colorectal Cancer (CRC)
Origin	Ductal cells of the pancreas (exocrine)	Epithelial cells of the colon or rectum
Common Symptoms	Abdominal pain, weight loss, jaundice, back pain	Blood in stool, abdominal pain, weight loss, change in bowel habits
Risk Factors	Smoking, chronic pancreatitis, family history, obesity	Age, family history, inflammatory bowel disease (IBD), diet high in red/processed meats
Genetic Mutations	KRAS, TP53, CDKN2A, SMAD4	APC, KRAS, TP53, PIK3CA, MMR genes (MLH1, MSH2, etc.)
Prognosis	Poor prognosis; 5-year survival rate < 10%	Variable prognosis depending on stage; 5-year survival rate ~65% (overall)
Tumor Markers	CA19-9, CEA, CA-125	CEA, CA19-9 (in advanced cases)
Common Metastasis Sites	Liver, lungs, peritoneum	Liver, lungs, peritoneum
Therapeutic Approaches	Surgery (Whipple procedure), chemotherapy (gemcitabine, FOLFIRINOX), targeted therapy	Surgery (colectomy), chemotherapy (FOLFOX, FOLFIRI), targeted therapy (EGFR, VEGF inhibitors)
Screening	No effective screening method for general population	Colonoscopy, fecal occult blood test (FOBT), sigmoidoscopy
Imaging Techniques	CT, MRI, endoscopic ultrasound, PET-CT	Colonoscopy, CT, MRI, PET-CT
Role of Angiogenesis	Angiogenesis plays a role, but PDAC is highly desmoplastic	Angiogenesis is significant, with VEGF pathway being targeted for therapy
Potential for Immunotherapy	Limited success with immune checkpoint inhibitors	Immunotherapy (e.g., checkpoint inhibitors) more promising, especially in mismatch repair-deficient tumors
Incidence	Less common, but highly lethal	One of the most common cancers globally
Age Group	Primarily affects older adults (average age ~70)	Typically affects adults aged 50 and older

1.1.3.1 *Pancreatic Ductal Adenocarcinoma (PDAC)*

Pancreatic Ductal Adenocarcinoma is one of the most aggressive and deadliest forms of carcinoma. If taken alone, it can comprise more than 90% of malignancies of the pancreas. Although not so common as most types of tumors, poor is notoriously the prognosis of PDAC, with its average five-year survival rate below 10%. The asymptomatic course of the disease in the early stages allows tumors to be diagnosed

at later stages due to metastases or invasion of critical structures. That already explains the high mortality rate. The clinical manifestations in an early stage are very unspecific and indefinite; PDAC diagnosing is therefore not easy. Anorexia, abdominal pain, and fatigue are common symptoms for patients. The obstruction of the bile duct by the tumor, particularly in cancers located in the pancreatic head, can lead to jaundice. The early manifestation of PDAC may be due to a sudden appearance of diabetes mellitus, even in the absence of metabolic syndrome, but it is frequently disregarded. More severe symptoms, such as vascular obstruction, epigastric swelling, and nerve infiltration may develop during later stages. These delayed symptoms make it more difficult to detect in advance, thereby making treatment efforts more complicated[9]. Typically, diagnosis involves imaging and biopsy. The first step is often to get an abdominal computed tomography (CT) scan enhanced with contrast, which gives very useful information about the size of a tumor as well as whether it is metastasized. Endoscopic ultrasound (EUS) is also used for its ability to provide superior resolution and fine-needle aspiration, which facilitates histological confirmation. Magnetic Resonance Imaging (MRI) can be useful to enhance the tumor's visibility and determine its association with nearby structures, particularly in situations where vascular invasion is suspected. Where there is a strong familial history of PDAC, or other high-risk features, surveillance with periodic imaging, or endoscopy may be indicated[10]. These features are discussed further in later sections. After diagnosis, staging allows differentiation of prognosis and potential treatment options. The most common staging system for pancreatic ductal adenocarcinoma is the TNM staging. In Stage 0, the tumor is confined only to the pancreatic ducts, whereas in Stage I, it extends more widely and at times progresses to a higher level. During stage II, the tumor may diffuse out of the normal pancreas into the local tissue or lymph nodes but without major vasodilator invasion. The worst are stage III tumors which include ablations of frequent nearby blood vessels or nerves and damage to lymph nodes. Stage IV's disease has advanced and spread to distant organs, escalating the prognosis[11].

Multiple fundamental genetic modifications are responsible for the molecular development of PDAC. One of the earliest and most important events in PDAC development is the presence of mutations in the KRAS gene, which occurs in over 90% of cases. Additional mutations in tumor suppressor genes like TP53, SMAD4, and CDKN2A occur as the tumor metastatically develops. Tumor growth and treatment complications arise from these genetic modifications, which are exacerbated by the resistance of PDAC to conventional therapies[12,13]. Molecular subtyping of PDAC has revealed unique gene expression patterns, which may lead to personalized treatment approaches, although clinical trials are still in progress[14].

1.1.3.2 Colorectal Cancer (CRC)

Colorectal cancer (CRC) is one of the most frequent cancers. It represents the third most frequent tumor overall and the second cause of tumor-related death. Compared to the majority of cancers, a high percentage of patients have benefited from improvement in the prognosis as a result of general screening. At an early stage, the absence of symptoms demands the usage of screening methods like colonoscopy. When symptoms do occur, there are usually alterations in bowel movements such as persistent diarrhea or constipation, and the presence of blood in stool. The disease can also cause unrelated weight loss, fatigue, and abdominal pain as the tumor progresses, especially if it results in incomplete bowel obstruction. Neoplasms that occur in the rectum or left colon are likely to present earlier on account of the smaller diameter of the lumen, whereas those on the right side of the colon may be presented later, often after dilatation has taken place, giving rise to symptoms[15]. Right-sided colorectal carcinoma is generally confined to the ascending colon and the proximal two-thirds of the transverse colon. The left-sided colorectal cancer starts in the descending and sigmoid colon as well as the distal one-third of the transverse colon. These tumors also possess some specific histological peculiarities. Right-sided CRC often originates from sessile serrated adenomas or mucinous adenocarcinomas, while in the case of left-sided CRC, it usually appears as tubular and villous as typical

adenocarcinoma. Because of its polypoid morphology, the left-sided tumors are easily visible during colonoscopy at the beginning of carcinogenesis. In contrast, right-sided CRC has a flat morphology that is more challenging to identify[16]. Together with the discovery of better treatment methods, these facts have contributed to the decline in mortality rates for CRC despite the increase in incidence rates seen in most developed countries. Most diagnoses are made through one of several effective screening methods: the Fecal Occult Blood Test (FOBT), Fecal Immunochemical Test (FIT), or one of several forms of direct visualization such as colonoscopy. When abnormalities are identified after the screening, they are subordinates to histological confirmation through biopsy during hematological examination of the colonoscopy. Imaging studies for the size of malignancy are usually done by CT scans of the abdomen and pelvis or MRI scans in cases of rectal cancer regarding metastases. PET scans may be done for assessment of far-off metastases in advanced disease.

Treatment strategies are heavily influenced by staging following diagnosis. A staging scheme called TNM is employed to classify CRC. At Stage 0 the tumor is confined to the innermost layer of the colon or rectum membrane and hasn't invaded even deeper layers; it is also known as carcinoma *in situ* or intramucosal carcinoma (Tis). In Stage I the growth has invaded deeper layers of the wall of the colon or rectum but has not extended to nearby lymph nodes. Thus, in the second stage of malignancy, it has invaded through the outermost layer of the colon or the rectum, sometimes advancing into adjacent tissues, though not reaching lymphatic nodes. In Stage III, the tumor has spread to regional lymph nodes, although it has remained local, not distal to the body. Stage IV presents a dramatically poorer prognosis if the neoplasm has spread to other organs like the lungs or liver[17].

CRC arises from a well-established series of genetic mutations that convert normal epithelial cells into cancer cells at the molecular level. Most pathways involve changes in the APC gene, a tumor suppressor that plays an important part (but not only) in cell growth and adhesion regulation. The development often begins with the loss of APC's function, especially in familiar adenocarcinoma polyposis (FAP) cases, where germ-line

mutations predispose the development. Also, somatic mutation has been found in more than the 80% of sporadic CRC[18]. Genetic changes in KRAS and TP53 are also common throughout the disease process. Genetic mutations in KRAS could be present in 40% of cases and could predict resistance to certain targeted therapies. The DNA mismatch repair (MMR) deficiency leads to microsatellite instability (MSI) accounting for a share of about 15% of deaths by carcinogenesis. The hereditary Lynch syndrome-related tumors are frequently found in individuals with MSI-high CRC, but it is also observed in at least 20% of sporadic colonic cancers[19]. Another important aspect to be considered is angiogenesis, which is crucial in progression and metastasis. One of the major pro-angiogenic factors whose level is usually higher is vascular endothelial growth factor (VEGF), which leads to poor prognosis. Usually, the level of VEGF is increased at the advanced stages. It is more prominent in the higher and more serious stages of development, especially in stages III and IV. Because of this insufficient blood supply, the tumor becomes hypoxic during these stages, acting as a strong stimulant for the synthesis of VEGF. However, this hypoxia-induced synthesis of VEGF through hypoxia-inducible factors (HIF), inducing neovascularization, has again facilitated the proliferation, invasion, and metastasis of the tumor. In addition, VEGF is commonly connected to bigger tumors, better tumor growth, and higher metabolic risk during these later stages[20].

1.1.4 *Preclinical tumor research*

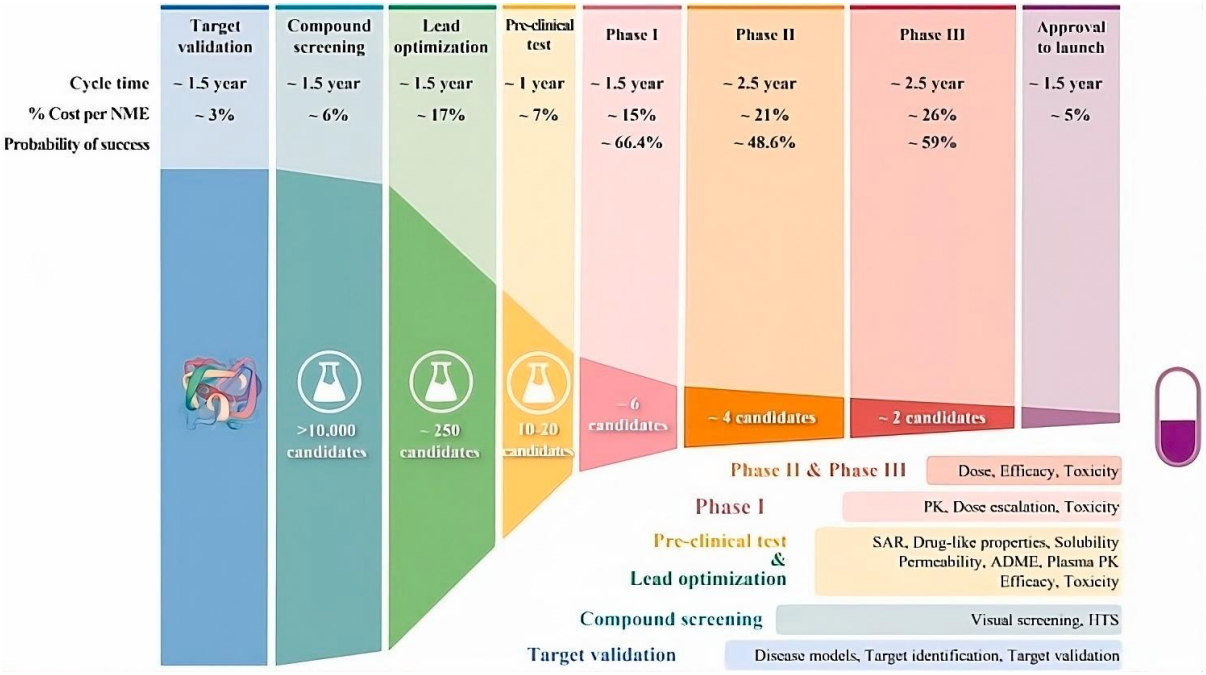

Figure 2 Failure rate at each stage of the drug development and discovery process [21].

The development of new drugs is a long and high-risk process that often faces significant challenges during the clinical trial phase. Considering all the studies, great effort and substantial investment are required, which takes 10 to 15 years and 1.5-2.0 billion USD to bring a single new drug to be approved for clinical use, the failure of 90% of drug candidates at this stage is a major concern for the pharmaceutical industry[21–23]. The high failure rate in clinical trials is largely attributed to the limited predictive value of preclinical studies, which often fail to accurately identify the drug target or predict the human response; approximately nine out of ten drug candidates fail during phase I of clinical trials, highlighting the need for bridging the gap between the preclinical setting and clinical application[24]. Most of the drugs that failed during the development were safe and effective in preclinical animal studies but did not translate into humans as lack of clinical efficacy and toxicity explain respectively 50% and 30% of the reasons that drugs do not overtake the clinical phase[21]. Before treatment may be effectively developed, a novel molecular target must first be truly validated in

human disease; biological differences between *in vitro*, animal models, and human disease may make it difficult to determine the molecular target's function, as the models become more complex. Faced with these challenges, re-evaluating current preclinical approaches, and developing more predictive models is crucial to improving the success rate of drug development[25]. The failure rates highlighted in the preclinical setting might be reduced by adopting strict criteria during drug development. Because of that, there is a need not only for the development of new drugs that can address unmet medical needs but also for more efficient and predictive preclinical models that can identify the right drug candidate for clinical trials. In addition, in clinical and preclinical settings, innovative approaches for monitoring and characterizing tumor and drug response are needed to better predict and achieve therapeutic strategies.

1.1.5 Innovative Therapies: New Approaches in Cancer Treatment

The search for new and effective treatments for cancer is likely to be easily applied in the clinic and is one of the big challenges of modern oncology. Traditional methods of treatment, such as radiotherapy, and chemotherapy have limitations and do not always bring an expected therapeutic effect, particularly in aggressive cancers like Pancreatic Ductal Adenocarcinoma (PDAC) and Colorectal Cancer (CRC). Surgery is presently the most effective modality of treating solid tumors in the clinic; however, it is often suffering from incomplete tumor resection, which may further lead to the risk of tumor recurrence, and it needs to be combined with radiotherapy and/or chemotherapy[26]. Besides, these two standard treatments show suboptimal efficacy with severe side effects and are often accompanied by the development of drug resistance. This is one of the major issues in cancer therapy, which significantly limits effectiveness and highlights the need for the development of innovative treatment strategies that can target cancer cells more specifically[27]. Combinations of multiple chemotherapeutic agents are being tested to overcome resistance mechanisms and

improve outcomes[28].

In PDAC we can see how FOLFIRINOX[29,30], a combination of 5-fluorouracil, irinotecan, oxaliplatin, and leucovorin, has increased overall survival compared to single-agent gemcitabine[31]. This combination has also been followed in the treatment of acute lymphoblastic leukemia; adding Hyper-CVAD-cyclophosphamide, vincristine, doxorubicin, and dexamethasone-with methotrexate and cytarabine improved the survival rate of the patient[32]. Further, in those patients who have locally advanced or metastatic pancreatic ductal adenocarcinoma (PDAC) who are generally healthy, FOLFIRINOX is the first choice. In patients with poor performance status, single-agent gemcitabine should be given. First-line platinum-based chemotherapy can also be applied in carriers of BRCA1/2 with very far-advanced disease[12]. In these patients, where there is no evidence of disease progression following a minimum of four months with first-line platinum-based chemotherapy, Olaparib maintenance can be considered. In cases of unresectable, locally advanced diseases, chemotherapy may be followed by consolidation chemoradiotherapy in the event of no evidence of progressive disease. It generally includes second-line polychemotherapy with fluoropyrimidines not given during first-line treatment in patients with good performance status (Karnofsky > 70%). One liposomal formulation of irinotecan (MM-398) was approved as nanomedicine in 2015 for use in combination with 5-fluorouracil (5-FU) plus folinic acid in the treatment of metastatic PDAC as a second-line treatment[29,30].

While surgery is considered the mainstay of treatment in the early stage of CRC, the approach in an advanced stage of the disease is to combine targeted therapies in addition to surgery.

Fluoropyrimidines, including 5-fluorouracil or capecitabine, combined with oxaliplatin or irinotecan (FOLFOX or FDIRI), comprise the backbone chemotherapeutic agents in CRC. Bevacizumab and cetuximab are two representative targeted therapies that are more commonly used in combination with these; Bevacizumab improved survival in advanced CRC by targeting angiogenesis[33–36]. Metastatic CRC patients can undergo surgical treatment. In the absence of surgical resection, chemotherapy alone or with

the addition of targeted therapy-including Bevacizumab, Cetuximab, or Panitumumab-remains the standard of care. Vaccines such as pembrolizumab and other immune checkpoint inhibitors are approved for immunotherapeutic use in those whose tumor is either MSI-H or dMMR. These therapies offer promising outcomes. In addition, the use of liquid biopsies for non-invasive monitoring of colorectal cancer recurrence and resistance is now under evaluation [37,38].

Despite all these efforts, severe side effects due to a lack of specificity to cancer cells and tumor resistance still represent major limitations. Such challenges have forced to find new approaches, including, immunotherapy, personalized medicine, and nanomedicine, which gives better specificity with a reduction in the side effects and fight against drug resistance in tumors of different types [39,40]. Approaches have been developed under nanomedicine to improve the bioavailability and specificity to tumor cells. Due to possessing certain physicochemical properties different from their bulk counterparts, including nanoscale size and large surface area-to-volume ratio, nanoparticles could be developed to take advantage of such properties to enhance drug delivery, extend blood circulation time, and increase specificity through engineering their surface with targeting moieties[41]. Gold and polymer-based nanoparticles like PEGylated liposomes have shown great therapeutic potential in preclinical studies. Engineered gold nanoparticles GNS@CaCO3/Ce6-NK act not only as drug delivery systems but also as photosensitizers and photothermal therapeutic agents[42]. PEGylated liposomes encapsulating doxorubicin have also demonstrated better therapeutic efficacy compared to the free drug in breast cancer, showing an advance in accumulation to the tumor site due to the enhanced permeability and retention effects[43]. The therapeutic effects of small-size nanoparticles are based on their physical properties allowing passive accumulation in tumor tissue through the enhanced permeability and retention effects, due to the leaky vasculature and lymphatic draining[44]. Nevertheless, passive targeting has the potential to result in multidrug resistance (MDR) and presents a significant challenge in terms of regulation.

By contrast, active targeting involves the mark of specific overexpressed receptors on tumor cells, enhancing the absorption of the targeted cells[45].

Currently, because of their specific interaction and high affinity to target antigens, antibodies are the most applied ligand for active targeting[46,47]. These proteins consist of two different regions: one variable region, Fab-a fragment, responsible for antigen binding, and one crystallizable fragment, Fc, which mediates interactions with the immune system, such as phagocytes or components of the complement system. Such consideration has led to the possibility of using antibodies in two different ways: first, as immunoconjugates linked either to a drug or a nanoparticle; second, in a naked form, as in the case of monoclonal antibody therapy. The former allows for a higher drug concentration in the tumor site, as they are capable of directly targeting antigens of cancer cells[48]. EGFR-targeting monoclonal antibodies conjugated to gold nanoparticles and encapsulating gemcitabine have been reported to significantly inhibit tumor growth in head and neck squamous carcinoma cells[49]. Alternatively, naked antibodies could be administered to the patient using an approach based on stimulating the immune attack against the tumor, the so-called immunotherapy. They can act either by marking directly cancer cells, making them more visible for immune system cells-opsonization-or by blocking immune checkpoint inhibitors such as PD-1, CTLA4, and LAG3, which suppress the T cell response against tumor cells[50]. FDA-approved different types of antibodies, including Trastuzumab and rituximab, mostly in combination with chemotherapy as a first-line treatment option[51–53]. The antibodies have been tested not only for their direct cytotoxic effects but also for their ability to inhibit angiogenesis-an important step for the growth and metastasis of most tumors. Bevacizumab was the first antiangiogenic drug, a humanized monoclonal antibody against VEGF-A, clinically for more than 15 years; it is approved to be used in combination with chemotherapy in the treatment of metastatic colorectal cancer[35]. Nowadays, new antibodies with unique characteristics, such as bispecific antibodies, are currently being explored for their ability to simultaneously target multiple antigens,

enhancing therapeutic efficacy, and reducing the likelihood of tumor escape variants. Diabodies are smaller than full-length antibodies because they do not have the Fc domain but do have two single-chain variable fragments (scFBV) able to bind two different antigens simultaneously. Smaller formats may increase tissue permeability and decrease circulation time, which would minimize the risk of side effects and increase selectivity toward tumor sites. New classes of antibody formats have been added, and advances in antibody engineering and conjugation techniques have widened the therapeutic scope of antibodies, opening new perspectives in targeted cancer immunotherapy[54,55].

1.1.6 Animal experimentation in preclinical tumor research

The use of animal models in preclinical settings has been a crucial aspect of drug validation and therapeutic development, as they provide insight into the underlying biological pathways and physiology that can be extrapolated to human disease. However, the predictive validity of these models has been questioned due to significant discrepancies between animal responses and human outcomes in clinical trials[56]. Therefore, a proper selection of appropriate animal models is essential to ensure successful translation into the clinical setting.

For improving the translational value of animal models, certain key factors need to be considered. Several determinants including proper experimental design, execution of studies, reporting of experiments, and animal model validation are fundamental for guaranteeing the predictive power [57,58]. General validation is the core of translational research, which considered several aspects such as face, predictive, and target validity[59,60]. Face validity refers to the degree to which the animal models capture the phenotypic manifestation of human disease. In this regard, the alignment of drug response and clinical outcomes between the animal and human pathology is also crucial, referred to as predictive validity. Additionally, it must be known if the animal model's molecular and cellular mechanism truly reflects the specific situation that

occurs in human disease, which is often referred to as target validity; this ensures that the therapeutics targets identified are relevant to the human condition.

Despite validated animal models are fundamental for proper screening of therapeutic drugs, their effectiveness in predicting the clinical outcome is often hampered by a poor experimental design. Moreover, the inconsistent laboratory conditions and stress-induced responses in animal subjects can further complicate the reliability of these models, highlighting the necessity for rigorous standardization and comprehensive methodological frameworks in their application to translational medicine[61]. First discrepancies which can lead to an overestimation of the efficacy of the therapeutic candidates rely on the time course and the patterns of drug administration. In animal models, the treatment route starts early during the disease, in contrast to the clinical situation often characterized by late-stage diagnosis and treatment onset. The efficacy of the treatment regimens could also be overestimated if potential side effects are ignored, making it impossible to administer equivalent doses in a clinical setting.

Reproducibility represents another key issue, as slight variations in experimental conditions can significantly affect the outcome. Age, gender, and health status of the animals can influence treatment response and must be properly considered as they need to match closely the clinical condition under study[62,63]. Reporting of all these characteristics is essential to allow interpretation and comparison of results across different studies, especially if slightly different models have been used. For instance, a tumor xenograft model with different cell lines of the same cancer type, using the same drug and animal model with standardized characteristics mentioned above, can provide a more comprehensive evaluation of the drug potential.

Ethical considerations also play a significant role in preclinical research. Since ethical reasons push to minimize the number of animals used, appropriate statistical design and analysis are key requirements to maximize the informative value of each

experiment and avoid underpowered or biased studies[64]. Unfortunately, also if all these points are currently considered, a high degree of failure is encountered, and that relies on the complexity of the models used.

To overcome that situation, a combination of different or highly sophisticated models can help to fit well in with clinical conditions. Humanized mouse models are highly valuable when transplanted with human tissues or cells. Depending on the specific disease and research, various types of humanized models and strains of mice are used.

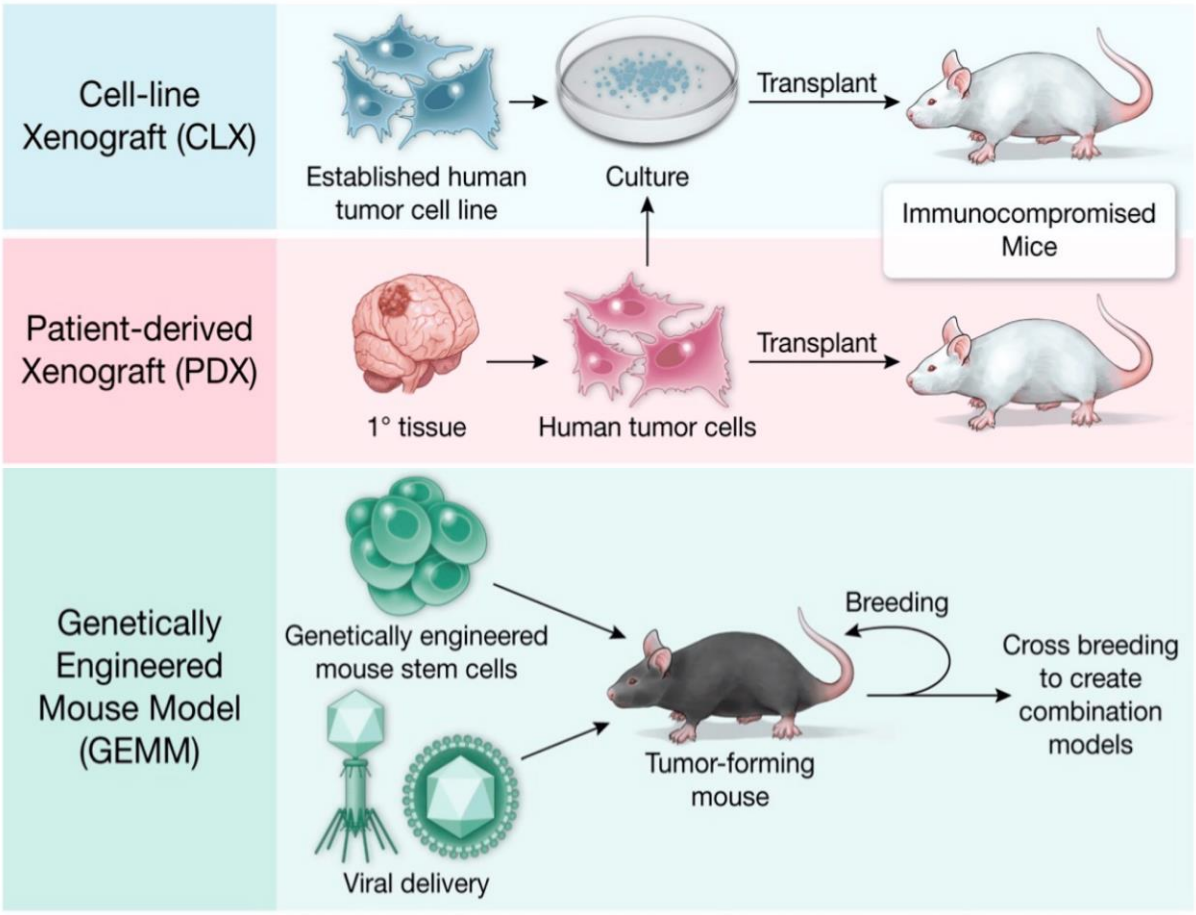

Figure 3 Different types of preclinical mouse model (Hicks, W.H.; Bird, C.E.; Traylor, J.I.; Shi, D.D.; El Ahmadieh, T.Y.; Richardson, T.E.; McBrayer, S.K.; Abdullah, K.G. Contemporary Mouse Models in Glioma Research. Cells 2021, 10, 712. https://doi.org/ 10.3390/cells10030712)

The most frequently employed ones include human tumor xenografts and 'humanized' mice, resembling human immune systems.

Human tumor cell-derived xenograft immunodeficient mice are widely used as they are relatively easy to establish and inexpensive, however the lack of appropriate human stroma and immune cells results in a poor predictive value[65]. In addition, despite orthotopic implant of tumor cells showing higher similarity to the original tumor, subcutaneous xenografts are still the most used models due to their technical simplicity[66]. To overcome these limitations, new orthotopic xenograft models that better mimic the tumor microenvironment are now emerging[67–69].

In contrast to cancer cell line-based xenografts, genetically engineered mouse models (GEMMs) that express human disease-related genetic alterations can recapitulate more accurate histopathological and molecular features of the disease. Higher heterogeneity and spontaneous acquired metastatic properties make them a more predictive model in preclinical screening, although their development is generally more time-consuming and challenging. Only a limited number of genes can be suitably engineered, and this poses a significant constraint on the range of diseases that can be effectively modeled, limiting the translational application of these genetically engineered systems[70]. Another type of advanced model is the so-called patient-derived xenograft (PDX), which involves the direct engraftment of surgical tumor specimens into immunocompromised mice. These models retain the original sample's heterogeneity and stromal components, with a high similarity to the tumor found in patients. The tumor, which can be collected from the metastatic site or primary, not only preserves the molecular features of the donor patient but preserves also the resistance profile and response to treatment, thereby improving the prediction of clinical outcome. In fact, those studies have shown a good correlation between response in PDX models and clinical responses observed in patients. As seen for the other models, PDX show disadvantages as well, including their low success rate in engrafting and expanding, high costs, and the inability to study immune system effect on tumor growth and therapy due to the need for immunodeficient mice[71,72].

1.1.7 Preclinical Approaches for Monitoring and Characterizing Tumor and Drug Response

Characterization of tumor and drug response is crucial for improving the prediction and success of therapeutic strategies in cancer treatment. In preclinical settings, drug efficacy has been mainly evaluated through the assessment of tumor growth inhibition in animal models, but this method is limited in predicting clinical outcomes. Caliper measurement is a conventional method, but it has limitations in accurately reflecting tumor volume, especially for irregular-shaped tumors. The estimation of the volume is obtained by measuring the width and the length of the tumor, and by applying the following mathematical formula: Volume=width² x length/2[73]. Unfortunately, that procedure doesn't fit well for irregular-shaped tumors, leading to highly variable results and a lack of reliability. This provokes, to achieve statistical significance for drug evaluation, a large number of animals to be used, raising the overall cost and an increase in the time required for preclinical studies, also limiting the possibility to test a large number of drug combinations.

New approaches can not only reduce the variability for tumor growth monitoring but also can provide more comprehensive information about tumor biology. In spontaneous and transplanted tumor models primary tumor growth and metastatic spread can be challenging to obtain accurate measurements[74]. In that context, non-invasive imaging techniques such as magnetic resonance imaging (MRI), positron emission tomography (PET), and optical imaging provide additional information about tumor microenvironment and response to therapeutics[75]. These imaging modalities can quantify various biological processes, such as tumor perfusion and metabolic activity, either directly or indirectly. For instance, MRI techniques like Dynamic Contrast-Enhanced MRI (DCE-MRI) provide direct measurements of blood flow and vascular permeability, while optical imaging methods, such as fluorescence imaging and Near-Infrared Spectroscopy (NIRS), can indirectly assess perfusion by measuring

parameters like oxygen saturation, which are influenced by blood flow. Such insight may reflect treatment response more accurately than traditional methods, thereby enhancing the predictive power of preclinical models and facilitating the transition to clinical applications[76,77]. Optical imaging techniques like fluorescence and bioluminescence imaging, monitor the expression of reporter genes in tumor cells and represent a powerful tool for tumor growth evaluation on real-time and longitudinal assessment of treatment response. The need for tumors that express genetically encoded fluorescent or bioluminescent probes is a major limitation of this, which is time-consuming for spontaneous tumor models. Advances in the hybrid imaging approach, combining anatomical imaging like MRI or CT with functional imaging like PET or single photon emission computed tomography (SPECT), have shown the ability to provide comprehensive information about the tumor microenvironment, including tumor vasculature[78]. While PET's spatial resolution of 5–10 mm is relatively high and may limit the ability to resolve fine microvascular details in preclinical settings, the complementary use of high-resolution modalities like MRI or CT helps overcome this limitation by providing anatomical precision. Additionally, in preclinical studies, alternative PET systems with enhanced spatial resolution (e.g., micro-PET) are often used to achieve finer detail suitable for evaluating small structures, such as tumor vasculature and heterogeneity.

Furthermore, the integration of innovative imaging technologies enables real-time monitoring of tumor dynamics and immune responses, thereby assisting in the identification of non-invasive biomarkers that predict therapeutic efficacy, particularly in the context of immunotherapy[79]. Combining mathematical modeling with imaging techniques can further enhance the understanding of tumor behavior and treatment outcomes, as these models utilize patient-derived data to forecast tumor progression and therapeutic response, which is essential for tailoring personalized treatment strategies[80,81]. In the next chapter, we will focus on innovative preclinical approaches, especially by focusing on Ultrasound and Photoacoustic systems which are nowadays very promising to address these challenges.

1.2 Molecular imaging

In the contemporary healthcare system, medical imaging occupies a crucial position in many medical contexts, as it validates, confirms, and records the progression of numerous conditions and the efficacy of treatments. The technique recreates various images of the inside of the body, offering a deep physiological and anatomical evaluation that can be essential for both routine physiological research and clinical practice. Despite anatomical imaging providing a variety of clinical information like diagnosis, surgical guidance/follow-up, and treatment monitoring, several limitations can be noted, from early detection of tumors to a lack of deep molecular characterization[82]. On account of that, a field of medical imaging known as molecular imaging is rapidly evolving, which expects to overcome the limitations offered by classical methodology. The field of molecular imaging is advancing quickly and holds great potential in precise targeting and accurate quantification in a range of applications including screening and early identification of diseases, personalized therapy, and more prompt monitoring of treatment progress[83]. The ability to observe and quantify how biological and cellular processes function *in vivo,* without the need for surgical procedures or biopsies, makes the field of non-invasive imaging techniques incredibly valuable. This breakthrough in medical advancements not only leads to an increase in patient care, as invasive procedures are employed much less frequently but also provides more confident and continuous data that can be used to monitor therapy response [84–87]. For this purpose, therapeutic monitoring can be more efficient by using specifically designed imaging agents, which mark specific molecular targets and can be fundamental for direct monitoring of treatment efficacy, anticipating morphological and anatomical changes that can occur too late[88].

Several types of techniques have been widely used in clinical settings including ultrasound (US), CT, MRI, and especially magnetic resonance spectroscopy (MRS), PET, and SPECT. Those last two mention techniques (PET, SPECT) are the most diffuse in clinical settings, based on the use of radionuclide agents specific to a target of interested[89,90]. Both approaches provide deep penetration and enable sensitive whole-

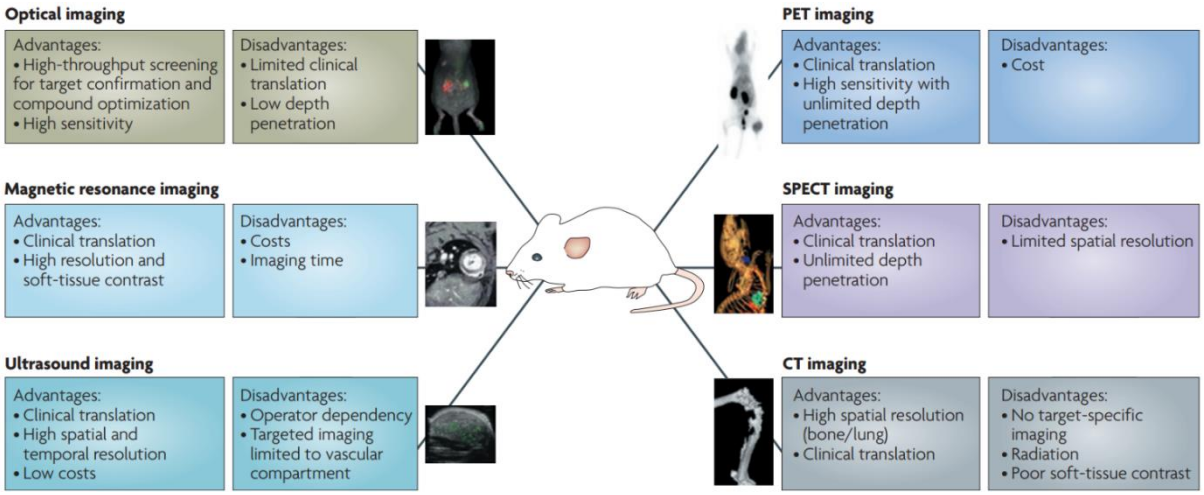

Figure 4 Techniques used for molecular imaging (Willmann, J., van Bruggen, N., Dinkelborg, L. et al. Molecular imaging in drug development. Nat Rev Drug Discov 7, 591–607 (2008). https://doi.org/10.1038/nrd2290).

body imaging of molecular targets and processes. Despite these similarities, both have slight differences in principles and clinical applications. PET relies on radiolabeled imaging agents to target specific molecular processes, which emit positrons that annihilate electrons, producing gamma rays detected by PET scanners to create images. Fluorodeoxyglucose F18 is the radioactive tracer mainly used in these situations, which acts as a glucose analog to localize the tissues with altered glucose metabolism as tumor sites. Accordingly, the main application is for revealing and monitoring tumor progression and treatment response, eventually by showing also metastasis.

Otherwise, SPECT uses gamma-emitting radioisotopes and a gamma camera with a collimator to enable the collection of tomographic images. Despite being less specific than PET, SPECT is the most common nuclear medicine modality in clinical settings

especially for detecting thyroid cancer, neuroendocrine tumors, and diagnosis in the field of cardiology and neurology.

The reason for their large use in clinical settings can be appreciated by looking at their high sensitivity, ranging from 10^{-10} to 10^{-12} M, combined with an extensive depth for tissue imaging which led to accomplishing quantitative analysis for molecular events. Unfortunately, PET and SPECT lack anatomical context which represents a main limitation of this kind of analysis. Additionally, the spatial resolution of PET may not be sufficient for the precise delineation of small structures, such as skin tumors, where fine anatomical details are critical for accurate diagnostics and treatment planning. Not only that, the main concern with the use of technologies relies on the use of radio nuclides, which provide ionizing radiation representing a limitation for safety. In general, subjects exposed cannot exceed 5 mSv (millisieverts) per year, limiting the number of scans they can have[91]. On account of that, Ultrasound imaging is now emerging as a new potential tool that can overcome limitations provided by those technologies.

1.3 Ultra-High Frequency Ultrasound (UHF-US)

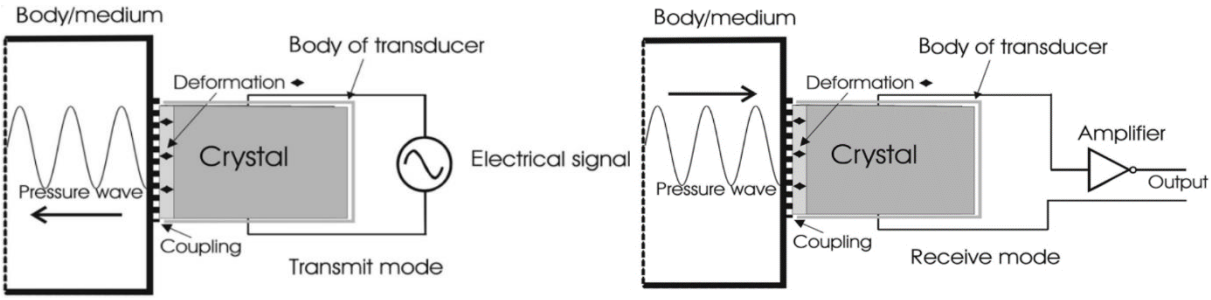

Figure 5 Schematic representation of the production and reception of ultrasound waves (Magee P. Essential notes on the physics of Doppler ultrasound. BJA Educ. 2020 Apr;20(4):112-113. doi: 10.1016/j.bjae.2020.01.003. Epub 2020 Feb 20. PMID: 33456938; PMCID: PMC7807840.)

Ultrasounds are mechanical waves that propagate through, allowing the generation of real-time, high-resolution images of internal structures within the body. This imaging modality has become increasingly prevalent in both clinical and preclinical settings due to its numerous advantages, including the absence of ionizing radiation, relatively low cost, and portability. The main frequency used in this setting ranges from 1 to 50 MHz, with higher frequencies providing improved resolution despite the reduced depth of penetration.

For the production and reception of ultrasound waves, piezoelectric transducers are employed[92]. Firstly, they generate short-pulsed ultrasound waves relying on the electrical currents that cross the transducer itself and direct the high-frequency sound waves into the body. Once they receive the signal, the transducer relies on the so-called piezoelectric effects, by converting the reflected echoes into electrical signals depending on mechanical pressure, which is converted as a potential difference, and finally can be processed into an image[93]. Depending on the type of sound echo, the transducer captures its intensity and transforms it into 1-D, 2-D, or 3-D images that the user can render and inspect.

Ultrasound has become a core imaging modality for preclinical studies, allowing real-time visualization of anatomical structures, as well as the assessment of physiological parameters such as blood flow, tissue perfusion, and cardiac function. The most used

frequencies in clinical settings are between 1 to 15 MHz, providing lower resolution compared to preclinical imaging where higher frequencies in the 20 to 50 MHz range are applied, enabling higher resolution imaging of small animal models and *ex vivo* samples[94]. The echoes received by the ultrasound probe are transformed first into electrical signals and then into a 2D digital image. From the intensity and the time of the returning echoes, various information can be extracted, such as the depth and size of the imaged structures. Several visualization modes are available for the detection of the echo graphic signal, known as a mode. The most common are:

- **A-mode (amplitude mode).** Represent the amplitude of the echo in a single dimension, showing the depth and intensity of the structures along a single line within the body.
- **B-mode (Brightness mode).** Convert the echo amplitude into a two-dimension image, where the brightness of each pixel is proportional to the echo intensity. The process of creating B-mode images involves methodically merging numerous A-mode (1-D) scans into a single 2-D image, in which each pixel's intensity is determined by the amplitude of the accompanying ultrasonic beam.
- **M-mode (Motion mode).** Record the motion of moving structures over time, such as the heart valves or arterial walls, by displaying the changes in the position of the echo signals along a single scan line over time[92,95].

1.3.1 Ultrasound Eco-Structure: Tissue Characteristics in Tumor Imaging

Ultrasound imaging relies on the physical interactions of sound waves with biological tissues, which influence the resulting image's appearance and quality. Soundwaves are mainly characterized by frequency (ξ), velocity (v), wavelength (λ), and intensity (J), which impact the resolution and penetration depth. In that case, a distinction is made between two different kinds of spatial resolution: axial and lateral. Axial resolution concerns the ability to distinguish between structures lying behind each other along

the direction of the ultrasound waves. The frequency plays a major role in axial resolution, as the distance between the structures must be $\Delta z \geq \lambda/2$ to visualize distinct structures. On the other hand, lateral resolution concerns the ability to visualize different structures that are located next to each other at the same depth. Lateral resolution is always inferior to axial resolution, depending on the following equation $\Delta x = 3*\lambda$ Various physical phenomena occur such as:

- **Reflection and transmission**. When an ultrasound wave encounters a boundary between two different tissues, part of the wave is reflected and transmitted through. The quantity of reflection depends on the difference in acoustic impedance between the two tissues. If the difference is large, more sound is reflected. The reflection coefficient (R) at the boundary between two media with impedances Z_1 and Z_2 is given by: $R=(Z_2-Z_1/Z_2+Z_1)^2$, where Z is computed as Z=rad(E*D), D is the density, and E represents the elasticity of the medium.
- **Scattering.** When sound waves reflect, they don't encounter a perfectly smooth surface but rather irregular surfaces. That causes a random scatter in several directions, enabling the imaging of tilted boundaries. The width of the reflection cone (the area over which the sound is reflected) increases as the wavelength decreases and the roughness of the surface increases. Due to that, higher frequency and rougher surfaces cause the sound waves to scatter more widely.
- **Diffraction**. Sound waves are diffracted when they travel through apertures, barriers, or other obstructions. A shift in the sound wave's direction is a component of diffraction. A greater degree of diffraction (sharpness of bending) results from increasing wavelength λ, and vice versa.
- **Absorption and attenuation.** As the sound wave intensity J penetrates in the medium, it decreases exponentially with the depth of propagation with the formula $J(x)=J_0\exp(-\mu x)$, whereas μ is the attenuation coefficient, which

depends on absorption and scattering, and x is the depth. This means that higher-frequency ultrasound is useful for providing more detailed imaging, as it offers improved axial and lateral resolution. However, the tradeoff is that higher frequencies also experience greater attenuation, corresponding to higher absorption and scattering within the medium, which results in reduced imaging depth[95–97].

As the ultrasonic beam interacts with biological tissues, it engages with different materials that have different acoustic properties such as density and stiffness. This allows for discrimination between various regions of the body, as most tissues have different acoustic impendence, leading to different reflections of the sound waves and therefore different brightness of the echo graphic image, a phenomenon known as echogenicity[98,99]. This characteristic defines the brightness of a specific region of interest of the image in comparison with the surrounding tissues, due to the different reflections of the ultrasonic wave which can be different by observing different images. Structures that appear to have the same echogenicity are defined as isoechoic, conversely, hyperechoic structures appear brighter compared to the surrounding tissues, while hypoechoic structures appear darker. The type of tissue encountered will also determine the fate of the ultrasound beam: some tissues will absorb the beam, while others will transmit and reflect it[100]. Unfortunately, some tissue characteristics can introduce artifacts to the generated images, especially when the beam interacts with bone, liquids, or gas-filled spaces. The bones and calcifications display a high degree of acoustic impedance that leads to a high reflection of the ultrasound beam, which provokes a generation of a shadow cone underneath the bone, affecting the visualization of the structures located behind[101]. Gas-filled space such as air can interfere with the propagation too, a phenomenon known as reverberation. That is why the transducer is not directly in contact with the body, but an interposed gel between the body and the probe is fundamental for providing the image itself while avoiding artifacts[102]. By doing that, the acoustic impedance of the transducer is like

that of the tissue being examined allowing the minimization of the reflection. Also, liquids such as water or blood, due to their low acoustic impedance, appear to be anechoic region. Moreover, the anatomical structure behind liquids can appear hyperechoic compared to the surrounding tissues, and that is mainly due to the lack of absorption of the ultrasound beam of the fluid[103]. Focusing on the preclinical setting, we can easily distinguish several tissues with this premise, also tumors can be identified and rapidly evaluated as they have a different echo structure.

1.3.2 *Perfusion Analysis: Insights into Tumor Vascularization and Function*

As seen in the previous chapter, ultrasound imaging is a valuable method for obtaining real-time information about tissues, organ status, and tumor evaluation. Not only can it provide anatomical details, but recent advancements in perfusion analysis have expanded the capabilities of the technique. Ultrasound can be used to image the perfusion in two ways: using Doppler and with the more recent development of contrast-enhanced ultrasound (CE-US), which relies on microbubbles as contrast agents[104,105]. Imaging perfusion and its changes can provide crucial information and quantification as volume blood flow, vascular permeability is altered in many physiological and pathological conditions. Especially in oncology, these techniques are now emerging for the study of angiogenesis, whose intricate vessel network patterns can help characterize and monitor tumor progression and response to the treatment.

1.3.2.1 Doppler Imaging: blood flow dynamics

Normal blood flow displays an intrinsic scattering due to the properties and the size of the red blood cells. With traditional B-mode ultrasound, this scattering effect is not visible, and blood flow appears black as the acoustic impedance is lower compared to the surrounding tissues. However, the motion of the blood can be traced by using a different approach, based on the Doppler effect. This occurs when a wave encounters

a moving object, causing a shift in the frequency of the reflected wave. It is defined with the following equation: $\Delta F=2*f_0*V*\cos\varphi$, where ΔF is the frequency shift, V is the speed of the moving object, f_0 is the original frequency and φ is the angle formed by the incident wave and the moving object. In our case, we need to consider that blood cells in the flow act as independent moving scatters, resulting in a series of frequency shifts mainly derived from the complexity of the hemodynamics and the interaction with the vessel walls. To obtain a single representative frequency shift for all the blood flow, the Fourier transform is applied, which decomposes all the frequencies and provides the Doppler spectrum. By analyzing the Doppler spectrum, signals regarding frequency fluctuation and flow direction, that is flowing toward or away from the probe, are collected throughout time. The Doppler echo devices can determine the angle of incidence of the ultrasound pulse to the blood flow, and also the speed starting from the frequency shift according to the Doppler equation above; that is indicative of the laminar or turbulent flow condition, useful to study the hemodynamic status of the vessels[106,107].

The techniques for receiving and sampling the Doppler signal can be continuous emission or pulsed emission, depending on the specific application. In continuous emission, the US probe emits a continuous signal, and the echo is then received by an additional probe. The use of two different probes allows us to detect the velocity of the blood but not the depth of the vessels. In pulsed Doppler we avoid that problem, as the probe both emits and receives the signal; by timing the emission and reception of the pulses, we can add to the velocity information the B-mode view of the area under analysis and so depth information.

Based on the visualization of the flux, we can apply color and power Doppler techniques. Color Doppler uses the detected Doppler shift to display the direction and relative speed of blood flow in a color-coded overlay on the B-mode image, providing a visual representation of the blood flow patterns. When the flux is moving towards the transducer it is represented in red, and vice versa in blue. The speed is also correlated to the intensity of the color, with fast flow in bright red/blue and slower flow

in darker colors. Power Doppler, on the other hand, does not show the direction of flow but instead provides a detailed map of the relative energy or power of the Doppler signals, which is indicative of the total amount of blood flowing through the region of interest. This technique is mainly used for the visualization of low-flow-tiny vessels, where color Doppler usually fails. Besides all these used, the Doppler technique has some limitations when dealing with regions of slow blood flow, large tissue motion and/or low hematocrit percentage[108]. For this purpose, the use of contrast agents emerged to overcome these issues.

1.3.2.2 Nonlinear Contrast Imaging: Enhancing Perfusion Visualization

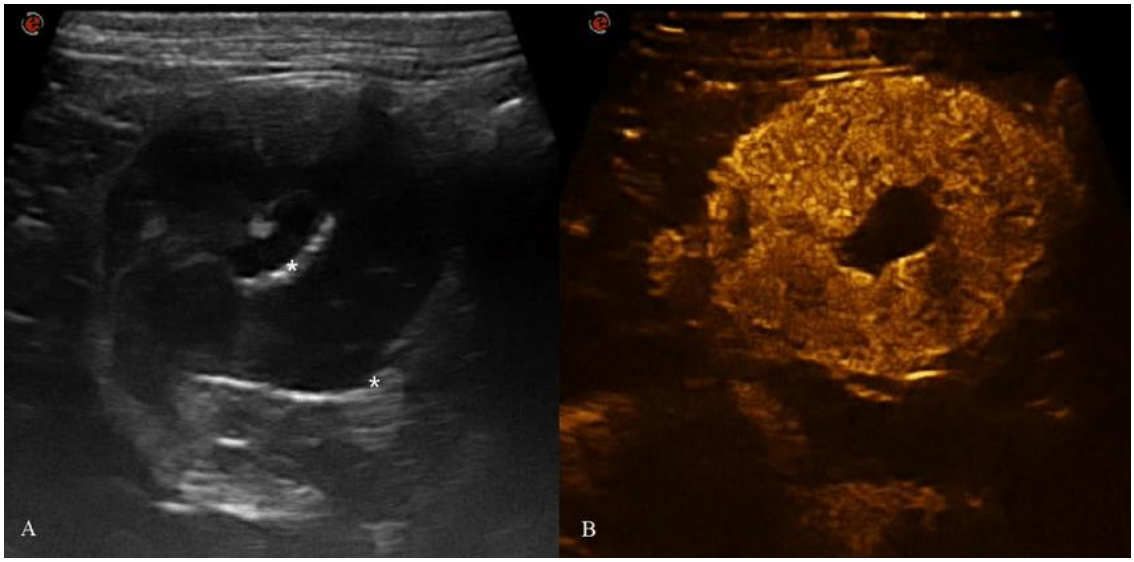

Figure 6 Ultrasound B-mode (A) and Nonlinear contrast imaging for perfusion evaluation Feline gastric high-grade lymphoma (HGAL) ((Simeoni, Francesco & Terragni, Rossella & Rubini, Giuseppe & Tamburro, Roberto & Signore, Francesca & Falerno, Ilaria & Aste, Giovanni & Russo, Marco & Mastromatteo, Giovanni & Vignoli, Massimo, B-Mode and Contrast Enhanced Ultrasonography Features of Gastric Inflammatory and Neoplastic Diseases in Cats. Animals. 10. 10.3390/ani10081444.).

Though flowing in arteries down to arteriolar and venular size can frequently be seen and characterized with Doppler, small vessels cannot be detected using B-mode scanning. Doppler is unable to detect tissue perfusion when blood flow velocity approaches that of tissue, which is at a rate of 1 cm/s[109], as happened also in tumor

conditions.

This problem is avoided using microbubbles, which offer a blood flow indication that is

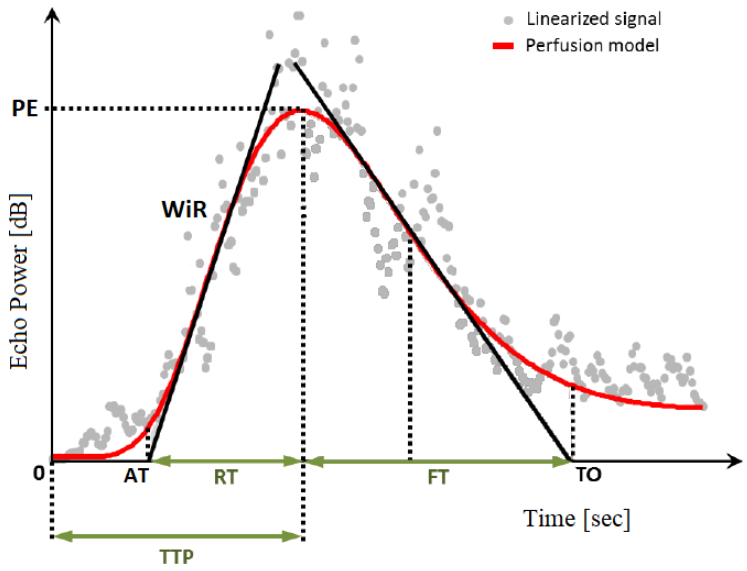

Figure 7 Time-intensity curve representing the perfusion parameters (Simeoni, Francesco & Terragni, Rossella & Rubini, Giuseppe & Tamburro, Roberto & Signore, Francesca & Falerno, Ilaria & Aste, Giovanni & Russo, Marco & Mastromatteo, Giovanni & Vignoli, Massimo, B-Mode and Contrast Enhanced Ultrasonography Features of Gastric Inflammatory and Neoplastic Diseases in Cats. Animals. 10. 10.3390/ani10081444.).

velocity independent[110]. These microbubbles are gas-filled particles of 1-10 micrometers in diameter, stabilized by a shell of phospholipids or albumin. Microbubbles respond non-linearly to the same ultrasonic energy that tissue does, on average, in a linear manner. When the ultrasound waves hit the microbubbles, they undergo compression, followed by an expansion during the refractory phase of the acoustic wave. This results in a non-linear response of the microbubbles, as the expansion is greater than the compression. By doing that, they generate harmonic frequencies of the fundamental, emitted originally by the transducer, which can be recognized and separated from the linear tissue signal by applying a specific frequency filter. Thus, contrast-enhanced ultrasound imaging using microbubbles allows to detect and map microcirculation in the tissue, that couldn't be visualized by Doppler alone. Although we can observe microcirculation, spatial resolution is limited, making it

impossible to discriminate individual capillaries. The signal which came from this technique is proportional to the microbubble concentration and thus to the blood volume passing through the region of interest[111].

After the injection of a bolus of microbubbles, the signal intensity in the specific region of interest can be plotted against time, allowing the analysis of blood perfusion parameters such as:

- **Peak enhancement (PE)**. It is the maximum signal intensity observed in the region of interest, which reflects the maximum blood volume passing through that area.
- **Time to peak (TTP)**. Time from the start of bubble injection to peak enhancement. Can provide information regarding the complexity of the vasculature as more complex structures tend to reach peak intensity later.
- **Mean transit time (mTT)**. Average time of the microbubbles to transit the region of interest.
- **Perfusion index (PI).** Is the maximum area under the curve divided by the mean transit time. It gives a quantitative measure of blood flow as the ratio of blood volume to speed.
- **Wash in rate (WiR)**. Slope of the curve during the initial rise of the signal, reflecting the rate of blood flow.
- **Wash out rate (WoR)**. Slope of the curve during the signal's decay, reflecting the blood flow rate out from the region of interest.

These perfusion parameters can be used to differentiate normal from pathological tissues, and several studies have demonstrated their usefulness in oncological imaging, as in the diagnosis and characterization of tumors and angiogenesis[66,77,112–115].

1.4 Photoacoustic imaging (PAI)

Photoacoustic imaging (PAI) represents a biomedical imaging method that concurrently exploits both optical and acoustic concepts for the visualization of the anatomy and physiological function of biological tissues, and it is a hybrid technique based on the photoacoustic effect. The setup of the PAI system comprises a pulsed light laser source, an ultrasound transducer for acoustic signal detection, a signal amplification with digitization component, and a system to simultaneously record the ultrasound B-mode and the photoacoustic component for data acquisition and image representation. This technique uses a short pulse of light that would be delivered to the biological tissue by a laser. The energy is converted to thermal energy in its interaction with the light-absorbing molecules, called chromophores, in the tissue. Another great advantage of the methodology is the use of non-ionizing radiation; hence, the procedure is safe and non-invasive for biomedical imaging. The whole procedure can be outlined as follows:

1. The target tissue is irradiated by a short-pulsed laser (~10ns) of a wavelength ranging from 600 to 1400 nm.
2. Photons penetrate the tissue, where they are absorbed by endogenous or exogenous chromophores.
3. The transformed optical energy can either be partial or complete into heat energy; therefore, the temperature rises locally and temporarily.
4. The heat-induced thermoelastic expansion of the tissue results in a temperature rise of less than 0,1K.
5. This thermal expansion causes a local pressure increase, generating acoustic pressure waves.
6. The low-amplitude acoustic waves are detected and converted into three-dimensional, high-resolution images by the ultrasound transducer.

PAI is particularly effective because it utilizes the optical absorption properties of endogenous chromophores in the tissues, such as hemoglobin, melanin, and lipids, allowing visualization of anatomical structures and physiological functions deep within biological tissues. This technique has been used in a wide range of biomedical applications, including cancer research, immunology, neurology, and monitoring of blood oxygenation[116–118]. PAI showed a promising ability in delivering simultaneously anatomical, functional, and molecular contrasts using a single modality. Due to its label-free nature, it offers a promising option for *in vivo* imaging, providing detailed tissue information in a non-invasive manner[119].

The penetration depth of this technique relies on the deposition of adequate photon energy within the tissues, which in turn depends on the optical properties of the tissues themselves. Specifically, the ability of tissues to absorb or scatter light can diminish the efficacy of this technique as the light propagates through the tissue. Initially, the technique was applied to study small animals, but it has since been extended to analyze larger tissues, including the human body and primate brain. The clinical application of this new technique, with its high spatial resolution and sensitivity, would primarily the endoscopic areas, where, compared to the instruments currently in use, could bring a superior quality definition and offer high-resolution imaging, also in three dimensions. Rather than competing with MRI or PET, PAI should define new operational fields more closely aligned with traditional optical imaging modalities, offering superior and powerful quality in resolving tissue and disease biomarkers[120–123].

1.4.1 *Contrast agents*

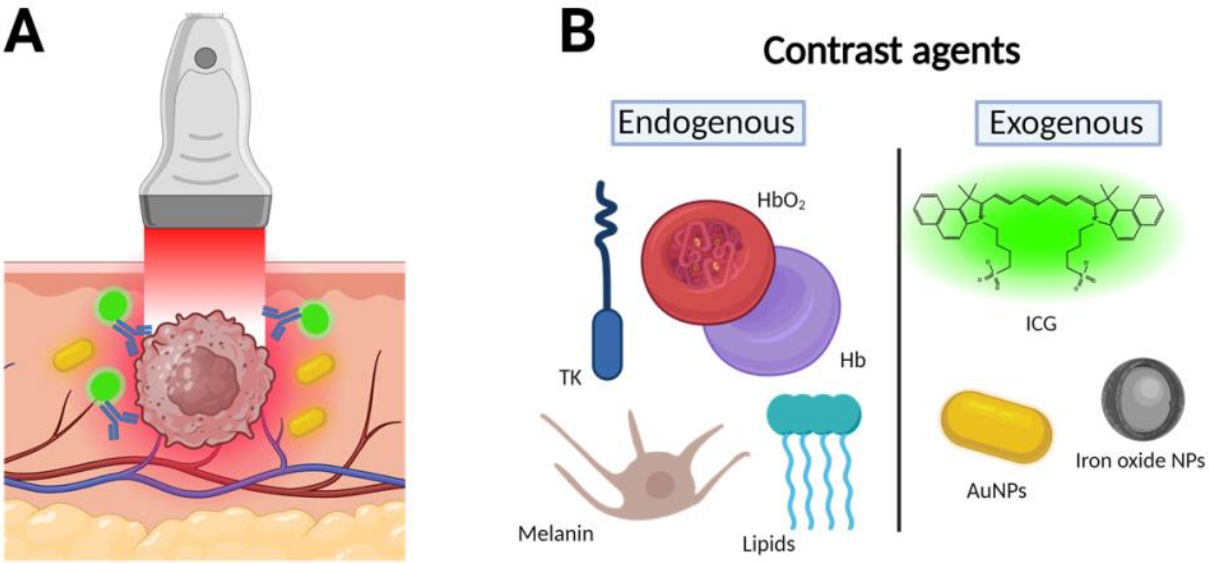

Figure.8 A) Photoacoustic imaging uses a transducer to generate pulsed laser light that is absorbed by chromophores. This absorption causes thermal expansion, creating acoustic waves that are detected and used to reconstruct high-resolution images. This system provides insights into tissue composition and structure. Chromophores can serve as contrast agents and are classified as either endogenous (i.e. melanin, lipids, oxy- and deoxy-hemoglobin) or exogenous (i.e. ICG and nanoparticles).

As in any imaging technique, the contrast agent aims to sharpen the definition and resolution with which otherwise unappreciated morphologically or biochemically diverse elements can be distinguished. Photoacoustic is no exception, being able to make use of endogenous and exogenous agents[124]. The first group of chromophores includes hemoglobin (Hb), melanin, lipids, and collagen. These chromophores are naturally present in tissues, providing complete confidence in their qualitative and quantitative composition. Hemoglobin is the most significant endogenous chromophore at wavelengths less than 1000 nm. At physiological concentrations, the absorption coefficient of both deoxygenated and oxygenated hemoglobin at these wavelengths is higher than that of other chromophores found in the tissues of various organs, such as lipids, water, and elastin[113]. For this purpose, PAI can be used to track hemoglobin concentrations in and around tumor masses, resulting in a very useful tool

to check hypoxic/necrotic areas and consequently angiogenesis. Additionally, the technique has demonstrated its capacity to visualize the growth of the larger arteries and veins associated with the tumor[125]. PAI technique has been employed also to study hypoxia in tumors that are often linked to malignancy and resistance to therapy comparing the PA signal strength of HbO_2 and Hb in patients with cancer. Gerling et al.[126] reported the development and evaluation of a combined photoacoustic imaging and high-frequency ultrasound approach. Assuming that cellular hypoxia serves as a marker of aggressiveness in various solid tumors and therefore an important parameter to monitor, the researchers demonstrated the feasibility and reliability of this bimodal imaging system in detecting tissue oxygenation in live murine models, reflecting how the system can be used for the identification of hypoxic tissue regions, potentially providing both anatomical and functional insights into the growth and treatment response of various neoplasms. Other application of endogenous chromophores can be linked to the use of melanin, which has been studied in the monitoring of the tumor growth in patients with melanoma and also to detect skin melanoma[127]. Another branching is the expression of angiogenic factors, resulting in altered vascularization, leading to the generation of hypoxic/necrotic areas, which are well-known features of tumors.

All of these substances exhibit optical absorption capabilities in the NIR (near-infrared, wavelength spectrum) region, which is between 600 and 900 nm. This spectrum provides the largest depth of penetration, reaching up to several centimeters.

Since not all biomolecules have a characteristic optical absorption spectrum, endogenous contrast can provide access to a restricted range of biological processes. For this reason, a wide range of exogenous agents, such as organic dyes, metal nanostructures, and fluorescent proteins, have been thoroughly investigated for contrast-enhancing approaches. Exogenous molecules, such as antibodies and peptides, offer advantages in imaging studies, particularly for pathological tissues like cancer, where endogenous chromophores alone are insufficiently sensitive. They have been developed taking into account the same NIR as the endogenous contrast agents,

to keeping the detection of PAI system. Many are the contrast agent suitable for PAI, both organic and inorganic[124]. The non-toxicity and biodegradability of organic contrast agents are their best quality and advantage. The combination of nanoparticles with nano systems exhibits important and very advantageous characteristics, such as mechanical flexibility and surface chemistry, which can be modified to optimize their effectiveness in clinical and preclinical applications. As example, Angiostamp800 is a novel photoacoustic organic contrast agent that targets the αvβ3 integrin, which is overexpressed on tumor cells during angiogenesis[128]. It has been evaluated in various animal cancer models and demonstrates tumor-targeting specificity. Another contrast agent, ICG, is a dye-based agent capable of producing high-intensity photoacoustic signals when used in combination with other materials like polyethylene and nano-graphene oxide. Targeted photoacoustic imaging using agents like ICG-RGD, which combines ICG with an integrin-binding moiety, can improve detection specificity. While organic contrast agents have been developed, inorganic agents like gold nanoparticles are increasingly used for photoacoustic imaging due to their favorable properties[129,130].

1.4.2 Preclinical applications

Photoacoustic imaging has attracted particular interest due to its potential to provide noninvasive, multiparametric information about tumors. Several studies have presented the use of PAI in the characterization of preclinical tumor models, and to assess therapeutic responses [131,132]. The possibility of visualizing vasculatures, oxygen saturation levels, and expression of molecular biomarkers in tumors using photoacoustic techniques translates into important information concerning tumor biology and therapeutic response. The early detection of tumors presenting high-resolution three-dimensional images of zones of accumulation of chromophores is possible because of the fast thermal response of acoustic waves. Recent advances in PAI have pushed its limit toward multispectral techniques that are able to detect several chromophores present in the tissue. Moreover, since the hardware components are shared between the ultrasound and photoacoustic imaging

modality following a common signal detection regimen, PAI can be combined with US imaging. This will further enable the extraction of morphological, functional, and molecular information on tissues. Applications that so far have been developed for PAI will include the study of tumor vasculature, monitoring therapeutic response, and the visualization of molecular targets in murine models of tumors[133–135]. The use of small animal models aligns well with these procedures, as photoacoustic imaging offers sufficient penetration depth and excellent spatial resolution down to several tens of micrometers. While the depth of imaging is comparable to other optical techniques, what sets PAI apart is its ability to combine optical and acoustic signals, allowing for deeper tissue penetration and higher sensitivity. Furthermore, photoacoustic imaging enables the concurrent monitoring and quantification of multiple metabolites by scanning two or more wavelengths for each tissue slice. The acquired data can be used to generate a final 3-D volume with a spatial localization of chromophores, providing anatomic, molecular, and functional imaging in real time. Furthermore, employing color Doppler or power Doppler modes—which are frequently employed in pre-clinical and clinical diagnostics—US imaging can also identify tumor vascularization. When adopting dual-wavelength (750/850 nm) scanning, in vivo ultrasonic and photoacoustic imaging (US-PAI) may detect endogenous metabolites like deoxyhemoglobin and oxyhemoglobin as well as fine inner organ structure more effectively than optical fluorescence imaging. Thus, the combined application of US-PAI constitutes a unique instrument for tracking tissue vascularization and oxygenation in subcutaneous malignancies[126,136]. Recent studies have focused on the combination of US-PAI to assess *in vivo* angiogenesis[125,137].

1.4.2.1 Angiogenesis evaluation

Angiogenesis is a physiological process that consists of the formation of new vessels from the pre-existing vessels, representing a critical event for several biological processes that include wound healing and restituting the blood supply to the tissues after an injury or ischemia. The original identification of angiogenesis has linked this

process with tumor growth[138,139]. Tumors are composed of cells with higher proliferation rates compared to normal cells, which means that they soon exhaust the available nutrition and oxygen, thus rendering their environment hypoxic. The thereby created hypoxia stimulates neovascularization, resulting in increased delivery of nutrition and oxygen. Therefore, the association of angiogenesis with aggressive tumor growth and metastasis has long been presumed, whereby new blood vessels may provide pathways that facilitate the entry of tumoral cells into the bloodstream. Several modes of angiogenesis have been implicated in tumor progression:

- **Postnatal angiogenesis**. Mediated by mobilizing circulating endothelial progenitor cells toward the tumors, promoting the formation of new vessels.
- **Sprouting angiogenesis**. Endothelial cells form new vasculatures under the stimulation of growth factors by the tumors, such as VEGF.
- **Vessel co-option**: The tumor used the existing vessels and did not need further vascular proliferation.
- **Vasculogenic mimicry.** Tumor cells mimic endothelial cells, forming functional vessel-like structures.
- **Lymph angiogenesis.** A newly formed lymphatic vessel could allow metastasis to occur in tumors.

The quantification of angiogenesis has thus turned out to be one of the major areas of inquiry while undertaking tumor research and treatment. Imaging techniques such as ultrasound, non-linear contrast, and photoacoustic imaging have been used in measuring and assessing angiogenesis. Most of these studies reported that these methods are adequately sensitive in the detection and quantification of tumor-associated angiogenesis, although the validation of these methodologies remains severely problematic.

Merging information both from oxygen delivery and perfusion, these advanced imaging techniques can provide a comprehensive evaluation of the angiogenic process, supporting the development of more effective therapeutic strategies.

Table 2 Overview of the models, results, and validation methods used in several studies. The table lists the reference, mouse model type, and the findings, indicating whether the photoacoustic imaging or nonlinear contrast ultrasound systems were validated.

REFERENCE	MODELS	FINDINGS/VALIDATION
Zhang et al. [140]	Subcutaneous/Orthotopic xenograft PC3 (Prostate cancer)	**Tumor size is a better indicator of BB2r-uptake in both mouse models, with significant positive correlations observed between tumor volume and BB2r-uptake as well as tumor perfusion.**
Liu et al.[141]	C57BL/6 J mice/apolipoprotein E gene knockout	**Enhanced PA signal primarily reflected inflammation and angiogenesis, correlating with αvβ3-integrin's function.**
Kuczynski et al. [142]	CB17 SCID mice; Orthotopic xenograft Hep3B-hCG (Hepatocellular carcinoma)	Identifies vessel co-option as a significant mechanism of acquired resistance to the anti-angiogenic therapy sorafenib in hepatocellular carcinoma (HCC); **no correlation of tumor perfusion with IHC/IF has been reported.**
Zhou et al.[143]	BALB/c nude mice; Subcutaneous xenograft C4-2 (Prostate cancer)	**Histological analysis confirmed the normalization of vascular functions after DC101 treatment.**
Pan et al.[144]	Athymic Nude-Foxn1^{nu}; Subcutaneous injection of growth factor (FGF-2 and heparin in Matrigel)	αvβ3-targeted GNBs for sensitive and specific angiogenesis imaging; **no correlation of PA with IHC/IF has been reported.**
Maximilian M. Menger et al[145].	CD1 mice (model for bone regeneration)	sildenafil acts as a potent stimulator of angiogenesis and bone regeneration in atrophic non-unions. **Callus tissue display an association on the increased number of CD31-positive microvessels and higher oxygen saturation.**
Okumura et al.[146]	C57BL6/J and B6N-Tyrc-Brd/BrdCrCrl albino; Lewis lung carcinoma (LLC) cell allograft model	PA coupled with ICG revealed that VEGF-trap effects could be predicted in terms of Tumor permeability; **no correlation of PA with IHC/IF has been reported.**
Xu et al.[147]	BALB/c nude mice; Subcutaneous B16 (Melanoma)	Mapping vasculature with PA on melanoma cell line on *in vivo*; **no correlation of PA with IHC/IF has been reported.**
Weinman et al.[148]	P8 Mice models	Active angiogenesis has been observed in the postnatal mouse brain, identifying perfused and nonperfused vessels, endothelial tip cells, and filopodia using IB4 staining, EB perfusion, and stereological analysis; **no correlation of PA and perfusion with IHC/IF has been reported.**
Gao et al. [149]	Foxn1nu; hind limb hiPSC-SMC injection (Hindlimb ischemia)	hiPSC-SMC promote VEGF-mediated angiogenesis, leading to improved hindlimb ischemia; **no correlation of PA with IHC/IF has been reported.**
Flurin Mueller-Diesing et al.[150]	BALB/cAnNRj mice; Orthotopic 4T1 injection (Mammary carcinoma)	Acetylsalicylic Acid reduced VEGFR-2 expression in a mouse cancer model, potentially resulting in more normal vessel growth and better tumor blood flow; **no correlation of Perfusion with IHC/IF has been reported**
Wang et al.[151]	NSG mice; subcutaneous injection of A549 cells (Lung cancer)	BACH1(oxygen- and redox-sensitive transcription factor) regulates tumor angiogenesis and vascularity**; no correlation of Perfusion with IHC/IF has been reported**

1.5 Biomarkers

A modern definition of biomarkers came from the National Institutes of Health in the 2000s, which defined them as "a characteristic that is objectively measured and evaluated as an indicator of normal biological processes, pathogenic processes, or pharmacologic responses to a therapeutic intervention"[152]. In biology, they are biological molecules, mostly proteins, which can be found in blood, urine, or tissues. It is important to notice that they can be also genetics-based, such as specific gene mutations or expression levels. Biomarkers can be used for a variety of applications such as screening, diagnosis, prognosis, treatment selection, and monitoring of disease. As those applications suggest, biomarkers play a crucial role in the practice of medicine, especially in the field of oncology. They can be fundamental for assessing the risk of cancer, but also for the study of Tumor-host interactions and Tumor burden, reflecting cellular functions like cell death or angiogenesis. Also, the identification in oncology of specific markers can predict the outcome of the medical treatment[153].

The main categories in oncology are prognostic and predictive biomarkers. CA19.9 is a glycoprotein antigen widely used in clinics, especially for monitoring PDAC[154]. It is an indicator of aberrant glycosylation, and high levels in blood and urine have been associated with more aggressive cancers and poor prognosis. This biomarker is not only restricted to pancreatic cancer but has also been detected in other gastrointestinal cancers like CRC[155]. A study has shown that CA19-9 is associated with a worst outcome if occurs in combination to an increase in Carcinoembryonic antigen (CEA). CEA is another widely used oncology biomarker, representing a glycoprotein involved in intracellular adhesion and cell-cell communication. In tumoral cells, it is mainly involved in angiogenesis and metastasis. Higher levels in blood are associated with poor prognosis. Despite the utility of these biomarkers, their sensitivity and specificity are limited. For CEA in colorectal cancers, a sensitivity of 77% and a sensibility of 84% is reported when a cut-off of 2.5ug/L is used for diagnostic purposes. Also, CA19-9 had poor sensitivity (75.5%) and specificity (77.6%) in PDAC, where 10-37% of patients

show normal levels of this marker. For that reason, in both CRC and PDAC they are not sufficient as single markers and are usually used in combination for increasing accuracy[156,157].

In account of that, recently several studies have focused on the identification of new biomarkers to improve diagnostic and prognostic accuracy in oncology. It has been demonstrated that ion channels, functioning as regulators for many cellular functions, are expressed abnormally in a variety of malignant malignancies. In this regard, ion channels can be viewed as Tumor markers, and they might also have clinical uses. Ion channels are transmembrane proteins that provide a pore controlling passive ion fluxes which are important for many essential physiological functions like control of cell volume[158]. They are possible targets and indicators for certain drugs and antibodies because of their surface location[159].

1.5.1 hERG1 potassium channel

Type 1 human ether-a-go-go-related gene potassium channels (hERG1, known also as KCNH2) are voltage-dependent channels fundamental for cardiac repolarization, as they generate outwards potassium currents crucial that lead to the repolarization of the cardiac action potential. The gene mapped on chromosome 11, in q35–36 position, encodes 1159 amino acids, where N and C-terminal are both located in the cytoplasm. Functionally, the channel consists of 4 alpha subunits that assemble to form a tetrameric channel, where each subunit has 6 transmembrane segments numbered S1-S6, where the pore helix and selectivity filter are located between S5 and S6[160]. Loss of function mutations in hERG1 can lead to the inherited long QT syndrome, which causes a disorder in ventricular repolarization that predisposes to the development of ventricular arrhythmia and sudden cardiac death[161,162]. In addition to their role in cardiac physiology, hERG1 channels are overexpressed in several different types of solid tumors such as colorectal cancer, breast cancer, pancreatic cancer, non-small cell lung cancer, and hematological malignancies including acute, myeloid leukemia, and chronic myelogenous leukemia, where it regulates the resting Vm due to its voltage-

dependent properties[163,164]. Especially, in PDAC the blocking of hERG1 has been found to reduce cellular migration and growth, and its overexpression has been linked with the worst prognosis. Also, in primary colon rectal cancer has been observed that higher levels of KCNH2 are linked with invasive phenotypes, but also is a negative prognostic factor in association with Glut-1 absence and reduced chemosensory for several chemotherapeutic agents (i.e. paclitaxel, camptothecin)[165].

1.5.2 Integrin β1

Integrins consist of heterodimeric cell surface receptors of two non-covalently linked alpha and beta subunit that mediate cell-matrix adhesion and cell-cell interaction. Up to now, 18 alpha and 8 beta subunits have been identified in humans, that can assemble in 24 different integrin heterodimers. β1 integrin represents the most widespread and abundant integrin subunit, with a central role in regulating migration, proliferation, survival, and differentiation of various cell types, which mainly came from the ability to interact with a large number of extracellular matrix ligands and the transduction of both inside-out and outside-in signals. Integrins are maintained in an inactive state characterized by a bent conformation, which can switch to an active expand conformation upon binding to dedicated modulator proteins, such as talins and kindlin. The activation of the integrin-mediated by an extracellular ligands binding will trigger multiple transduction pathways, mediate the actin cytoskeleton remodeling, and the activation of kinases such as FAK, SRC, and PI3K, which in turn regulate a wide range of cellular functions like cell growth and survival. After binding the ECM, integrin receptors cluster together to form focal adhesion, where they anchor the cell to the substrate by connecting ECM to the actin cytoskeleton[166]. Integrin β1 is overexpressed in many cancers like colorectal cancer and lung cancer, where the α1β1 contributes to cancer progression, but also in pancreatic cancer as well as lung cancer and breast cancer, mainly due to the dimer α2β1 which has key role in promoting metastasis but also to contribute to chemotherapeutic resistance[167].

1.5.3 *hERG1/β1 Complex*

Recent evidence highlights an interplay between hERG1 channels and integrinβ1. They can communicate not only by interaction through the formation of a physical macromolecular complex but also with diffusible signals such as intracellular second messengers that reciprocally modulate their functions. Their inter-regulation has been demonstrated in different cancer cells, where hERG1 activity regulates the expression and clustering of β1 integrin which in turn modulates the activity of the potassium channel.

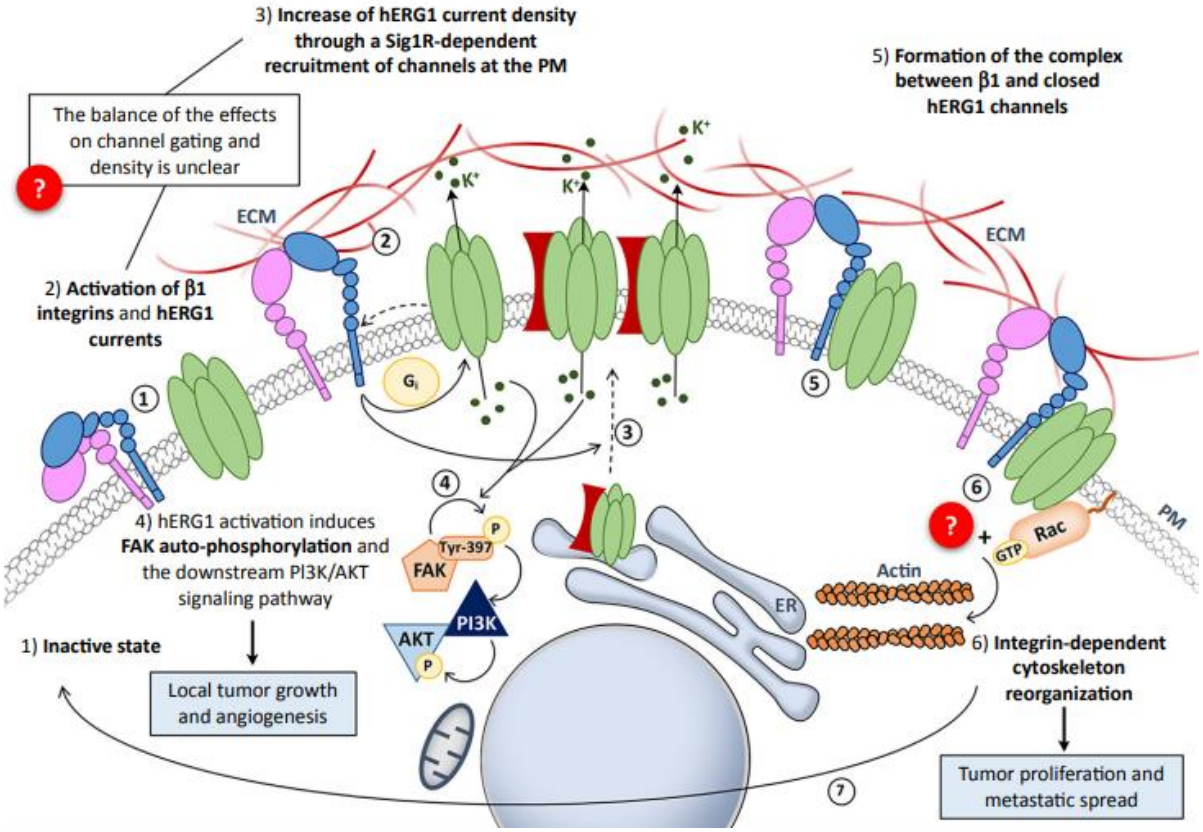

Figure 9 Schematic representation of physical and functional interaction between hERG1 and β1integrin in cancer cells ("Ion Channel Conformations Regulate Integrin-Dependent Signaling" Andrea Becchetti, Giulia Petroni, Annarosa Arcangeli)

K+ flux appears to be a key event that regulates FAK phosphorylation and the downstream PI3K signaling pathway, implicated in tumor growth and angiogenesis.

That event can be due to the activation of integrin-dependent signaling cascades, as seen in neuroblastoma tumors, where the adhesion to fibronectin activates the pathways which leads to the activation of Gαi protein, which activates hERG1 current. Once the complex has formed, hERG1/β1 integrin is favored by the channel residing in the closed state. Indeed, the closing of hERG1 channel stimulates cytoskeleton reorganization and cell migration, acting in a new conformational state that can mediate signal transfer. The complex is observed in several cancers including colorectal cancer, gastric carcinoma, pancreatic cancer, breast cancer, and neuroblastoma. The complex sustains cell motility via a hERG1-centered mechanism in pancreatic adenocarcinoma PDAC, involving reorganizing f-actin in stress fibers and modulating filopodia formation and dynamics through interactions with small GTPases and [Ca2+]i[168–170]. In CRC, the co-expression is a marker of poor prognosis and metastatic potential, as triggers the recruitment of the PI3K p85 subunit within the complex and AKT phosphorylation, thus regulating autophagy and angiogenesis via an upregulation of HIF-1α, resulting in VEGF-A production[171]. The chemokine receptor CXCR4 is a component of the hERG1/β1 integrin complex in leukemia cells, and it initiates pro-survival signaling pathways and resistance to chemotherapy-induced apoptosis[172]. One relevant thing is that hERG1/β1 integrin interaction was not detected in cardiac myocytes; that is connected to the presence of the hERG1 auxiliary subunit KCNE1 (potassium voltage-gated channel subfamily E regulatory subunit 1), which blocked the interaction of hERG1 with β1. Since KCNE1 is not expressed in cancer cells, that made the complex hERG1/β1 integrin a valuable biomarker for developing antineoplastic therapy[173,174], which can be used as innovative cancer treatment strategies in addition to diagnostic and prognostic applications[175]. Indeed, it can modulate various cancer-related and cancer-relevant signaling pathways, depending on the pathophysiological context. These modulations have a functional impact on cancer cell survival, motility, proliferation, and other aspects. Conformational coupling is the main mechanism of signal transduction when the interaction between the integrin and the channel involves the creation of multiprotein complexes. This

interaction primarily consists of activating FAK and ERK phosphorylation, which triggers cell proliferation processes.

2. Aims

Preclinical studies are crucial to clinical research, yet 90% of drug candidates fail in trials. Reducing failure rates requires stringent criteria in preclinical settings, including new therapeutic strategies, better models mimicking *in vivo* cancer characteristics, and reliable Tumor identification and monitoring methods.

This thesis seeks to address these challenges by:

i. **Evaluating therapeutic strategies**: Investigating the efficacy of the bifunctional diabody scDb-hERG1/β1 in combination with gemcitabine for PDAC and with bevacizumab for CRC, aiming to improve therapeutic outcomes.

ii. **Developing advanced tumor models:** Establishing novel PDAC mouse models that more closely mimic the *in vivo* microenvironment of pancreatic cancer, including key features such as stromal components, to enhance biological relevance.

iii. **Characterization using Advancing imaging methodologies:** Applying the Vevo F2 LAZR-X system, which integrates photoacoustic and ultrasound imaging, to enhance the characterization of the previously mentioned tumor model, monitoring therapeutic response and evaluating angiogenesis.

3.Materials and Methods

3.1 Cell culture

Four major cell lines of human origin were used in this work: PANC-1 and RLT-PSC for PDAC, and HCT116-WT plus HCT116-Beva/A for CRC. For PANC-1, cells are grown and maintained in DMEM medium supplemented with 10% fetal bovine serum (FBS), 2% L-glutamine, and 1% penicillin-streptomycin. PANC-1 pancreatic ductal carcinoma cells showed a regular, round shape with a doubling time of approximately 52 hours. RLT-PSCs were cultured in DMEM-F12 with 10% FBS, 2% L-glutamine, and 1% penicillin-streptomycin. Pancreatic stellate cells (RLT-PSC) observed by light microscopy show clusters of cells with a small nucleus and little cytoplasm. RLT cells have a shorter doubling time than PANC-1 cells (about 28 hours) and a "star" appearance with arms branching off from the perinuclear area, with individual cells contacting their neighbors. HCT116 cells were cultured in RPMI added with 10% FBS, adding Bevacizumab 250 µg/ml to the growth medium of HCT116-Beva/A. Both CRC cell lines exhibited an epithelial-like morphology, with a short doubling time (ranging from 25 to 35 hours). All these cell lines were maintained in a 37°C incubator at 5% CO_2.

3.2 ELISA

HCT116-WT and HCT116-Bev/A cell lines were evaluated for VEGF-A secretion under various conditions. Cells were trypsinized when they reached a confluency of 80% and seeded in a 24-well plate at a concentration of $2x10^5$ cells/well in a standard culture medium, plus the treatment when needed. After 24h, the medium was replaced by 0.5mL of Optimem (Gibco; Carlsbad CA, USA) and harvested for an additional 24h period. In the end, the medium was collected and used to perform VEGF-A measurements using the Human VEGF-A ELISA kit (Invitrogen, cat. no. BMS277-2), following the manufacturer's instructions. Both cell lines were evaluated by adding to

the standard medium i) 250µg/ml Bevacizumab, ii) 50 µg/mL scDb-hERG1/β1, and iii) 250µg/ml Bevacizumab + 50 µg/mL scDb-hERG1/β1.

3.3 Western Blot and Coimmunoprecipitation

3.3.1 Western Blot

The adherent cells of the HCT116-WT and HCT116-BevA/A strains have been evaluated for the presence of the following proteins: β1-integrin, hERG1, HIF1-α, and VEGF-A.

To evaluate β1-integrin and hERG1, the two cell lines were first scraped off a T75 flask (80% confluency) and then rinsed with ice-cold PBS. Pellets were obtained by centrifugation at 1200 rpm, washed twice in PBS, and immediately incubated for 20 minutes in 1% NP-40 lysis buffer (1% NP-40, 150 mM NaCl, 50 mM Tris-HCl, pH 8, 5 mM EDTA, 10 mM Na4P2O7) supplemented with a complete tablet of a mix of protease inhibitors. The samples were maintained on ice throughout the experimental procedure.

To evaluate HIF1-α and VEGF-A, both cell lines were harvested in T75 flasks under hypoxic conditions for 16 hours. Subsequently, NP-40 was added to each flask and the samples were placed at -20°C to halt the cell cycle. After this, the cells were scraped off. From this point onwards, all the passages were conducted identically for each protein analyzed.

The lysates were centrifuged for 10 minutes at 4°C at 13,000 g. After that, supernatants were gathered, and protein content was measured using the Bradford protein assay (Bio-Rad, Hercules, CA) following manufacture instructions. 50γ were mixed with Laemly Buffer 4X, reaching a final volume of 16µL, and loaded in a 7.5% precast-gel (7.5% Mini-PROTEAN® TGX™ Precast Protein Gels). Electrophoresis is then performed by setting 100V and using a Tris-Glycine running buffer. After, proteins are blotted onto polyvinylidene fluoride (PVDF Trans-blot Turbo Biorad), using the trans-blot turbo systems set at 1.3A, 25V for 7 minutes. After blotting, the membrane

is rinsed a couple of times with T-PBS before adding the blocking solution (BSA5% in T-PBS) for 1h. The primary antibody is then added and placed at 4°C overnight (O.N.) The following antibodies are used: HIF1-α (Novus Biological, 1:500), VEGF-A (Santa Cruz, 1:500), r-pAb anti-β1-integrin, RM-12 (Immunological Science, Rome, Italy) at final dilution 1:1000, r-pAb anti-hERG1, C54 (MCK Therapeutics Srl, Pistoia, Italy) at a final dilution 1:1000 for WB. The next day, the membranes are washed in T-PBS before adding the secondary antibody (1:10000 Anti-Rabbit IgG Peroxidase a6154 Sigma; 10000 Anti-Mouse IgG Peroxidase a4416 Sigma) for 1h. The membranes are then analyzed by using the ChemiDoc Imaging system, applying HRP substrate 30s before revealing (Clarity Western Blotting Substrates, Biorad).

3.3.2 Coimmunoprecipitation

Cells were seeded on FN-coated 100 mm Petri dishes for 90 minutes at 1.5×10^6 cells/ml in order to perform co-immunoprecipitation. The Bradford protein assay was used to quantify the proteins, and the same technique as for the western blot was used, using NP-40 as the lysis buffer. Pre-clearing was performed on 1.5 mg of isolated cells by rotating Protein A/G Plus-Agarose (Sigma-Aldrich, St. Louis, MO) beads for two hours at 4°C, as per the manufacturer's instructions. Following that, cell lysates were gently rotated overnight at 4°C to precipitate the TS2/16 antibody (5µg) for 1 mg of protein. Beads were washed three times with PBS and the bound protein component was eventually eluted by boiling the samples in Laemmli buffer for 5 minutes at 95°C. The collected samples were run on a 7,5% polyacrylamide gel for 1 hour at 100 V in Tris-glycine-SDS running buffer (Bio-Rad). Using the "HIGH MW" program (1.3 A, 25 V for 10 minutes), Turbo Blot (Bio-Rad) was used to semi-dry blot gels on PVDF membranes. Membranes were treated with 0.1% Tween 20 in PBS containing 5% BSA for two hours at room temperature. Blots were then incubated overnight at 4°C with polyclonal antibodies against hERG1 (polyclonal rabbit polyclonal antibody. hERG1 CT pan–polyclonal antibody; DT-552, Di.V.A.L. Toscana Srl, Sesto Fiorentino, Italy), β1 integrin (rabbit polyclonal antibody. RM12, Immunological Sciences, Roma, Italy) at

1:1000 final concentrations and against tubulin (mouse monoclonal antibody. Anti-tubulin, Santa Cruz Biotechnology, Dallas, TX, USA) at 1:500 final dilution. The membranes were then incubated for 45 minutes at room temperature with either horseradish-peroxidase anti-rabbit secondary antibodies (anti-rabbit IgG (whole molecule) peroxidase, developed in Goat, Sigma-Aldrich, St. Louis, MO) 1:10.000 or horseradish-peroxidase anti-mouse secondary antibodies (anti-mouse IgG (whole molecule) peroxidase, developed in Goat, Sigma-Aldrich, St. Louis, MO) 1:5000. Then, using the ImageQuant LAS 4000 image capture system and the ECLTM peroxidase substrate (GE Healthcare, Amersham, UK), the immunoreactivity was assessed by enhanced chemiluminescence response. The ReBlot WB recycling kit (Merck Millipore, Burlington, MA) was frequently used for membrane stripping in accordance with the manufacturer's instructions.

3.3.2.1 Densiometric analysis

After background subtraction, densitometric analysis was carried out on three separate scans using ImageJ software (ImageJ v.1.38, U.S. National Institutes of Health). At least three distinct, independent experiments produced the results. Vinculin was employed for VEGF-A, whereas hERG1, β1, and HIF1-α values were adjusted on the α-tubulin signal. The signal for the co-immunoprecipitated protein (hERG1) was divided by the signal of the protein utilized for immunoprecipitation (β1 integrin) and normalized to the signal of the equivalent protein in the whole lysate (β1 integrin input) to quantify the hERG1/β1 integrin complex.

3.4 RNA extraction and reverse transcription (RT)

RNA was extracted from CRC cancer cell line HCT116-WT and HCT116-BevA/A, harvested in T75 flasks. Initially, the cell culture media was aspirated, and the surface was washed with phosphate-buffered saline (PBS). The PBS was then aspirated and replaced with fresh PBS, after which the cells were removed with a cell scraper. The

cells were collected in a 15-mL Falcon tube, which was then centrifuged for 5 minutes at 1100 RPM. The PBS was removed, and 1 mL of TRIzol reagent was added to the sample (1 mL from 10^6 to 10^7, as per the protocol). The subsequent step entails the incorporation of 0.2 mL of chloroform for each 1 mL of TRizol™ reagent utilized for lysis. The contents must be mixed using a vortex, which is crucial for the optimal separation of the three phases. Subsequently, the sample is incubated for 2-3 minutes, after which it is subjected to centrifugation for 15 minutes at 12,000 x g at 4°C. The mixture undergoes a phase separation, yielding a phenol-chloroform layer, an interphase, and a colorless aqueous layer at the top, which contains the RNA. The latter is then separated and collected in a new Eppendorf tube. At this juncture, the isolation of the RNA is initiated. The initial step entails the addition of 0.5 ml of isopropanol to the aqueous phase, in proportion to the quantity of TRIzol reagent utilized for lysis. This is followed by an incubation period of 10 minutes at 4°C. Subsequently, the sample is subjected to centrifugation for a period of 10 minutes at a speed of 12,000 x g at a temperature of 4°C. The precipitate of total RNA forms a white gel-like pellet at the bottom of the tube, and the supernatant is removed with a micropipette. Once the RNA has been precipitated, the sample is washed by resuspending the pellet in 1 ml of 75% ethanol and 1 ml of TRIzol reagent, which was used for lysis. The sample is vortexed briefly and then centrifuged for 5 min at 7500 x g at 4°C. This step is repeated a second time in order to remove as much as possible of various contaminants (e.g., guanidinium isothiocyanate), which would lead to inaccurate measurements upon quantification. Subsequently, the supernatant is removed with a micropipette, and the pellet is permitted to air dry for a period of 5 to 10 minutes. The final step in sample solubilization involves resuspending in 20-50 µl of RNase-free water by pipetting up and down. The sample is then incubated in a heat block set to 55-60°C for 10-15 minutes. The entire procedure is conducted with both samples and TRIzol maintained in a container with ice and under a chemical fume hood. At this juncture, it is feasible to quantify the field. RNA purity and quantification was assessed with Nanodrop (Thermofisher) system before reverse transcription, by

evaluating the absorbance ratio A_{260}/A_{280} and A_{260}/A_{230}. Once quantified, 1µg of RNA was used for reverse transcription with SuperScript IV Reverse Transcriptase (Invitrogen) and random hexamers using a 2-step protocol. In the first instance, the mixture was prepared as follows:

COMPONENT	**VOLUME**
Random Hexamers (50µM)	1 µl
Mix dNTP (10mM)	1 µl
RNA (1µg)	Up to 11 µl
H_2O	to 13 µl

The mixture was heated to 65°C for 5 minutes, then incubated on ice for 1 minute. In the second step, to each mixture we proceed in adding the following component:

COMPONENT	**VOLUME**
5x buffer SSIV	4 µl
DTT (100 mM)	1 µl
RNaseOUT	1 µl
Super Script® IV (200 U/µl)	1 µl

The final mixture is then firstly incubated at 23°C for 10 minutes, followed by an incubation at 55°C for 10 minutes. In the end, to inactivate superscript IV, we proceed with an additional step by heating the mixture to 80°C for 10 minutes. The final mixture can so be used immediately for RQ-PCR or stored at -20°C.

3.5 Real-time quantitative PCR (RQ-PCR)

mRNA expression of angiogenesis-related genes such as VEGF-A, VEGF-C, HIF-1α, HIF-2α, VEGFR1, VEGFR2, and ANGPTL4 were evaluated by Real-time quantitative PCR

(RQ-PCR) using SYBR green-fluorescent dye (Power SYBR Green, Applied Biosystems). The primers used are the following:

PRIMER	Sequence (5'-3')
FH2_VEGFA	**GACTTATACCGGGATTTCTTG**
BH2_VEGFA	**CTGGCTCAGGAAGATTTTATG**
FH2_HIF1A	**GAAACTACTAGTGCCACATC**
BH2_HIF1A	**GGAACTGTAGTTCTTTGACTC**
FH2_VEGFC	**CTGGCTCAGGAAGATTTTATG**
BH2_VEGFC	**TGTTTTTACAGACACACTGG**
FH2_ANGPTL4	**GCTGCATGCGTTGCCTC**
BH2_ANGPTL4	**CCCTTGGTCCACGCCTCTA**
FH2_EPAS1	**CAGAATCACAGAACTGATTGG**
BH2_EPAS1	**TGACTCTTGGTCATGTTCTC**
FH2_FLT1	**ATGTGAAACCCCAGATTTAC**
BH2_FLT1	**TGATTGTAGGTTGAGGGATAC**
FH2_FLT4	**AGGTATTACAACTGGGTGTC**
BH2_FLT4	**TTCCTCAAATGTCTTCATCC**
FH2_GAPDH	**GGGGTGTTGAAGGTCTAAA**
BH2_GAPDH	**GATCTGGCACCACACCTTCT**

GADPH gene has been used as housekeeping, to normalize the expression levels of all the genes involved. To proceed with RQ-PCR, a mix is prepared, in such quantities as to obtain 24 μl per well, to which 1μl of the cDNA obtained by retro transcription will be added. The mixture is the following:

COMPONENT	**VOLUME**
SYBR Green Mix	12,5 μl
Primer forward (10μM)	0,65 μl
Primer reverse (10μM)	0,65 μl
H_2O	10,2 μl

The PCR commenced with an incubation period at 95°C for 10 minutes, followed by 40 cycles of amplification. Each cycle consisted of denaturation at 95°C for 15 seconds and an annealing-extension step at 60°C for 1 minute. The relative quantification of

gene expression levels was determined using the ΔΔCt method. Each reaction was performed in triplicate.

3.6 Labelling scDb-hERG1/β1 with Indocyanine green (ICG)

The amine-reactive dye ICG was dissolved in anhydrous DMSO. Solutions of scDb-hERG1/β1 were incubated with ICG at ICG:scDb molar ratios of 5, 10, and 20 (5×, 10×, and 20×) in conjugation buffer (0.002 M NaHCO3 + 0.048 M Na2CO3 + 0.15 M NaCl, pH 8.5) for 1 hour in the dark at 37°C with gentle mixing at 750 rpm. Total volume (250µL) and DMSO percentage were kept constants for all reactions. Purification was performed using PD-10 desalting columns (Cytiva, Marlborough, MA, USA). We then proceeded with washing step using double-distilled H_2O (washes with 2.5 ml repeated 4 times for 10 ml of ddH_2O). At the end of the labelling, bring 2.5 ml ICG-scDb-hERG1/β1 to volume with ddH_2O. Pour the 2.5 ml solution onto the column and allow it to elute. Two phases are separated, a lower one (where the dye is excess and not bound to anything) and an upper one (where ICG and the antibody are bound). Once eluted, the column is then placed in a 15 mL Falcon, adding 1.75-2 mL of ddH2O to the column and centrifuge at 1000 g for 5 minutes.

Before testing in an *in vivo* setting, the scDb-hERG1/β1-ICG has been characterized by using the Vevo Phantom (FUJIFILM VisualSonics, Inc., Toronto, ON, Canada), which allows obtaining such agents' absorption spectra. To perform the acquisition, the chamber is filled with distilled water, and the tubes are inserted into the chamber and immersed in the solution. The tubes are then filled, by using a syringe fitted with a 27-gauge needle, with the following agents: scDb-hERG1-β1-ICG (16mg/Kg), ICG green (1mg/Kg) and mAb-hERG1-ICG (16mg/kg). At the end, absorption spectra for each agent are obtained, and the system automatically identify those peaks which allows the distinction of the different contrast agents when observed during *in vivo* situations.

scDb-hERG1-β1-ICG was used in *in vivo* setting by administrating 100 μg intravenously 1h before the imaging acquisition. Real-time PAI monitoring of the scDb-hERG1/β1/ICG green PA signal was carried out using the linear array transducer operating at 57 MHz.

3.7 Cell preparation for *In vivo Models*

Both PDAC and CRC cell lines, harvested in T75 flasks, were detached with trypsin and counted by using LUNA II system (Luna II ™, Automated Cell Counter, TWIN HELIX SRL). All the cells were then resuspended on PBS, considering a final volume of 20μL for orthotopic mouse models, and 100μL for subcutaneous. In the latter, before the inoculation of cells, we add 50μL of Matrigel (Corning Matrigel Matrix) to ensure a reduced spread out of cells.

3.8 Mouse models

For the *in vivo* experiments, the same animal models have been used, which are 6 weeks old Foxn1$^{nu/nu}$ athymic nude mice. Those are currently preferable for tumor cell engraftment as they lack only the mature T cells, representing the least immunodeficient mice available, keeping the innate immunity intact and providing a high degree of tumor cell engraftment.

3.8.1 Ethics

Each experiment was carried out at the University of Florence's Animal House (Ce.S.A.L.) in the L.I.Ge.M.A. laboratory (Laboratory of genetic engineering for the production of mouse models). Mice were kept in ventilated cabinets within the sterile room, where they had unrestricted access to food and water and a 12-hour dark-light cycle. The Italian Ministry of Health approved the procedures under authorization number 843/2020-PR. For each experiment performed, the minimum number of

animals required to guarantee the statistical validity of the analyses was used, based on the G*Power software (for details on the number of animals used, see the paragraphs below).

3.8.2 PDAC Orthotopic xenograft mouse model

Orthotopic PDAC mice models were generated by the ultrasound (US)-guided injection using the Vevo F2 LAZR-X imaging system, in which $1x10^6$ PANC-1 per inoculum was injected.

To assess the therapeutic efficacy of the combination of scDb-hERG1/β1 with Gemcitabine, mice were randomly assigned to one of five treatment groups on day 14 following cell injection. The control group was administered saline (n = 16), while the scDb-hERG1/β1 group received 16 mg/kg of the compound (n = 8). The third group was treated with 5 mg/kg of Gemcitabine (n = 11). The fourth group received Gemcitabine (25 mg/kg; n = 7), while the fifth received scDb-hERG1/β1 16 mg/kg + Gemcitabine/5 mg/kg (n = 5). Treatments were initiated on day 14 and continued until day 36.

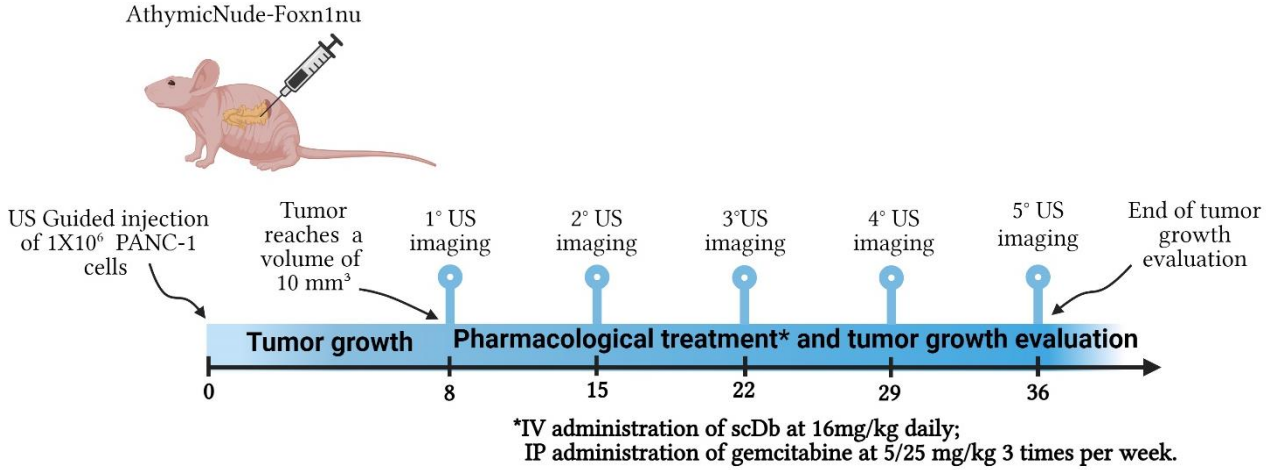

Figure 10 Schematic representation of the experimental timeline for the in vivo setting: from model generation to pharmacological treatments in PDAC model.

To assess the effect of treatments on survival, animals were monitored and euthanized when they showed signs of distress. Kaplan-Meier survival analysis was performed to

show the proportion of mice that survived for a given time after treatment.

For better mimic Tumor microenvironment, we then move on in increasing the complexity of PDAC mouse models. For that, we inject in an Eco-guided way $1x10^6$ PANC-1 and $1x10^6$ RLT-PSC alone and combination with each other at a ratio of 1:1 and 1:5 respectively, keeping $1x10^6$ of total cells per inoculum (for each group, *n* = 10). We then followed the Tumor growth for 52 days from the inoculum.

3.8.3 *CRC subcutaneous xenograft mouse model*

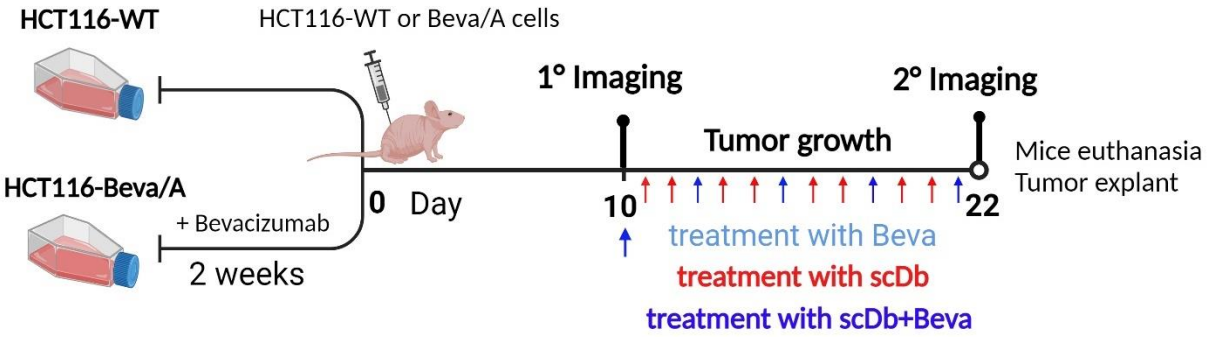

Figure 11 Schematic representation of the experimental timeline for the in vivo setting: from model generation to pharmacological treatments in CRC models.

For CRC, two subcutaneous mouse models of colorectal cancer xenograft were produced. A first model, sensitive to Bevacizumab, was generated by subcutaneous inoculation of $1x10^6$ HCT116-WT on both sides of the athymic Foxn1nu/nu mice flanks. A second model, resistant to Bevacizumab, was produced by subcutaneous inoculation of $1x10^6$ HCT116-Beva/A cells. Mice with CRC resistant or sensitive to bevacizumab were divided into four groups: a saline group (*n* = 22), a Bevacizumab group (treated i.v. with 10 mg/kg of Bevacizumab), scDb-hERG1/β1 group (treated i.v. with 16 mg/kg of scDb-hERG1/β1), and a group Bevacizumab + scDb-hERG1/β1 group (treated i.v. with 10 mg/kg of Bevacizumab and16 mg/kg of scDb-hERG1/β1) (all treatment groups, *n* = 12). All the treatments began on day 10 after cell inoculation and ended on day

22. Bevacizumab was administered in both models two times a week, and scDb-hERG1/β1 was administered daily.

3.9 Comprehensive Evaluation of Tumor Growth, Oxygenation, and Perfusion Dynamics

Tumor growth, oxygenation, and perfusion were evaluated using the Vevo F2 LAZR-X system (Fujifilm VisualSonics, Toronto, Canada), a hybrid system that integrates the capabilities of ultrasound with photoacoustic imaging. In the ultrasound department, high-frequency transducers (5 to 57 MHz) are employed to ultrasonically analyze various regions of interest (ROIs) in animals, in conjunction with optical fibers bundle, which have a resolution of 50 µm, to obtain photoacoustic images.
The procedure is carried out in four distinct phases on a previously inoculated mouse model.

1. **Preparation.** Initially, the optical fibers are connected to the ultrasound probe (57 or 29 MHz) via a specialized jacket. Subsequently, the animal is anesthetized with isoflurane gas (5% for induction, 2% for maintenance).
2. **Positioning.** The animal is placed on the imaging platform in the right lateral recumbent position for PDAC and immobilized, while in the prone position for CRC. Ultrasound gel is then applied to the acoustic window over the tumor site, and placing the ultrasound probe close to the animal's skin in the area of the tumor mass.
3. **Acquisition:** The ultrasound transducer is mounted on a three-dimensional motor, which enables the entire tumor mass to be selected and scanned. A preliminary ultrasound image of the tumor mass is obtained in the initial acquisition stage. Subsequently, photoacoustic imaging is conducted by selecting the appropriate wavelength window (750/850nm for deoxyHb and oxyHb, 820nm scDb-hERG1/β1-ICG) for acquiring it in 3D.

For the evaluation of Tumor perfusion in Colorectal cancer and PDAC mouse models, Nonlinear contrast mode on day 22 and 56 respectively is performed. 50 µl of Vevo MicroMarker contrast agents, which are non-targeted microbubbles, are intravenously injected. For perfusion acquisition, 2D cross-sectional imaging were performed using the 29 MHz linear array transducer (UHF29X).

4. **Assessment:** In the final step, Vevo Lab software is employed to render the tumor mass in 3D, thus enabling the assessment of its volume, oxygenation, and perfusion.

3.9.1 Data processing for Ultrasound (US) and Photoacoustic Imaging (PAI)

The volumes were measured delineating the ROI (Region of Interest) for every axial slide using Vevo LAB software.

PAI was used with OxyHemo-Mode was used to determine oxygen saturation (sO_2 %) and hemoglobin (Hb) comparing the PA signal at 750 and 850 nm. The transducer was equipped with a jacket for inserting the narrow optical fiber bundle.

Four parameters were obtained with PA: HV, $sO2_{TOT}$, sO_{2P}, and Hb_{TOT}. HV is the hypoxic volume and represents the necrotic part of the tumor. $sO2_{TOT}$ gives an indication of tissue oxygenation, while sO_{2P} considers only the peripheral part, excluding the necrotic central area. Hb_{TOT} represents the sum of all the hemoglobin values of the mass.

To evaluate the absorption spectra of the scDb-hERG1/β1-ICG, ICG alone, and mAb, Spectro-mode was used, and the absorption spectra of the contrast agents were directly saved into the Vevo Software. Then, the spectral fingerprints were used with the Multi-wavelength mode for acquiring the signal into the tumor masses. The Live Unmixing feature of the software enables real-time display of spectrally unmixed

components, allowing for dynamic monitoring of the conjugate's distribution and targeted delivery during multispectral imaging.

3.9.2 Data Processing for Contrast Enhanced Ultrasound (CE-US)

Tumor perfusion status was assessed at day 22 for CRC (end point) and 56 for PDAC by Contrast Enhanced Ultrasound (CE-US) imaging following i.v. injection (50 µl, tail vein) of non-targeted Vevo MicroMarker (contrast agent;Fujifilm Visualsonics). 2D cross-sectional imaging of tumors were obtained with 29 MHz linear array transducer (UHF29X). Data were processed with VevoCQ software (Visualsonics Fujifilm), and the ROI was drawn manually along the perimeter of each tumour using the measurement tools. The perfusion parameters calculated from each ROI were Peak Enhancement (PE), mean transit time (MTT), time to peak (TTP), Area Under the Curve (AUC), and Perfusion Index (PI). The PE was defined as the maximum signal intensity measured after the injection of the contrast agent. The MTT was defined as the average time required for the contrast agent to pass through the ROI. TTP was defined as the time interval from the beginning of enhancement to the PE. The AUC was defined as the area under curve to infinite time. PI was calculated as AUC/MTT.

3.10 Histology and Immunohistochemistry on xenografts

Formalin-fixed, paraffine embedded HCT116-WT and HCT116-Beva/A were analyzed for the expression of the following protein: CD31 (Anti-CD31 antibody [RM1006], ab281583, Abcam), HIF1-α (NB100-296, Novus Biologicals), VEGF-A (VEGF (A-20) sc-152, Santa Cruz). Firstly, we proceed by cutting, with the microtome, a 5µm thick Tumor section. Each section is then dewaxed and rehydrated before the inactivation steps for endogenous peroxidase, which consists of exposing for 20 minutes to a 1% H_2O_2 in PBS solution. Antigen retrieval is then performed by heating the samples in a microwave oven at 600W in a citrate buffer pH 6.0 for 15 minutes. After two washing

steps of 5 minutes each, a 1h blocking step using 10% BSA in PBS is performed. The antibodies were added overnight at 4°C after the blocking step, with a proper dilution in 10%BSA/PBS as follows: CD31 (1:500), HIF1-α (1:100), VEGF-A (1:50). Immunostaining was carried out with a commercially available kit (ImmPRESS® HRP Universal, MP-7800), according to manufacturer's instructions. All the samples were counterstain with Mayer's Hematoxylin. HIF1-α and VEGF-A expressions were evaluated with an estimate of the percentage of immunoreactive cells, focusing on the areas observed at 10x magnification that exhibited a higher density of stained cells. α-SMA expression instead is used for counting the number of vessels in each slice analyzed.

3.11 Histological evaluation of necrotic volume (%) and vessel estimation

In HCT116-WT and HCT116-BevA/A untreated group, we calculated the percentage of necrotic volume and the vessel count. For determining the necrotic volume, all the samples were counterstained with Hematoxylin and eosin. To calculate the percentage of the necrotic volume, we approximate the paraffin section as a disk, obtaining the volume of our masses with the formula: $V_{section}=\pi\times r^2\times h$, where h represents the thickness of the sections (5μm) and r the radius of the masses calculating by ImageJ software. Once we have the $V_{section}$, we proceed to calculate the radius of the necrotic area, always by adopting ImageJ, with the same formula: $V_{necrotic}=\pi\times r^2\times h$, where h is the same as $V_{section}$. To calculate the percentage of necrotic Volume, we then proceed with the following formula: $(V_{necrotic}/V_{section})$ *100%.

For vessel count, we focused on three different kinds of analysis, by evaluating (i) the number of vessels normalized for the area of the section (Number of vessels/slice), (ii) the number of Vessels on the slice ($Vessels_{Slice}$), and (iii) extrapolating the number of vessels in all the Tumor masses ($Vessels_{TOT}$).

(i) For obtaining the Number of Vessels/slice, we count the vessels for a given section of the tumor and normalized for the given area (mm^2) of the slice, calculated by ImageJ. (ii) $Vessels_{Slice}$ is obtained by directly counting the number of vessels on the slice. (iii) To calculate the number of vessels within a given tumor volume, we ran a series of calculations, focusing on a disk with specific dimensions for a better approximation of paraffine sections and particle characteristics, and assuming a sphere volume for global tumor masses. The volume of the disk representing the paraffine sections is calculated with the formula: $V_{section}=\pi\times r^2\times h$, where h represents the thickness of the sections (5um) and r is the radius of the masses calculated by ImageJ software. The volume of the tumor masses has been approximated as a sphere and is calculated by the formula: $V_{tumor}=4/3\times\pi\times r^3$. In the end, the total vessel count has been obtained by the following formula: Total vessels= $(V_{tumor}/V_{section})$ ×n° Vessels of section.

All measurements were performed independently by three different experimenters, each blinded to the work of the others to ensure objectivity and minimize bias. This approach was applied consistently across all evaluations, including the calculation of necrotic volume and vessel counts, to enhance the robustness and reliability of the obtained results.

3.12 Statistical analysis

GraphPad prism software (version 5.1, GraphPad Software, San Diego, CA, USA) was performed for statistical analysis. For a single treatment group comparison, unpaired Welch T-test was used to identify statistically significant differences ($p_{value}<0.05$). Using R software (v.4.2.2), the log-rank test was used to determine the significance of the mean survival in the Kaplan-Meier curves.

4. Results

4.1 Pancreatic Ductal Adenocarcinoma (PDAC) Studies

4.1.1 Generation of orthotopic xenograft mouse model of PDAC

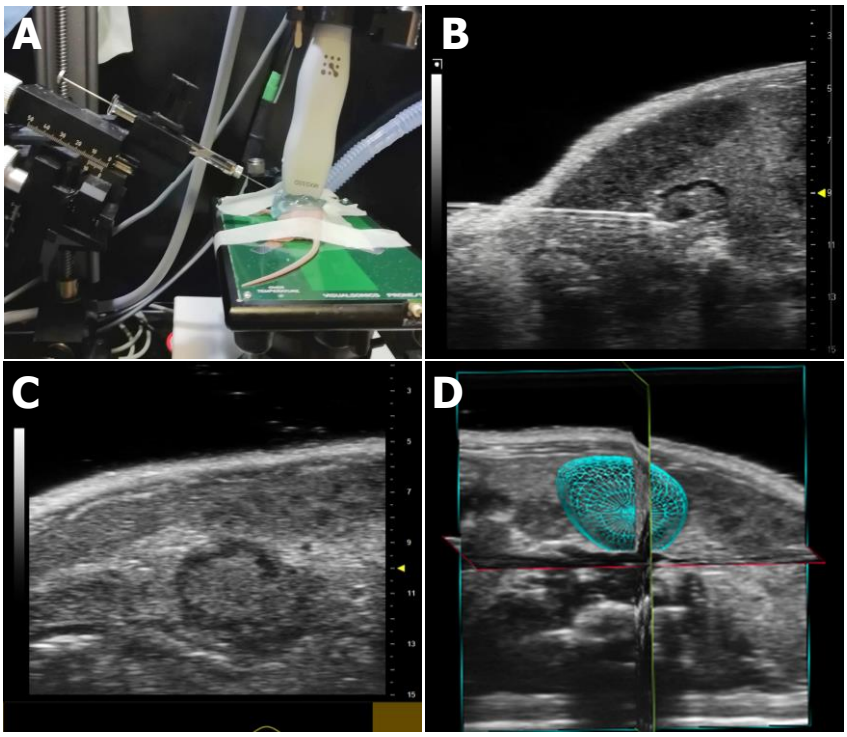

Figure 12 A) The mouse was placed on its right flank and the needle of the Hamilton syringe was positioned perpendicular to the transducer. B) Needle insertion and injection of 1X10^6 PANC-1 cells into the pancreas C) Tumor development was monitored with USI and D) 3D rendering of the Tumor mass, obtained by VevoLab software.

To generate orthotopic xenograft mouse model of PDAC, we proceed with an ultrasound-guided injection of PANC-1 directly into the pancreas of athymic nude mice. The whole procedure relies on several steps that need to be properly followed. At first, we prepared 1x10^6 PANC-1, suspended in 20µL of PBS, one hour before the inoculation. Vevo F2 LAZR-X system is turned on and set to B-Mode imaging using the 57Mhz transducer.

First, is performed a subcutaneous injection of the analgesic drug carprofen (NSAID) at a dose of 5mg/Kg. We proceed by anesthetizing the mouse into the gas chamber using 4% isoflurane. Once the mouse is anesthetized, it is transferred to a handling table, properly heated to 37°C, and equipped with a nose cone that allows the exit of a continuous flow of 2% isoflurane, to keep the mouse anesthetized throughout the procedure. The mouse must be put on the right flank on the handling table, and adequately fixed with adhesive gauze on the right hand, right foot, and tail onto the electrode pads which allows to register ECG and respiration rate during the intervention (*Fig.12A*). In addition, the skin must be properly stretched to ensure an optimal perforation of the syringe during the injection. Once the mouse has been properly placed, we sanitize the skin with 70% ethanol and apply ultrasound gel on the abdomen by using a 50 mL syringe. The transducer, which is connected to a 3D motor, is then lowered towards the skin, and placed transversally to the animal body. Once it has been visualized the pancreas, we can proceed to prepare the syringe for the inoculation. For that, we load cells suspended 20µL of PBS in a Hamilton syringe equipped with a 28g x 30mm needle. The syringe is then placed on a specific holder micromanipulator, with the needle bevel facing up and making a 45° angle with the ultrasound transducer by lowering the syringe to the mouse skin. By doing that, we are able now to visualize the syringe in the US image on the display. The micromanipulator is then used to pierce the skin and insert the syringe needle into the pancreas. Before injecting the cells, we must ensure that the pancreatic tail we observed with the US visualization, is situated behind the spleen and close to the left kidney (*Fig.12B*). After that, we proceed by the injection of the 20µL bolus straight into the pancreas, leaving the needle in place for five to ten seconds, then slowly retracting it. In the end, take out the US gel from the mouse's flank and put it in a fresh cage by itself, observing until it has regained sufficient consciousness. PDAC mouse models required from 8 to 14 days before ipo-echogenic Tumor structure in the tail of the pancreas can be observed (*Fig.12C*). Tumor cell engraftment and tumor development were evaluated with 3D US imaging. The 3D acquisition was performed

in B-mode using the 3D motor that allows the transducer to scan the abdomen in various sections along the axis perpendicular to the transducer. A series of 2D images were obtained which were then assembled by the analysis software VevoLab, reconstructing the 3D anatomical image of the Tumor (rendering 3D, *Fig.12D*). 20 mice were injected with PANC-1, and 16 out of 20 animals developed the Tumor within 14 days.

4.1.2 *Evaluating scDb-hERG1/β1 Penetration in Orthotopic PDAC Xenograft Tumors using Photoacoustic Imaging*

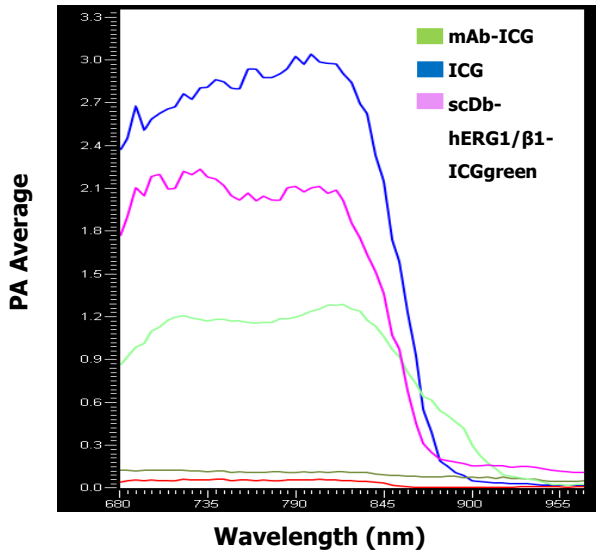

Figure 13 Comparison of the absorption spectra of scDb-hERG/β1-ICGgreen (purple), ICGgreen (Blue), and mAb-hERG1-ICGgreen (green). The spectra were obtained by using VevoPhantom.

Once we obtained the orthotopic PDAC xenograft mouse, we evaluated the capability of scDb-hERG1/β1, combined with gemcitabine, to inhibit tumor growth. Previous studies have demonstrated the presence of the hERG1/β1 integrin complex in PDAC primary samples and PDAC cell lines, as well as the high expression of hERG1 in primary human PDAC samples[178–180]. Before testing the efficacy of the combination therapy, we evaluate the capability of the scDb-hERG/β1 to reach and target the PDAC tumor masses in our mouse models, by conjugating it with ICG. Firstly, we use the Spectro mode to characterize the absorption spectra of the scDb-

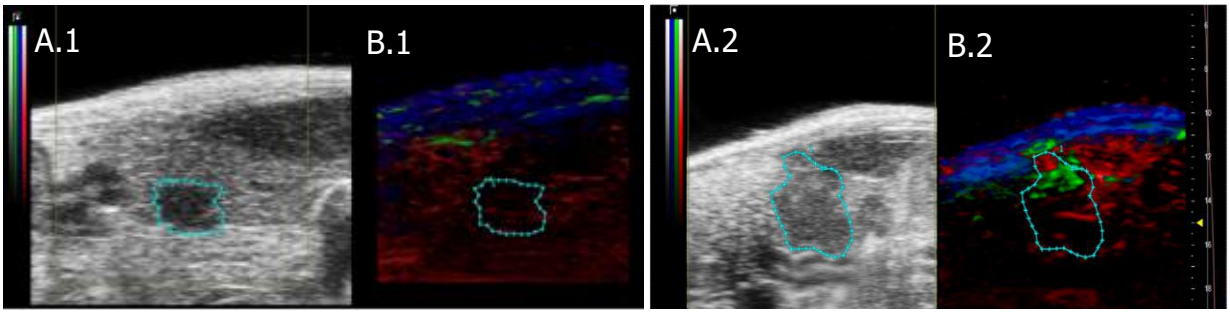

Figure 14 Two-dimensional ultrasound (A) and photoacoustic (B) images of tumor masses acquired one hour after intravenous injection of 1mg/kg ICGgreen (.1) and 16mg/kg of scDb-hERG1/β1 (.2). The tumor is evidence by cyan region. On PA imaging (B), red areas indicate the presence of oxyhemoglobin, blue areas indicate the presence of deoxyhemoglobin, and green spots indicate the ICG signal.

hERG1/β1 compared to ICG alone and in the conjugated form with a mAb. We observed that the scDb-hERG1/β1 absorption spectra retain the characteristic pattern of ICG, showing the successful conjugation of the antibody with the dye, but with slight changes in both peak intensity and peak shift, probably due to the interaction between the dye and the antibody. The peak at 800nm of the ICG, in scDb-hERG1/β1-ICG is shifted to 820nm compared to the free dye (*Fig.13*), allowing for the monitoring of the targeted delivery in the xenograft model. We then evaluated the Tumor penetration of scDb-hERG1/β1-ICG in the xenograft model. Two mice bearing PDAC xenograft tumors with a size of 20 mm^3 were intravenously administered 50 µL scDb-hERG1/β1-ICG (16mg/Kg) and 50 µL of ICG alone (1mg/Kg). One-hour post-injection, Photoacoustic imaging used with Multiwavelenght mode was performed, unmixing the signal derived from oxyhemoglobin, deoxyhemoglobin, scDb-hERG1/β1-ICG, and ICG alone. Observing the PA signal intensity of scDb-hERG1/β1-ICG compared to ICG alone, we could appreciate an accumulation of the targeted construct within the tumor (*Fig.14B.2*). In contrast, no signal is appreciated when injecting only ICG alone (*Fig.14A.2*). These data confirm the specific tumor targeting capability of the scDb-hERG1/β1 antibody in the PDAC xenograft model, supporting the rationale for the combination therapy with gemcitabine. These findings have been submitted in Lottini et al. 2023 [181].

4.1.3 *Combinatory treatment on orthotopic PDAC xenograft*

Having shown that scDb-hERG1/β1 targets PDAC in *in vivo* mouse models, we evaluate its ability to impact tumor growth by combining it with gemcitabine at both therapeutic and sub-therapeutic doses. On account of that, 14 days after cell inoculation, mice were randomized in 5 groups: Saline (CNTRL), gemcitabine 25 mg/kg (Therapeutical

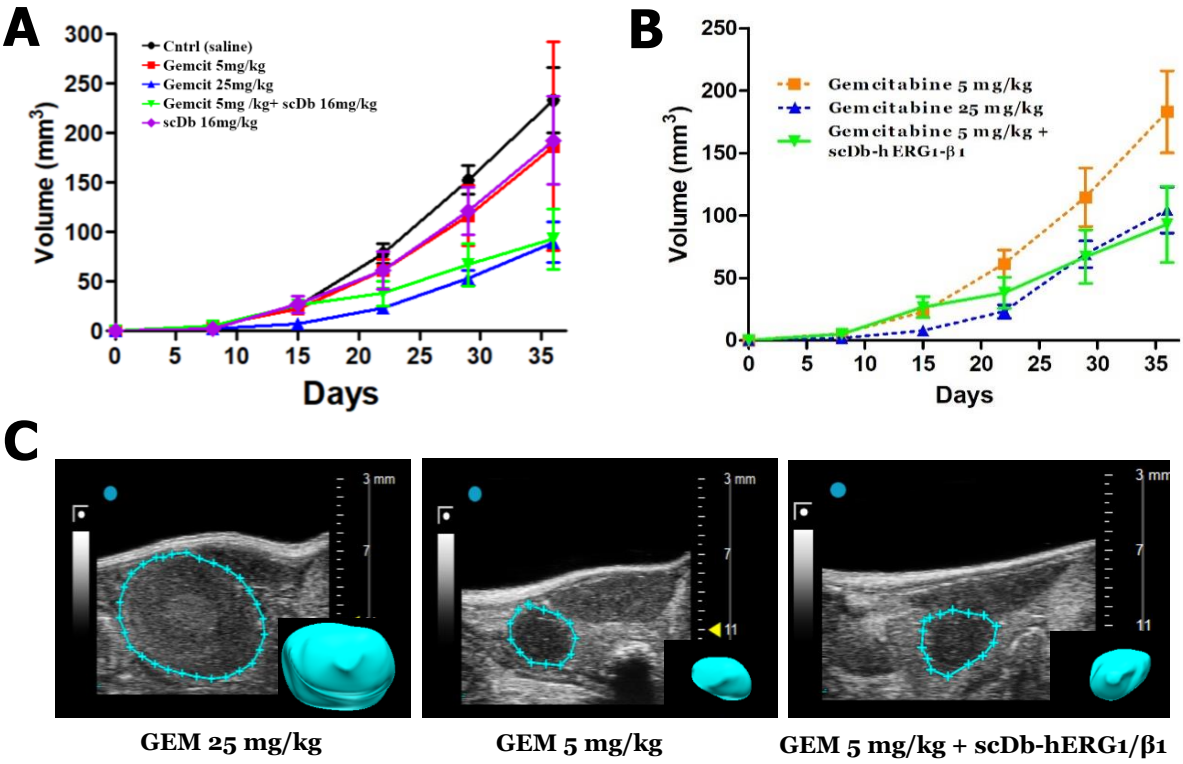

Figure 15 Tumor growth in time for all the treatment group (A). It can be appreciated how the combinatory treatment (B) enhanced the therapeutic efficacy of gemcitabine when applied at sub-therapeutical dose, reaching a same impact on tumor growth as the gemcitabine at therapeutic dose. (C) Representative US images of tumor masses at the endpoint, for gemcitabine 25mg/kg, 5mg/kg and combinatory treatment. For each 2D US image, is reported also the 3D rendering tumor masse for each treatment.

dose), gemcitabine 5 mg/kg (sub-therapeutical dose), scDb-hERG1/β1 16 mg/kg, and a combination of gemcitabine 5 mg/kg and scDb-hERG1/β1 16 mg/kg. The experimental endpoint was set on day 36 after cell inoculation, as tumor growth beyond this stage no longer reflects the typical progression of the disease. At the treatment endpoint, the saline group showed the greatest tumor growth compared to

all the other groups reaching a mean tumor volume of 246.2 mm³ ± 94.1 mm³, while gemcitabine 5 mg/kg and scDb-hERG1/β1 16 mg/kg alone showed a lower mean volume of 189.2 mm³ ± 74.1 mm³ and 178.4 ± 68.2 mm³ respectively, though this

A

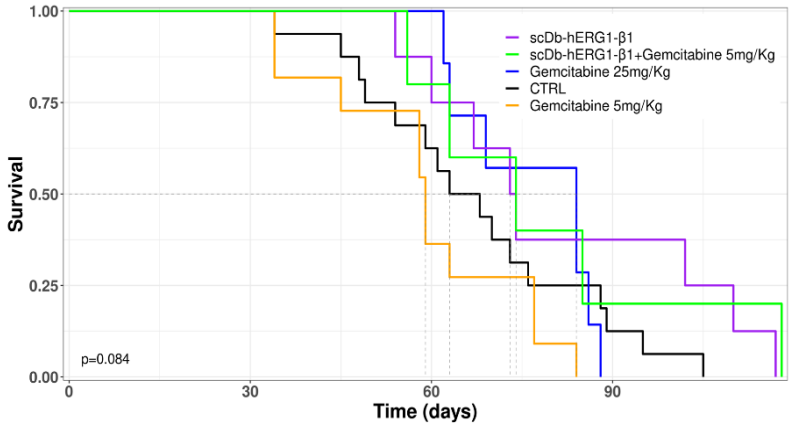

B

Groups	Mean survival time (Days)
Gemcitabine 5 mg/kg	59
Gemcitabine 25 mg/kg	76.6
scDb-hERG1/β1+Gemcitabine 5mg/kg	82
scDb-hERG1/β1	79
Cntrl (saline)	67

Figure 16. Kaplan-Meier survival curves for all groups under all the treatments (A). As evidence from the table (B), combinatory treatment provides a higher mean survival time compared to the other groups.

difference was not statistically significant *Fig.15A*). Of more interest was the effect on the growth of gemcitabine 25mg/kg alone and the combination of gemcitabine 5mg/kg with scDb-hERG1/β1 16mg/kg (*Fig.15B*).

As expected, gemcitabine 25mg/kg had a great impact in tumor growth, reaching a final mean tumor volume of 89.4 mm³ ± 32.0 mm³, reaching also the significant (p=0.0008) if compared to the saline group. Combinatory treatment shows a similar impact as gemcitabine 25mg/kg on tumor growth, showing a final mean tumor volume of 93 mm³. That is also statistically significant compared to the saline group (p=0.003), showing how the combination therapy significantly potentiated the chemotherapeutic effect of gemcitabine 5mg/kg alone, which displayed high tumor growth. That may be important, as a lower dose of gemcitabine can be fundamental to overcome side effects provided by the chemotherapeutic drugs while keeping the same therapeutic efficacy.

To assess the potential impact of the different treatment routes on survival and potentially establish long-term toxicity, mice were monitored after treatment and

euthanized when they display signs of suffering, performing a Kaplan-Meier survival analysis to assess differences between groups (*Fig.16*).

The mean survival time for mice treated with gemcitabine at 25 mg/kg was 76.6 days, compared to 67 days for the control group and 59 days for the group treated with gemcitabine at 5 mg/kg alone. The latter two groups showed a similar survival trend, reflecting the ineffectiveness of the subtherapeutic dose of gemcitabine. Increased overall survival was observed in the groups treated with scDb-hERG1/β1 alone (79 days) and in the combination group of scDb-hERG1/β1 and 5 mg/kg gemcitabine (82 days). The median survival time of the scDb-hERG1/β1 group was significantly different from that of the 5 mg/kg gemcitabine group ($p = 0.05$). The difference in media survival time between the 25 mg/kg and 5 mg/kg gemcitabine groups was statistically significant ($p = 0.02$). In addition, the combination group (scDb + gemcitabine 5 mg/kg) showed significantly longer survival compared to the 5 mg/kg gemcitabine group alone (82 days vs. 59 days, $p = 0.1$). In the 25 mg/kg gemcitabine group, severe signs of distress were observed, including reduced mobility and back arching, leading to euthanasia. These mice also exhibited a decrease in nesting behavior earlier than other groups, similar to the control group. At the time of sacrifice, 30% of the mice treated with gemcitabine 25 mg/kg developed ascites and exhibited abnormal liver conditions, confirming the toxic effects of the treatment. These findings explain why mice treated with the therapeutic dose (25 mg/kg) of gemcitabine started to die later but showed a narrower time window (days 62-88) of death compared to all other groups. In contrast, no ascites or abnormal liver or kidney conditions were observed during sacrifice in the scDb-hERG1/β1 or scDb-hERG1/β1 + 5 mg/kg gemcitabine groups. Additionally, general signs of suffering, such as abnormal posture and reduced mobility, were observed later in these groups compared to the control and 25 mg/kg gemcitabine groups, indicating a lower level of treatment-related toxicity. These findings have been submitted in Lottini et al. 2023 [181].

4.1.4 *New Orthotopic PDAC xenograft mice: RLT-PSC/PANC-1 co-injection*

The extracellular matrix, as a crucial element of the tumor microenvironment, significantly influences the development and progression of pancreatic ductal adenocarcinoma. PDAC is characterized by an abundance of desmoplastic stroma surrounding tumor cells, which increases the aggressiveness of malignancy and leads to increased therapeutic resistance[182,183].

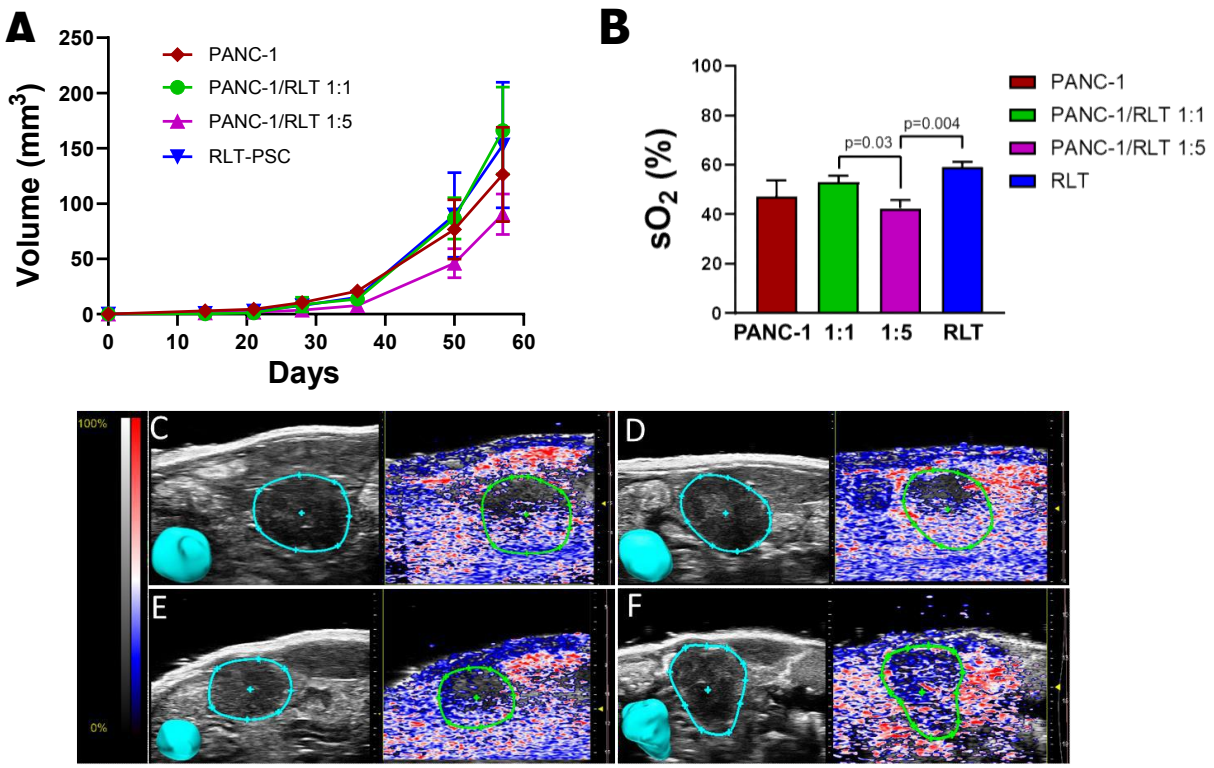

Figure 17 (A) Time course of Tumor growth for all the treatments. (B) Oxygen saturation levels, evaluated at days 56 for all the groups. Tumor volume and hypoxia: (C-F) Representative of B-mode and oxyhemoglobin PA images of pancreatic ductal adenocarcinoma (PDAC) tumors derived from the injection of PANC-1 cells (C), PANC-1/ RLT-PSC 1:1 (D), PANC-1/RLT/PSC 1:5 (E), and RLT-PSC (F) cells

Therefore, to better predict the therapeutic efficacy of novel therapies, new *in vivo* models that better mimic the tumor microenvironment are needed. To elucidate the role of stroma, we established 4 groups of orthotopic PDACs, always performing an

eco-guided injection of $1x10^6$ cells, as follows: (i) PANC-1 (n=5); (ii) RLT-PSC (n=5); (iii) 1:1 ratio between PANC-1 and RLT-PSC (n=7); (iv) 1:5 ratio between PANC-1 and RLT-PSC (n=6). These models were then characterized for Tumor growth, hypoxia, and perfusion. The mice were followed for 56 days after cell injection, performing US imaging starting on day 14 and repeating once a week, while PA and Non-linear contrast imaging were performed at the experimental endpoint.

Following tumor growth, all cell lines exhibit comparable time trends in tumor growth, although, at the endpoint, some differences in mean tumor volume can be observed between the different models. For PANC-1/RLT-PSC 1:1 and RLT-PSC, mean tumor volumes are similar, reaching 161.1 mm^3 and 156.4 mm^3, respectively. PANC-1 demonstrated a reduction in tumor growth over time in comparison to PANC-1/RLT-PSC 1:1 and RLT-PSC, reaching a final volume of 128.8 mm^3, although the observed differences were not statistically significant. A substantial decline in tumor growth was observed in the PANC-1/RLT-PSC 1:5 group, in comparison to the other groups, with a final volume of 87.5 mm^3 at the endpoint (*Fig.17A*).

It is also noteworthy that the PANC-1/RLT-PSC 1:5 group exhibits distinctive characteristics concerning hypoxia and the perfusion index. The oxygen saturation percentage in this group is lower than that observed in all other groups, reaching a final value of 41.7% (*Fig.17B*). The oxygenation levels of the PANC-1/RLT-PSC 1:5 model is significantly lower than those of the PANC-1/RLT-PSC 1:1 (52.6%; p=0.03) and RLT-PSC (59.2%; p=0.004) models. However, the difference is not statistically significant when compared to the PANC-1 model (45.3%; p=0.14).

The observation of the perfusion index, which relates to the functionality of the vascular network in the tumor, demonstrates a consistent reduction in the PANC1/RLT-PSC 1:5 model in comparison to the other models (*Fig.18*). However, this difference

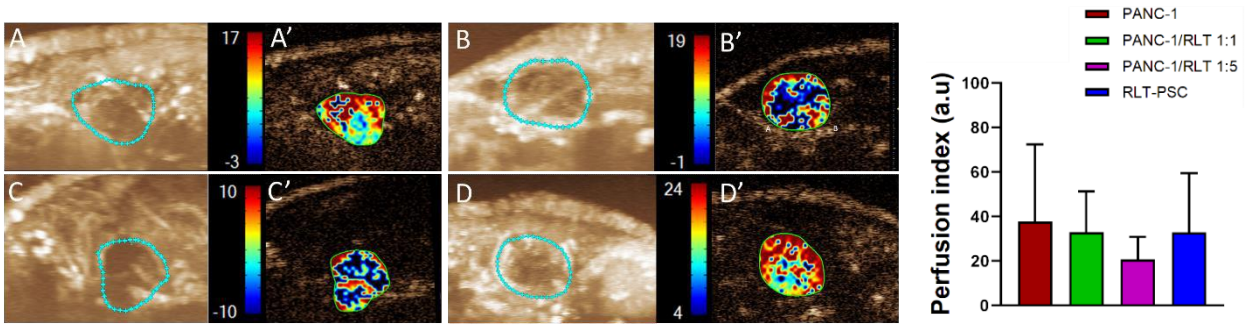

Figure 18 Tumor perfusion index: The maximum intensity projection (MIP) on representative tumors produced from the injection of PANC-1 (A), PANC-1/RLT-PSC 1:1 (B), PANC-1/RLT/PSC 1:5 (C), and RLT-PSC (D) cells was acquired using contrast-enhanced ultrasonography (CEUS) following the injection of microbubble contrast agents (Vevo MicroMarker). (A-D) The spatial distribution of microbubbles on sample tumors is depicted in parametric pictures. The region of interest (ROI) drawn around the periphery of each tumor has been used to compute the PI.

is not statistically significant.

The perfusion index in that model is lower (19.6 a.u) in comparison to all the other groups, with the PANC-1 model displaying the highest value (38.6 a.u). RLT-PSC and PANC-1/RLT-PSC 1:1 also in this case display similar values, of 34.5 and 35.2, respectively.

These results suggest that the introduction of a higher stromal component in the xenograft model, specifically a higher proportion of RLT-PSC, leads to increased hypoxia and reduced vascular perfusion, which in turn causes a reduction in overall tumor growth compared to the control PANC-1 model.

Additionally, we proceed to check the presence of metastasis in the liver (*Fig.19*). On macroscope inspection, tissue lesions were seen in the livers of two of the seven mice given the PANC-1/RLT-PSC 1:1 inoculation and two of the six mice given the PANC-1/RLT-PSC 1:5, indicating the possibility of metastases. Notably, animals given PANC-1 and PSC-RLT did not exhibit any lesions.

PANC-1/RLT-PSC (1:1)

PANC-1/RLT-PSC (1:5)

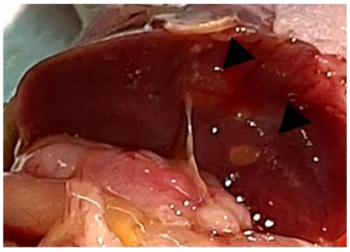

Groups	n° of mice with liver lesions/total
PANC-1	0/5
PANC-1/RLT-PSC (1:1)	**2**/7
PANC-1/RLT-PSC (1:5)	**2**/6
RLT-PSC	0/5

Figure 19 Macroscopic metastasis evaluation on the liver. The number of lesions observed in total for each group is reported in the table.

4.2 Colorectal Cancer (CRC) Studies

4.2.1 In Vitro Characterization of Angiogenesis-Related Gene Expression

Two CRC cell lines were used: HCT 116 (HCT 116-WT) and HCT 116 cells adapted to Beva (HCT 116-Beva/A) which were first established and characterized by Ellis' group[184]. These two cell lines were first characterized in an *in vitro* setting by evaluating angiogenesis-related genes and proteins. Firstly, we performed an RQ-PCR on both for the following genes: VEGF-A, VEGF-C, HIF-1α, HIF-2α, VEGFR1, VEGFR2, and ANGPT4.

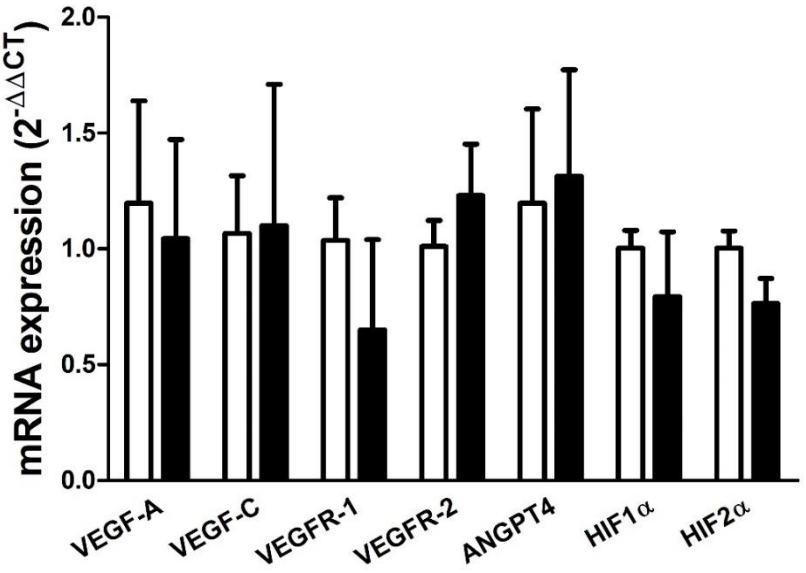

Figure 20 RQ-PCR of angiogenesis-related gene expression of HCT116-WT (white bar) and HCT116-Beva/A (black bar).

On both cell lines, we can see minimal differences in mRNA expression for all the genes, and no significant differences were found in any of the analyzed genes (*Fig.20*). Only in the case of VEGFR-1 emerged a difference, where HCT116-Beva/A has a decreased expression for the decoy receptor compared to HCT116-WT, although it is not significant. Minimal differences have also been observed when looking at HIF-

1α and VEGF-A, for both a minimal increase in HCT116-WT has been reported.

Interestingly, also by Western blot analysis for HIF-1α and VEGF-A proteins unveiled the same trend revealed with RQ-PCR (*Fig.21*). Under hypoxic conditions, minimal differences, as seen in the mRNA, have been highlighted, but no significant differences have been observed. This lack of variation at both the mRNA and protein levels reinforces the idea that the regulation of HIF-1α and VEGF-A remains stable in both cell lines.

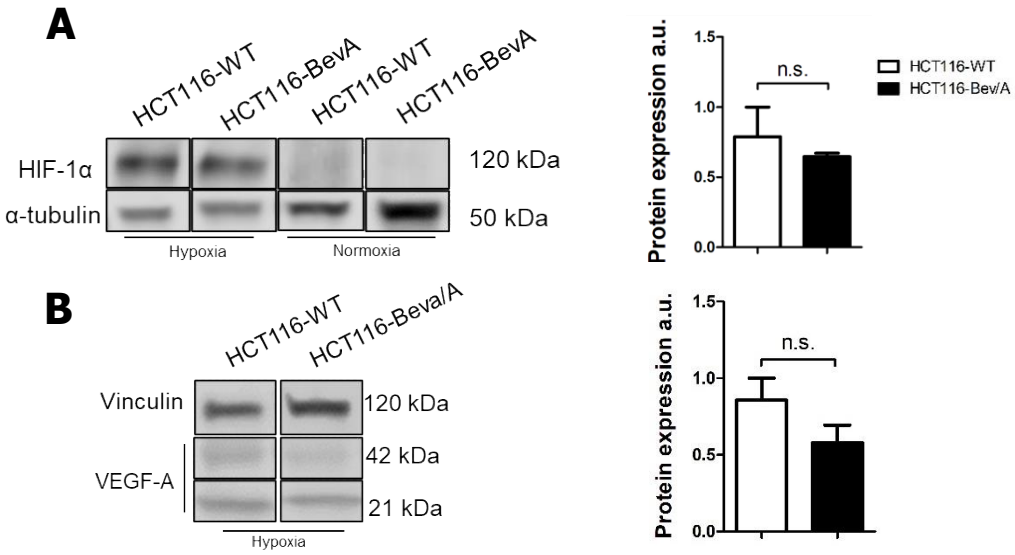

Figure 21 Western blot in hypoxia and Normoxia condition, and protein expression evaluation for HIF-1α (A) and VEGF-A (B).

Furthermore, both cell lines were analyzed for VEGF-A protein levels using ELISA, revealing similar trends across treatments (*Fig.22*). Although VEGF-A levels responded to treatments, no significant differences were observed between HCT116-WT and HCT116-Beva/A cells, indicating that VEGF-A expression is preserved in both lines. Both cell lines revealed a significant reduction in VEGF-A concentration after Beva treatment, equal to ~ 0.5 ng/ml. This reduction indicates that Bevacizumab neutralizes VEGF-A even in the Bevacizumab-adapted cell line.

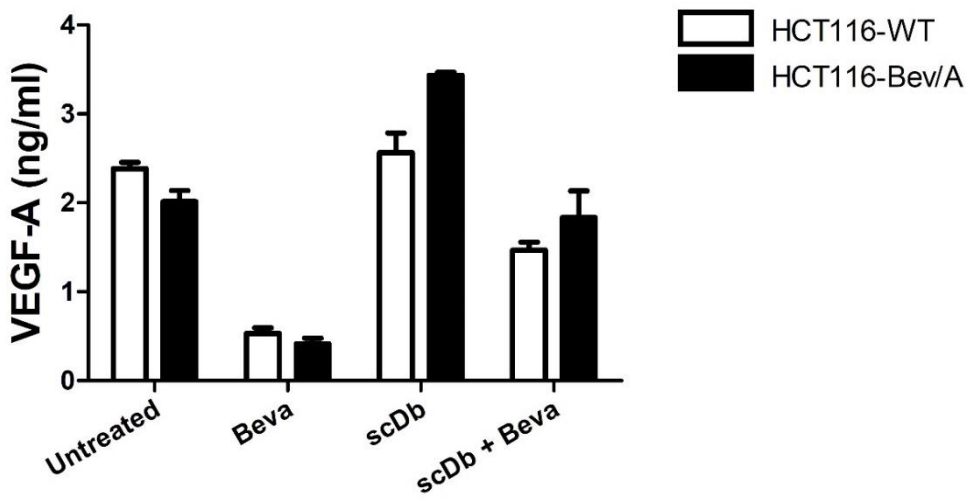

Figure 22 ELISA analysis of VEGF-A on either HCT116-WT and HCT116-Beva/A under different treatments.

There was a significant increase in VEGF-A levels with scDb-hERG1/β1 treatment compared to Bevacizumab-treated cells. Quite curiously, HCT116-Bev/A cells showed a huge increase in VEGF-A concentration (~4 ng/ml), almost double that of HCT116-WT (~2.5 ng/ml). The combined treatment of scDb-hERG/β1and Bevacizumab resulted in a reduction of VEGF-A levels in both cell lines compared to scDb-hERG/β1 alone, indicating a potential additive or synergistic effect of the combination therapy.
Overall, the adaptation of HCT116 cells to Bevacizumab does not significantly alter the expression or regulation of angiogenesis-related factors, highlighting the preserved nature of VEGF-A expression in both cell lines under various treatments.

4.2.2 *US and PAI on masses obtained from HCT 116-WT and HCT 116-Beva/A cells*

After *in vitro* characterization, the next step was to analyze the differences between these two cancer cell lines in an *in vivo* setting. For this purpose, cells were cultured in the absence (in case of HCT116-WT) or with 250 µg/ml (HCT 116 Beva/A) of Bevacizumab for 2 weeks. Subsequently, $1x10^6$ cells were injected subcutaneously into

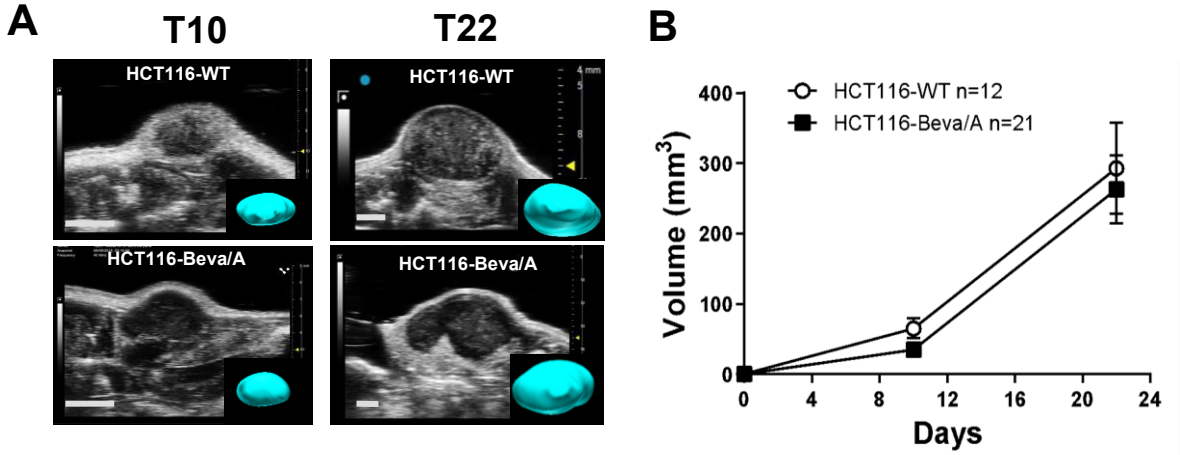

Figure 23 Tumor growth: (A) Representative US images of tumor masses at day 10 and 22 (endpoint) for HCT116-WT and HCT116-Beva/A cell line. (B) Following tumor growth in time, the two cell lines display identical time trend, reaching a same mean volume at the endpoint.

the flanks of Foxn1$^{nu/nu}$ athymic nude mice. Using ultrasound imaging, we monitor the tumor growth for those two different tumor models at 10 and 22 days. Looking at the growth curve, we cannot see any differences statistically significant both at 10 and 22 days (*Fig.23B*). At the endpoint both the HCT 116-WT and the HCT 116-Beva/A mass had similar mean volumes, measuring 293.5 mm3 ± 22.43 mm^3 SD and 263.1 mm3 ± 22.14 mm^3 respectively. On day 22, we then proceed to evaluate primary angiogenesis-related features of the masses, by using PAI and nonlinear contrast (CE-US) to assess oxygenation levels and perfusion characteristics, respectively.

Several parameters were evaluated using photoacoustic imaging. Specifically, taking advantage of the photoacoustic properties of hemoglobin, we first measured the hypoxic core volume (HV) and oxygen saturation using the distinct extinction

coefficient of oxy- and deoxyhemoglobin at 750 nm and 850 nm respectively. In addition to measuring the mean saturation of all tumors (sO_{2TOT}), we also determined the oxygen saturation of the peripheral region around the hypoxic core (sO_{2P}) (*Fig.24A,B*).

No difference as assessed between the two models looking at the HV mean values. The percentage of sO_{2TOT} was lower than sO_{2P} in both models, as predicted, and the absolute values of sO_{2TOT} and sO_{2P} diverged (*Fig.24C*). When comparing the two models, it is found that HCT116-Beva/A displays higher values for both sO_{2TOT} and

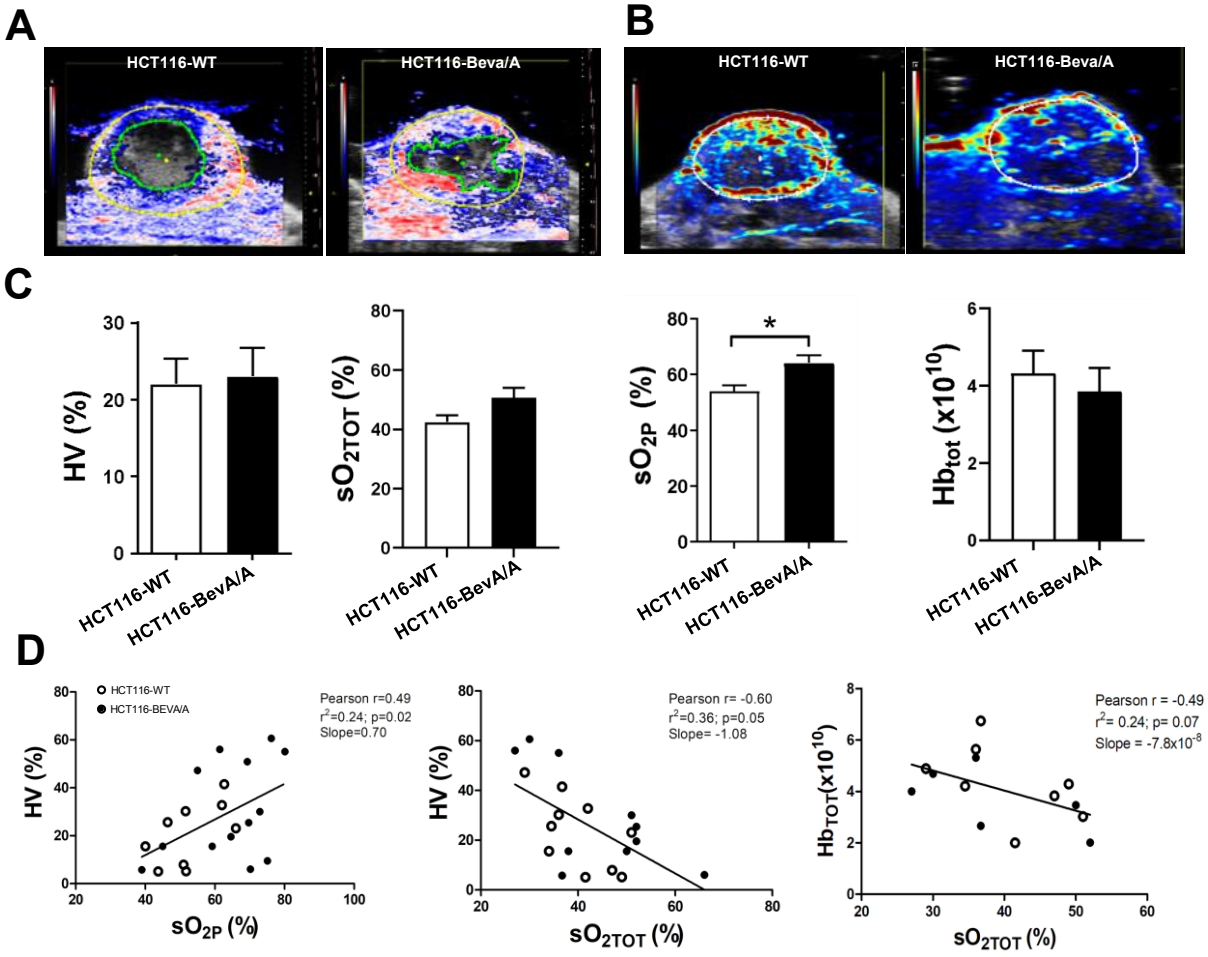

Figure 24 Representative images obtained by Photoacoustic imaging: (A) oxy-hemoglobin evaluation, with the hypoxic core defined as the area supported by the green line; (B) hemoglobin total content evaluation. HCT116-WT and HCT116-Beva/A were then compared for HV, sO_{2TOT}, sO_{2P}, Hb_{TOT} (C). Scatter plot with Pearson correlation analysis has been performed comparing HV, sO_{2TOT}, sO_{2P}, Hb_{TOT} (D).

$sO_{2P,}$ and the difference in sO_{2P} also approached statistical significance (p=0.01). Finally, we determined the total hemoglobin content (Hb_{TOT}) for all Tumor masses. In contrast to oxygenation levels, Hb_{TOT} displays similar values between HCT 116-WT and HCT116-Beva/A tumor models.

To gain more insight into HV, sO_2, and Hb_{TOT}, a correlational analysis was performed (*Fig.24D*). Pearson's correlation coefficients were calculated to evaluate the strength and direction of the relationships between those parameters.
HV compared to both sO_{2TOT} and sO_{2P} showed a moderate correlation, but with different trends. While sO_{2TOT} displays a negative moderate correlation (Pearson r= -0.6; p=0.05), by looking at sO_{2P} it emerges a positive moderate correlation (Pearson r= 0.5; p=0.02). Although, highlighting the differences between Hb_{TOT} and sO_{2TOT}, the correlation between these two parameters has shown a negative moderate correlation (Pearson r= -0.5; p=0.07). It can be seen from the data obtained that although the larger the necrotic volume is, the lower the total oxygenation within the mass is. In contrast, peripheral oxygenation increases as necrotic volume increases, implying that there are angiogenetic processes in the tumor periphery, and that necrotic volume may be a good way to assess the level of tumor progression.

4.2.3 *Perfusion on masses obtained from HCT 116-WT and HCT 116-Beva/A cells*

To obtain more angiogenesis-related parameters, we applied CE-US to quantify tissue perfusion by systemic injection of microbubbles. No statistically significant differences were found, despite the masses obtained from HCT116-Beva/A cells having generally lower values of PE (*Fig.25A*), TTP (*Fig.25B*), mTT (*Fig.25C*), and PI (*Fig.25E*) than those obtained from HCT 116-WT cells, suggesting a possible reduction in blood flow efficiency, increased leakiness (suggested by PE), and a reduced complexity of vessels (suggest by TTP and mTT). Only the AUC values are higher in HCT116-Beva/A masses compared to HCT116-WT. The lack of significance is due to the high variability within the single experiments.

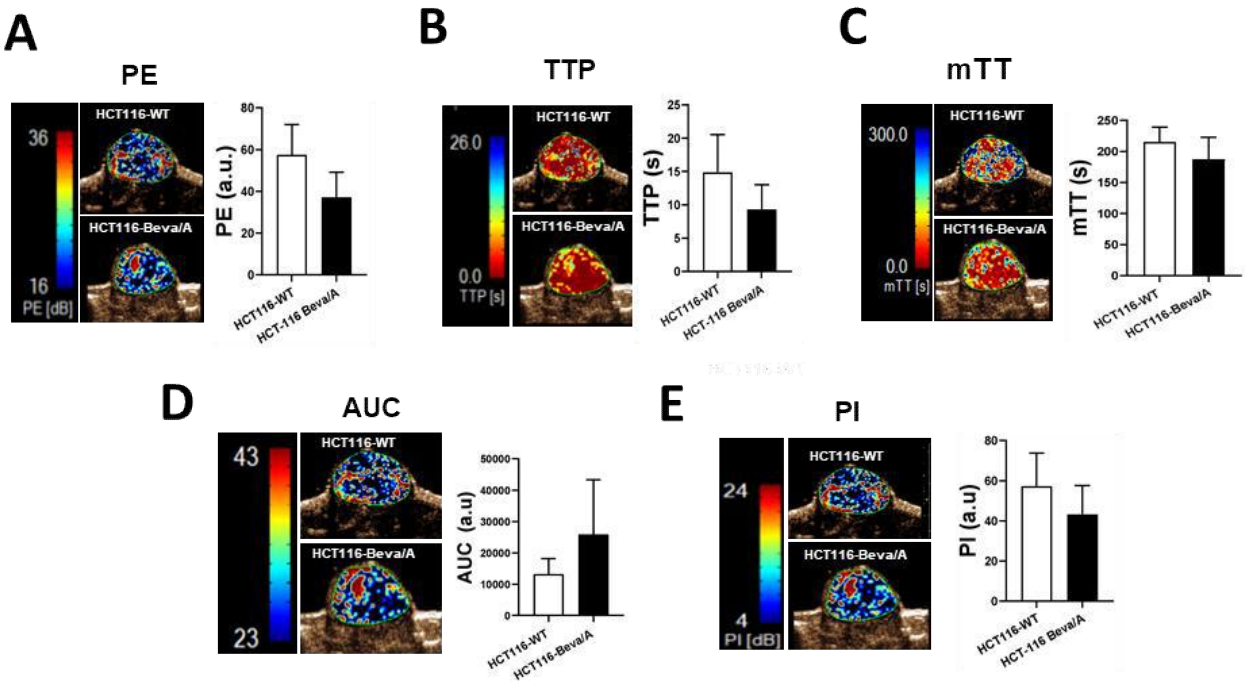

Figure 25 Nonlinear contrast imaging on HCT116-WT and HCT116-Beva/A cell lines. For each parameters obtained, a representative image and the comparison between the two tumors-derived cell lines have been reported. (1) Peak Enhancement (PE); (2) Time to Peak (TTP);(3) Mean Transit Time (mTT); (4) the Area under the curve; (5) Perfusion Index (PI).

4.2.4 *Correlation of Perfusion and Photoacoustic Imaging Parameters*

We pulled all data together to perform correlation analyses to determine how perfusion parameters correlate with PAI parameters (sO_{2TOT}, $sO_{2P,}$ or Hb_{TOT}). This analysis was based on 7 data points, all collected within a single experiment. This approach was chosen to minimize variability arising from instrumental fluctuations in oxygenation measurements and operator handling. The analysis revealed a moderate correlation of PE with Hb_{TOT} (Pearson r= 0.53; p=0.22) and to a lesser extent with sO_{2TOT} (Pearson r= 0.30; p=0.50) although no statistical differences were assessed (*Fig.26A*). TTP values showed only an inverse correlation with sO_{2TOT} (Pearson r= -0.67; p=0.10) and

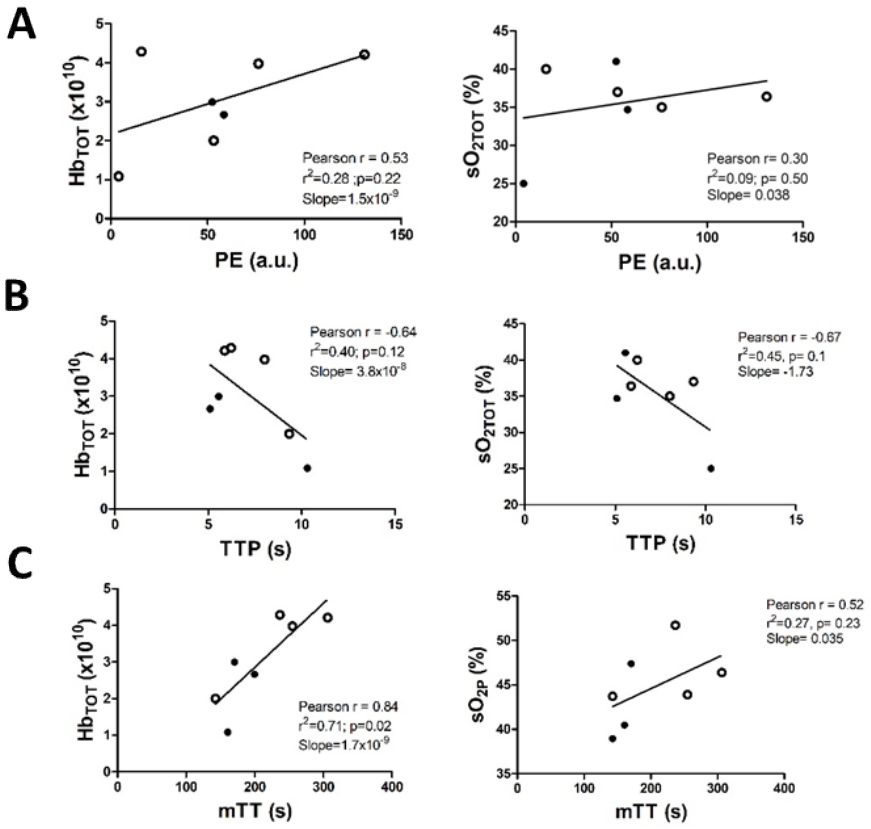

Figure 26 Scatterplot showing the relationship between photoacoustic and perfusion parameters. (A) Peak enhancement plotted against Hb_{TOT} and sO_{2TOT}; (B) TTP(s) plotted against Hb_{TOT} and sO_{2TOT}; (C) mTT(s) plotted against Hb_{TOT} and sO_{2P}.

Hb_{TOT} (Pearson r = 0.64; p=0.12) but not with sO_{2P} (*Fig.26B*). This indicates that a longer time to peak is associated with a lower total oxygen saturation and a lower total Hemoglobin, although these findings are not statistically significant. That showed that as vessels show more complexity, this leads to a reduction in global efficiency by reducing total hemoglobin content within the mass and reducing total oxygenation levels.

The mTT parameter was strongly correlated with Hb_{TOT} (Pearson r = 0.84; p=0.02) and to a lesser extent with sO_{2P} (Pearson r = 0.52; p=0.23), indicating that prolonged blood flow, due to abnormal vasculature, cause an accumulation of red blood within the tumor (*Fig.26C*). As sO_{2P} grows with mTT, it also suggests an increase in hypoxic volumes, as the previous paragraph evidences a correlation with that.

For all the other data, no correlation has emerged. Overall, the significant finding is the strong correlation between mTT and Hb_{TOT}, suggesting that the mean transit time is a good predictor of total Hemoglobin levels.

Therefore, we proceeded to consider the PAI and perfusion parameters to monitor the effects of pharmacological treatments known to affect Tumor angiogenesis (anti-angiogenic drugs AAD, to define whether they act as anti-angiogenic or vessel-normalizing drugs).

4.2.5 *Ex vivo assessment of hypoxia*

For validation of PAI, and to gain more insight into the differences between our two Tumor models of CRC, we proceed with histology and IHC analysis. Firstly, we proceed with the validation of HV by performing H&E staining on different sections of the two tumoral models. The necrotic area was measured for each section and its volume was calculated, yielding the necrotic volume for each Tumor. A difference in Necrotic Volume between the masses was not observed. The HV determined by PAI and the Necrotic Volume (Pearson r= 0.96; p<0.0001) showed a strong correlation (*Fig.27B*).

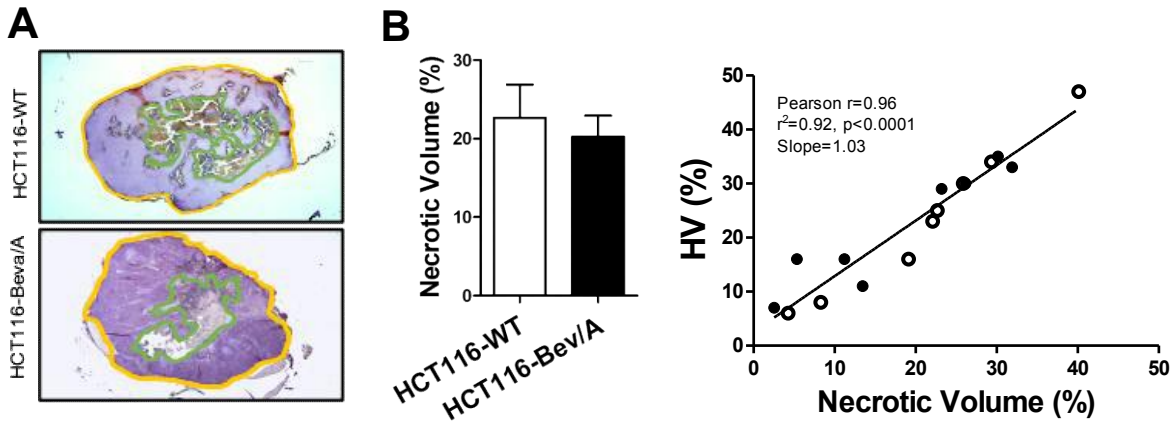

Figure 27 H&E staining on HCT116-WT and HCT116-Beva/A tumor (Magnification: 1.6x; Scale bar 1.7mm). The necrotic area is evidence in green (A). The comparison between necrotic volume between the two models shows no significant differences (B). PAI-derived parameters HV show a strong correlation with necrotic volume obtained as evidence by Pearson correlation coefficient = 0.96).

After that, we proceed with a direct evaluation of the vessels within the tumor masses. On account of that, we used CD31 antibody for vessel recognition, performing IHC staining (*Fig.28A*). The necrotic core of the masses was excluded from the vessel count. As detailed in Materials and Methods, three parameters were obtained: vessels/slice, $Vessels_{TOT}$, and mean vascular area. Although a higher value for each parameter can be observed for the tumor derived from HCT116-Beva/A compared to HCT116-WT, no significant differences have emerged.

This points out how the two models have no differences both in the number of positive CD31 $Vessels_{Slice}$ and $Vessels_{TOT}$ (*Fig.28B*).

Focusing also on PAI validation, we observed a positive correlation between $Vessels_{TOT}$ and Hb_{TOT} (Pearson r= 0.95; p=0.0001), and a positive correlation of $Vessels_{Slice}$ to sO_{2P} (Pearson r= 0.53; p=0.11), although not significant (*Fig.28C*). No correlation has been observed for sO_{2TOT}.

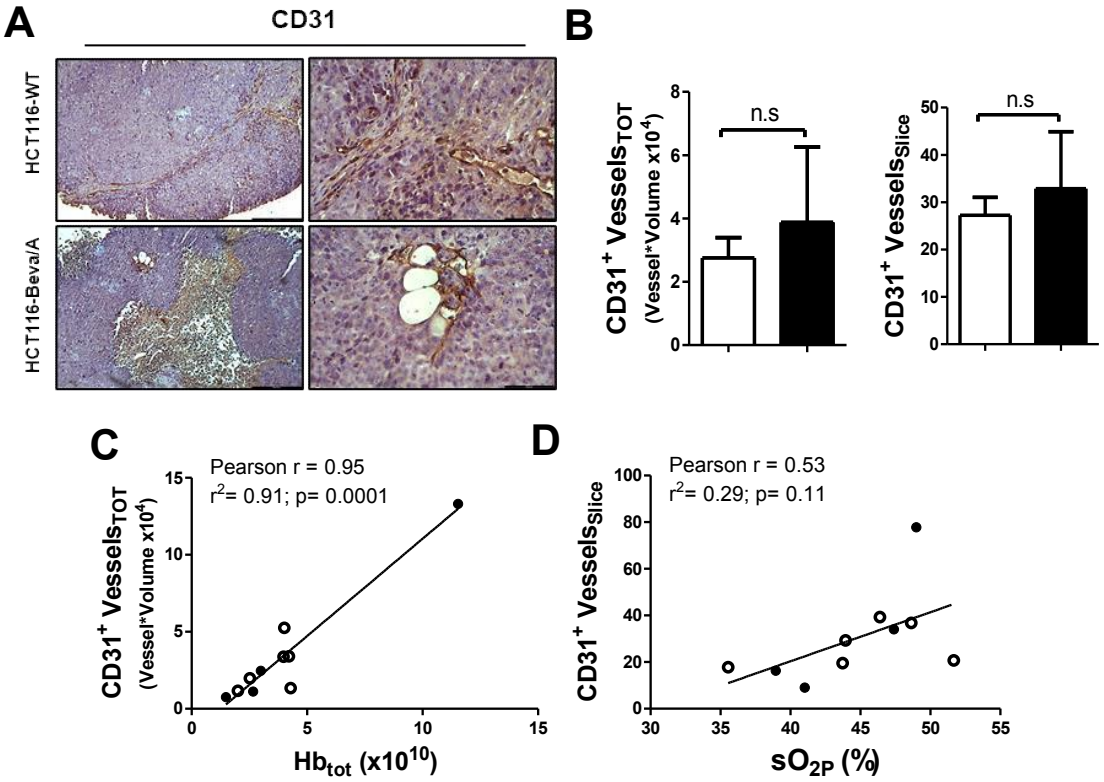

Figure 28. IHC of CD31 (1:500) on HCT116-WT and HCT116-Beva/A (A) (Magnification: 10x (left), 40x (right); Scale bar: 268 µm (10x), 67 µm (40x)). (B) Comparison $Vessels_{Slice}$, and $Vessels_{TOT}$ between the two different models. (C) Correlation between $Vessels_{TOT}$ and Hb_{tot} (D) and between $Vessels_{Slice}$ and sO_{2P} .

To further investigate angiogenesis-related factors, the expression of HIF-1α and VEGF-A in the two cell-type masses obtained by IHC was observed.

Whereas *in vitro* conditions don't evidence any differences both in mRNA and protein expression, in the tumor masses we observed a significant increase of both HIF-1α (*Fig.29A*) and VEGF-A (*Fig.29B*)on HCT116-WT masses compared to the HCT116-

Beva/A, reaching also statistical significance (HIF-1α: 31.2% (WT) vs 9.3% (Beva/A), p=0.004; VEGF-A: 40.6% (WT) vs 15.8% (Beva/A); p=0.006). A strong correlation emerged between HIF-1α and VEGF-A expression in either cell line (Pearson r = 0.94; p=0.05) (*Fig.29C*). However, the number of vessels/area (Pearson r= 0.59; p=0.22) had directly related HIF-1α expression (*Fig.29D*). Interestingly, an inverse correlation emerged between sO_{2P} and HIF-1α (Pearson r= -0.8; p=0.06) (*Fig.29E*).

The correlation between vessels/slice and mean vessel area with $sO_{2P,}$ can be considered to represent the total number of vessels and their dimension in the total volume of the mass. Considering that sO_{2P} is inversely related to HIF-1α, it can also be considered an inverse estimate of the hypoxic status of the tissue. Another way of putting it is that high sO_{2P} means that there is less hypoxia in the peripheral part of the tissue and, therefore, does not fire up the response of VEGF-A to hypoxia. The fact that the masses from HCT116-Beva/A cells show lower expression of VEGF-A and HIF-1α, along with higher sO_{2P}, having approximately the same number of vessels,

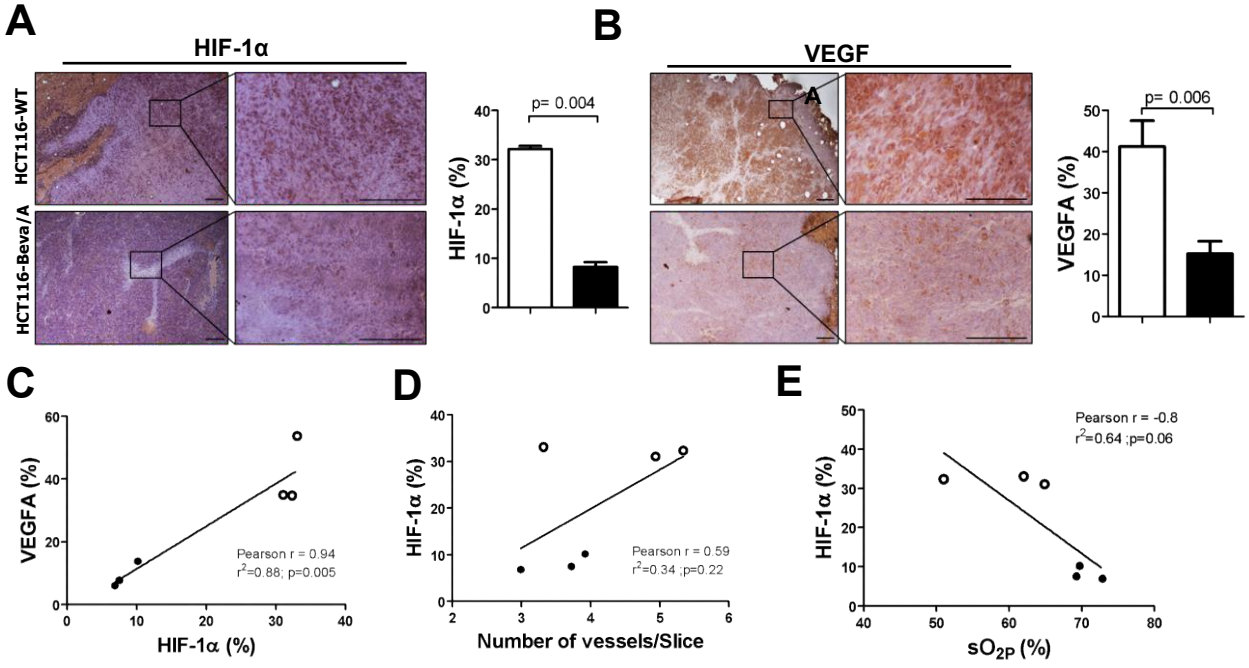

Figure 29 IHC and relative percentage expression of HIF-1α (A) and VEGF-A (B) (Magnification: 10x (left), 40x (right); Scale bar: 268 μm (10x), 67 μm (40x)). The parameters display high correlation between them (C), while HIF-1α display also a good correlation with the number of vessels/slice (D) and an inverse correlation with sO_{2P} (E).

supports this. Also, these data fit with perfusion parameters: an increase of VEGF-A and HIF-1α can lead to an increase in complexity and disorganization of the vascular network, and this is also evidenced with Perfusion parameters, where HCT116-WT shows a higher value for PE, TTP, mTT and PI, all supporting the increasing complexity (and leakiness) compared to HCT116-Beva/A.

4.2.6 *Effects of Bevacizumab (US, PAI and CE-US)*

Once we established the differences between the two models, we then proceeded to compare the influence of Bevacizumab's treatment on *in vivo* xenograft mice. Cultures were established *in vitro* for two weeks either in the absence (HCT 116-WT) or in the presence of 250 µg/ml Beva (HCT 116-Beva/A). After two weeks, $1x10^6$ cells were then injected subcutaneously into the flank of athymic nu/nu immunocompromised mice. 10 days after cell inoculation, mice were randomized into two different groups. One group of animals was treated with vehicle and the second one received i.v. 10 mg/kg of Bevacizumab twice a week, for a total of 2 weeks.
On day 22, the response of the Beva treatment was measured by tumor volume quantification using US imaging, and also by measuring HV, sO_{2TOT}, $sO_{2P,}$ and Hb_{TOT} using PAI. Perfusion parameters like PE, TTP, mTT, PI and AUC were quantitatively evaluated using CE-US.

The treatment with Bevacizumab resulted in a significant reduction of tumor volume for both cell lines but had stronger effects for HCT 116-WT (mean tumor volume = 72.3mm^3 ± 16.24 mm^3) than for HCT 116-Beva/A (mean tumor volume = 130.7mm^3 ± 15.36 mm^3) (*Fig.30A,B*). Beva treatment provided a reduction of HV for both cell lines compared to their corresponding untreated group, but these were not statistically different (*Fig.30D*). Overall, there was a significant reduction in sO_{2TOT} ($sO_{2TOT\text{-}Untreated}$= 42.4%, $sO_{2TOT\text{-}Bevacizumab}$=30.4%; p=0.002) (*Fig.30E*) and sO_{2P} ($sO_{2P\text{-}Untreated}$= 56.9%, $sO_{2P\text{-}Bevacizumab}$=37.9%; p<0.001) (*Fig.30F*) in the HCT 116-WT tumors, while in HCT116-Beva/A can be observed similar trend in sO_{2P} ($sO_{2P\text{-}Untreated}$= 67.9%, $sO_{2P\text{-}}$

$_{Bevacizumab}$=58.2%; p=0.01) (*Fig.30F*) but no differences can be seen for sO_{2TOT} ($sO_{2TOT\text{-}Untreated}$= 50.7%, $sO_{2TOT\text{-}Bevacizumab}$=49.1%; p>0.05) (*Fig.30E*).

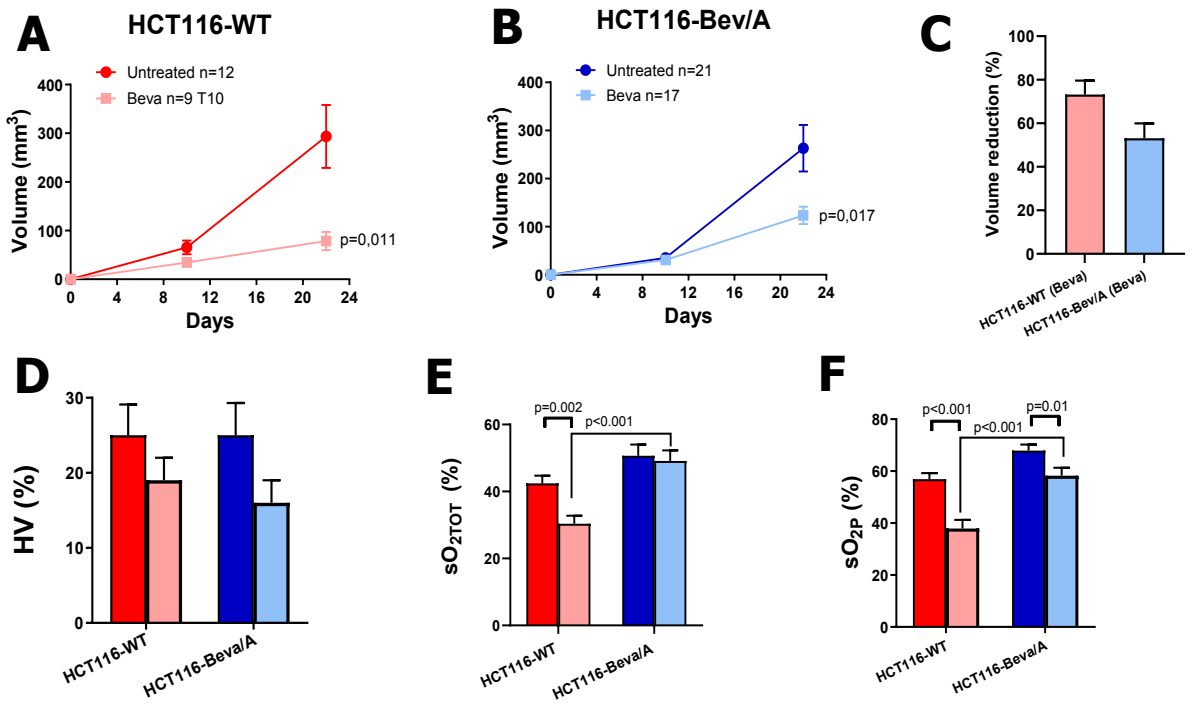

Figure 30 Tumor growth in time for HCT116-WT (A) and HCT116-Bev/A (B) treated with Bevacizumab. (C) Comparison of volume reduction between HCT116-WT (light red) and HCT116-Beva/A (light blue). Untreated and Bevacizumab-treated cell lines are compared for HV (D)m sO_{2TOT} (E) and sO_{2P} (F). Dark red and Dark blue represents HCT116-WT and HCT116-Beva/A respectively.

Regarding the perfusion parameters, a slight increase in PE,TTP and PI (*Fig.31A,B,E*) was observed in the Beva-treated groups, while a decrease was registered in mTT (*Fig.31C*). All these changes in perfusion parameters were more obvious between HCT 116-Beva/A and HCT 116-WT tumors, although not of statistical significance.

Tumor volume and necrotic area reduction accompanied Beva treatment, associated with a decline in sO_{2P}, reflecting a more hypoxic state. Such changes were lower in HCT 116-Beva/A cells, reflecting a condition of resistance to Beva. Although the results differ for oxygenation, the perfusion data show a similar trend in response to treatment

for both lines, underlying an improvement in overall perfusion as suggested by PE, PI, and mTT; yet, higher TTP suggests that blood flow may be absorbed more slowly at first, and things like the presence of bigger or more curved blood arteries, which fill more slowly yet eventually give good perfusion.

Overall, the response to the treatment evidence that both lines undergo similar changes, despite their differences.

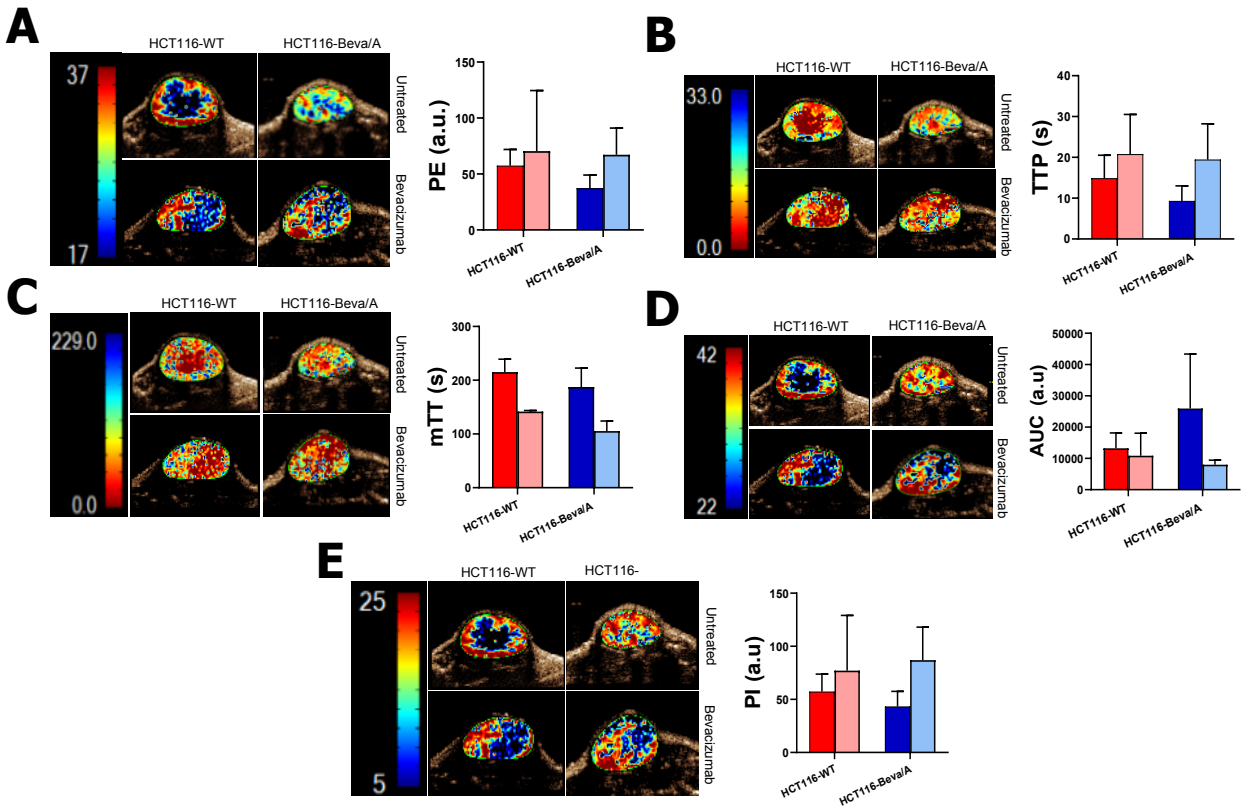

Figure 31 Nonlinear contrast imaging on HCT116-WT and HCT116-Beva/A cell lines treated with Bevacizumab. For each parameters obtained, a representative image and the comparison between the two tumors-derived cell lines have been reported. (A) Peak Enhancement (PE); (B) Time to Peak (TTP);(C) Mean Transit Time (mTT); (D) the Area under the curve; (E) Perfusion Index (PI). Dark red and dark blue represent HCT116-WT and HCT116-Beva/A untreated, while the lighter colors represent their treated counterpart.

4.2.7 *Evaluating scDb-hERG1/β1 Penetration in subcutaneous CRC Tumors*

Before testing the anti-angiogenetic effects of scDb-hERG/β1, we proceeded in the evaluation of its capability to reach the tumor site. Previous *in vitro* studies have demonstrated the presence of the hERG1-β1 integrin complex in CRC primary samples

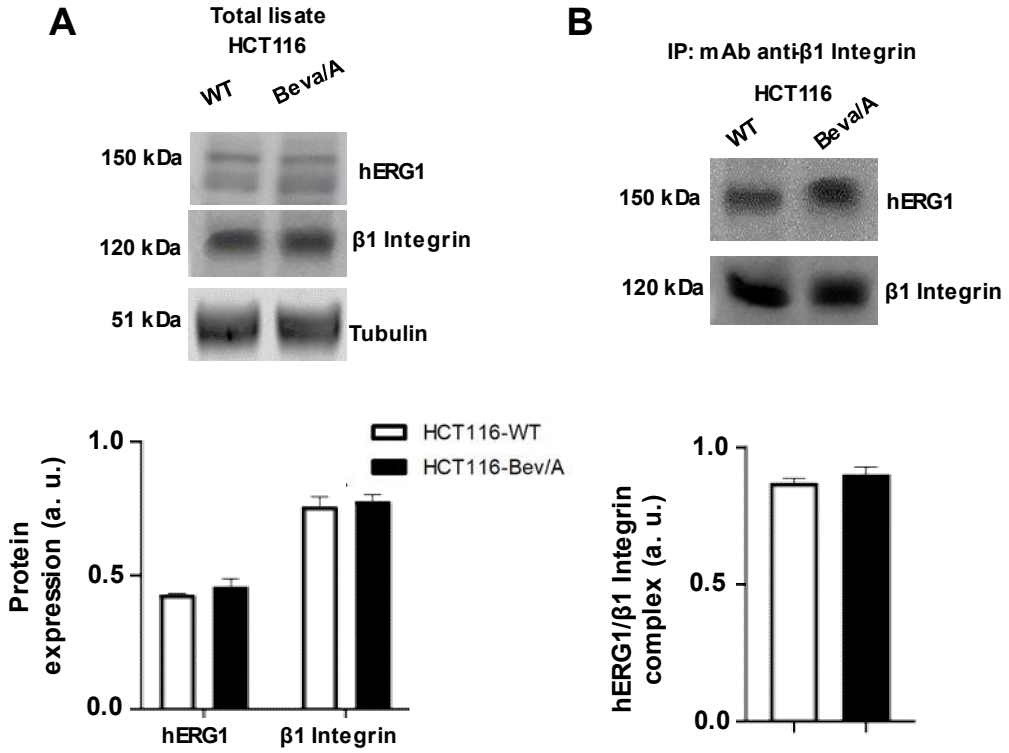

Figure 32 (A) hERG1 and β1 protein expression on HCT116-WT and HCT116-Beva/A. A representative Blots (upper panel) and densiometric analysis (lower panel) is reported. (B) Representative blots and associated densitometric analysis of the co-immunoprecipitation involving hERG1 and β1 integrin.

and CRC cell lines. In western blot analysis, both cell lines show similar protein expression of hERG1 and β1 (*Fig.32A*), and they co-immunoprecipitated equally (*Fig.32B*), confirming that the complex is expressed in both.

Then, we proceed as seen for PDAC, by firstly characterizing the absorption spectra of the scDb-hERG1/β1 compared to ICG alone and in the conjugated form with a mAb.

We then evaluated the tumor penetration of scDb-hERG1/β1-ICG in the subcutaneous model. Two mice bearing CRC subcutaneous tumors, either HCT116-WT and HCT116-Beva/A, with a size of 20 mm^3 received 50 µL scDb-hERG1/β1-ICG (16mg/Kg) and 50 µL of ICG alone (1mg/Kg) intravenously. We followed the signal for 24h by acquiring the PA images at 1h, 6h and 24h. Looking at the scDb-hERG1/β1-ICG PA signal intensity, we can see that for both tumors the signal is very weak at the first hour and becomes higher at the sixth hour (*Fig.33*).

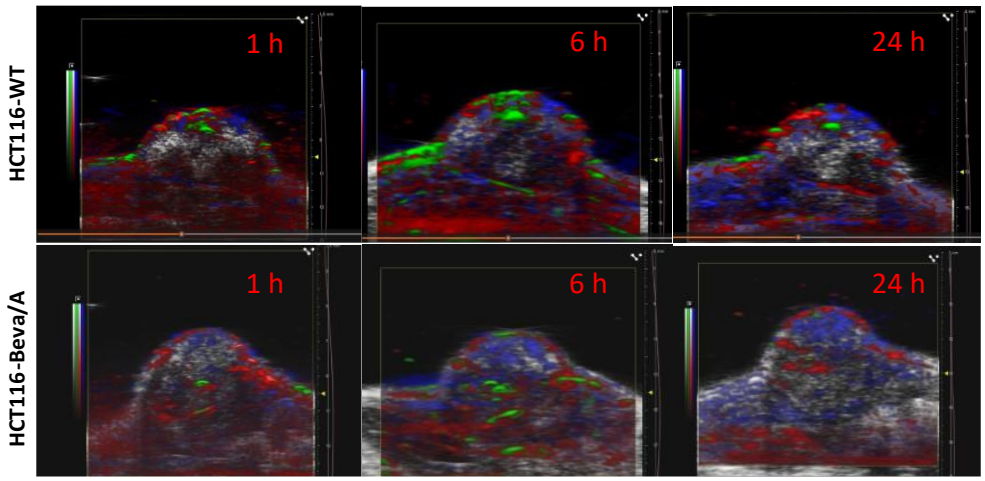

Figure 33 PA imaging. Evaluation in time of scDb-hERG1/B1 conjugated with ICGgreen in time for either HCT116-WT and HCT116-Beva/A derived tumor masses. Green areas show the signal of scDb-hERG1/B1 conjugated with ICGgreen, while red areas indicate the presence of oxyhemoglobin and blue areas show the presence of deoxyhemoglobin.

We can see the signal coming from the inside of the tumor masses, showing the tumor site specificity of the diabody. The signal at 24 hours is similar to the low signal image at 1 hour indicating the wash out of the antibody from the tumor after 24 hours.

4.2.8 *Effects of the scDb-hERG1/β1*

Once demonstrated the penetration of scDb-hERG1/β1 into the tumor masses of both cell lines, we then evaluated the *in vivo* efficacy of the diabody. For instance, we used the same workflow as seen for the treatment with Beva, with the only difference being that in this case, scDb-hERG1/β1 was administered i.v. daily at 16mg/kg. We also performed the same analysis such as Tumor growth, oxygenation levels, and perfusion.

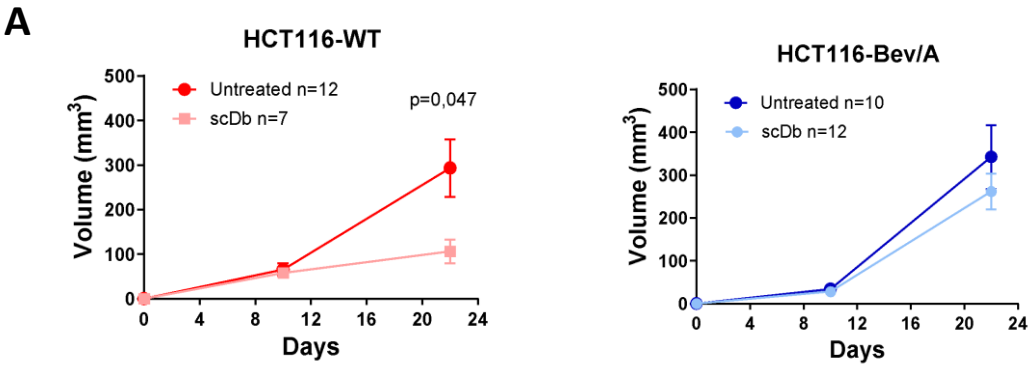

Figure 34 Tumor growth in time for the two different tumor models: Dark red and Dark blue lines represent untreated group of HCT116-WT and HCT116-Beva/A respectively, while the lighter lines the scDb-hERG1/ β1 treatment.

Starting from the Tumor growth, we observed differences in the response to the treatment between the two models (*Fig.34*). HCT116-WT mouse model displays a statistically significant reduction of the Tumor masses (p=0.047) compared to the control group. Although slight differences can be observed also in HCT116-Beva/A between the control and treated groups, a significant difference is not reached. The impact on the two different models is very high, where HCT116-WT and HCT116-Beva/A display a mean volume at the endpoint of 101.9 mm^3 ± 14.52 mm^3 and 262.1mm^3 ± 20.44 mm^3 respectively. For both models, we observed the same impact on the HV (*Fig.35B*) of the treatment, where a significant increase is encountered compared both to the control group (HCT116-WT untreated/treated p=0.082; HCT116-Beva/A untreated/treated p=0.02).

Observing oxygenation, the differences in response to the treatment between the two models reappeared. HCT116-WT shows an increase in both sO_{2TOT} and sO_{2P} (*Fig.35C,D*) despite only in the case of sO_{2P} we can appreciate a higher increase on oxygenation levels (from 56.9% of the untreated to 71.8% of the treated) which is also statistically significant (p=0.001).

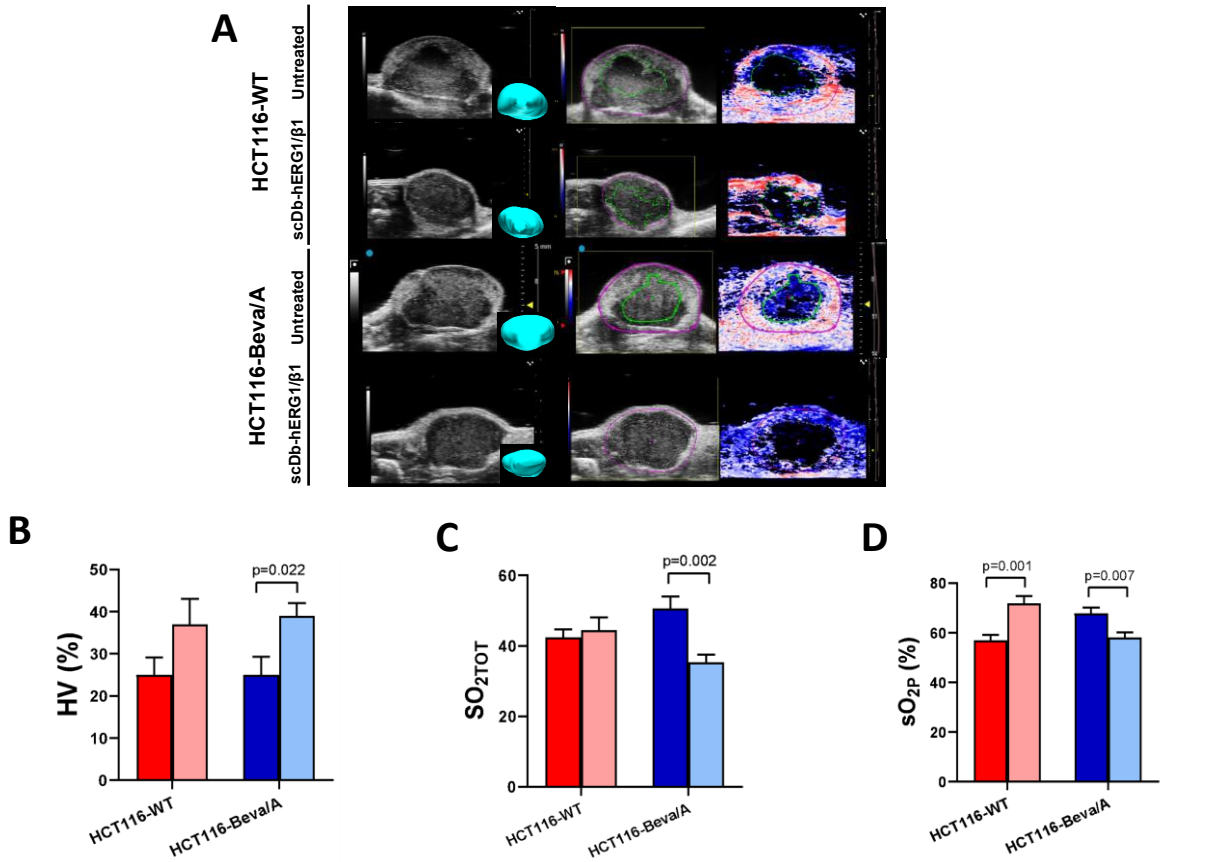

Figure 35 (A) US and PA imaging for HCT116-WT and HCT116-Beva/A: Imaging comparison of untreated vs treated. Barplot comparison between untreated and scDb-hERG1/ β1 treated on both Tumor models for HV (B), sO_{2TOT} (c), and sO_{2P} (d). Dark red and Dark blue bar represents untreated group of HCT116-WT and HCT116-Beva/A respectively, while the lighter bar the scDb-hERG1/ β1 treatment.

In the case of HCT116-Beva/A, both sO_{2TOT} and sO_{2P} tend to decrease in the treatment group compared to the control group (*Fig.35C,D*). Especially, in both parameters, the reduction was statistically significant (p= 0.002 sO_{2TOT}; p= 0.007 sO_{2P}), and a higher

reduction is observed in the case of sO_{2TOT} (from 50.7% of the untreated to 35.4% of the treated).

Moving to the perfusion, the masses display similar trends based on the treatment. For PE (*Fig.36A*) and PI (*Fig.36E*), scDb-hERG1/β1 provides an increase in those parameters, while we observe a decrease in mTT (*Fig.36C*) and AUC (*Fig.36D*). TTP has a different trend compared to the treatment of the two models; where in the case of HCT116-WT a slight increase can be observed, in HCT116-Beva/A we observed a decrease.

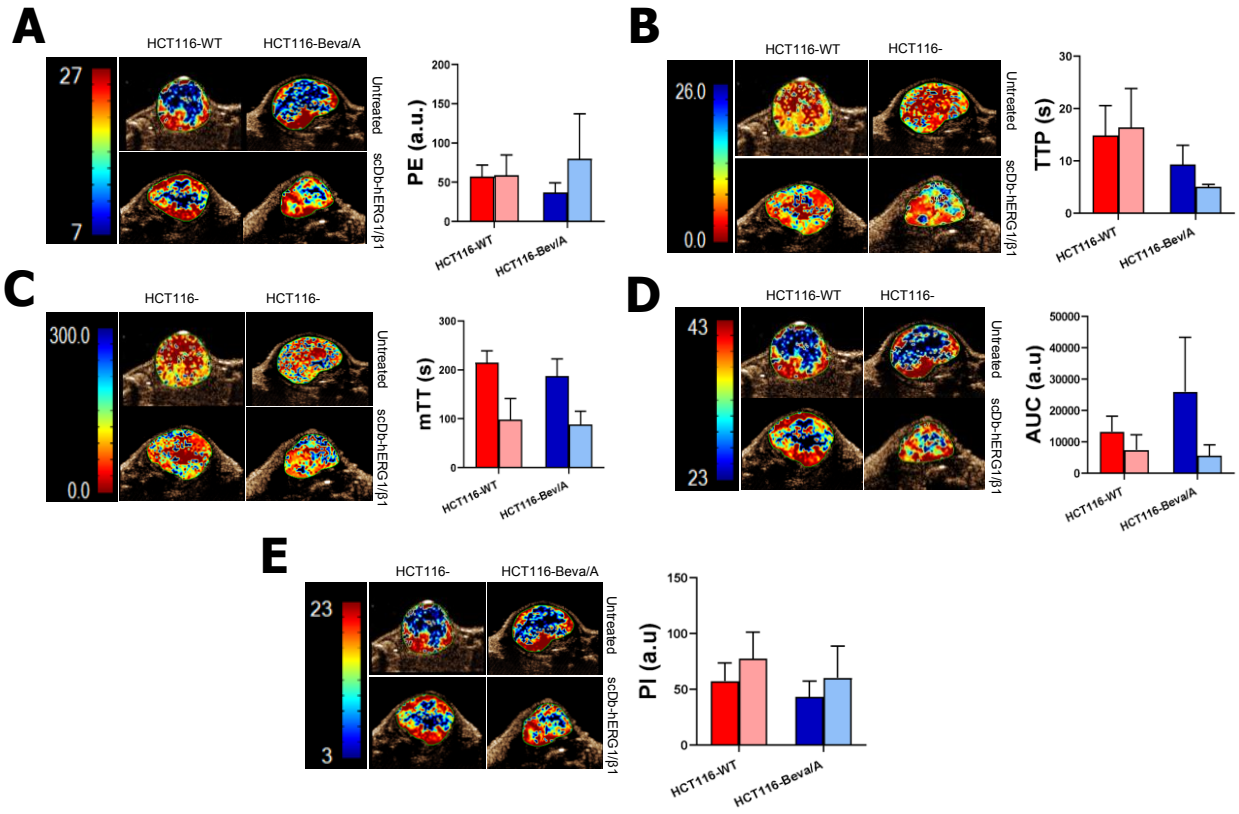

Figure 36 Nonlinear contrast imaging on HCT116-WT and HCT116-Beva/A cell lines treated with scDb-hERG1/ β1. For each parameters obtained, a representative image and the comparison between the two tumors-derived cell lines have been reported. (A) Peak Enhancement (PE); (B) Time to Peak (TTP);(C) Mean Transit Time (mTT); (D) the Area under the curve; (E) Perfusion Index (PI). Dark red and dark blue represent HCT116-WT and HCT116-Beva/A untreated, while the lighter colors represent their treated counterpart.

These results evidence the same trend as seen for Bevacizumab treatment on

perfusion parameters, where PE, PI, and mTT increase on both, underlying an improvement of the treatment in overall perfusion.

4.2.9 *Effects of the combination Bevacizumab + scDb-hERG1/β1*

After evaluating the single treatment of scDb-hERG1/β1 and Bevacizumab, we proceed to assess how the combinatory treatment affects the masses obtained from either HCT 116-WT or HCT 116-Beva/A cells. For the therapeutic schedule, we used the same protocol as for the single treatments, by administering 10 mg/kg Beva intravenously twice a week and 16 mg/kg scDb-hERG1/β1 i.v. daily.

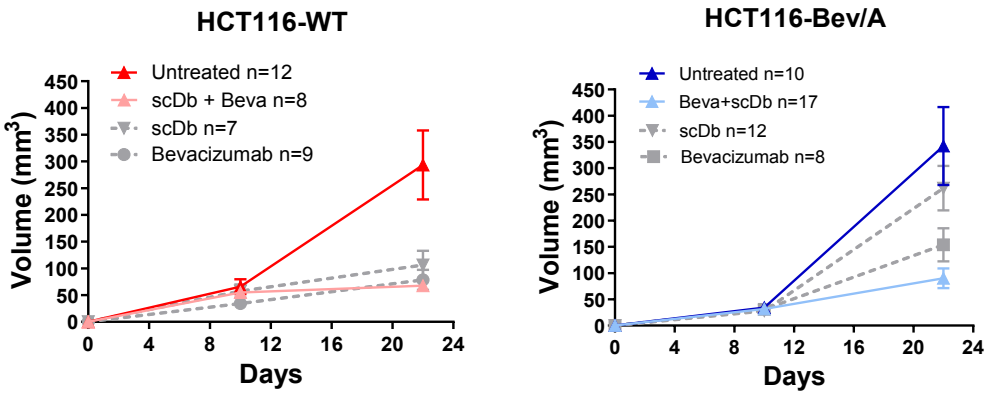

Figure 37 Tumor growth in time for the two different tumor models: Dark red and Dark blue lines represent untreated group of HCT116-WT and HCT116-Beva/A respectively, while the lighter lines the scDb-hERG1/ β1+Bevacizumab treatment. Grey lines represent treatments alone: scDb-hERG1/ β1 (triangle point), Bevacizumab (square point).

The dual treatment provides a significant reduction in tumor growth of either HCT116-WT (mean tumor mass=54.7 mm^3 ± 11.14 mm^3) and HCT116-Beva/A tumor masses (mean tumor mass= 90.3 mm^3 ± 10.14 mm^3, compared to their untreated counterparts (HCT116-WT p=0.01; HCT116-Beva/A p=0.0004), but differences emerge when compared to monotherapy treatments (*Fig.37*). Although the combination provides a reduction in HCT116-WT, it's not significantly different from the single treatments (101.9 mm^3 ± 14.52 and 72.3 ± 16.24 mm^3 for scDb-hERG1/β1 and Bevacizumab, respectively). On the contrary, on HCT 116-Beva/A tumor masses

provided a higher reduction compared to single treatments (262.1 mm^3 ± 20.44 mm^3 and 130.7 mm^3 ± 15.36 mm^3 for scDb-hERG1/β1 and Bevacizumab, respectively), although statistical significance was reached only when compared to scDb-hERG1/β1 (p=0.003) (*Fig.37).* Furthermore, in masses derived from HCT 116-WT cells, a marked increase in HV emerged in comparison to the untreated condition (from 25% to 38%) and Beva alone (from 19% to 38%), but not in comparison to treatment with scDb-hERG1/β1 (*Fig.38B*).

Comparing the combination-treated HCT-116-Beva/A masses to their untreated counterpart, there were no effects on HV (from 25% to 27%); however, when

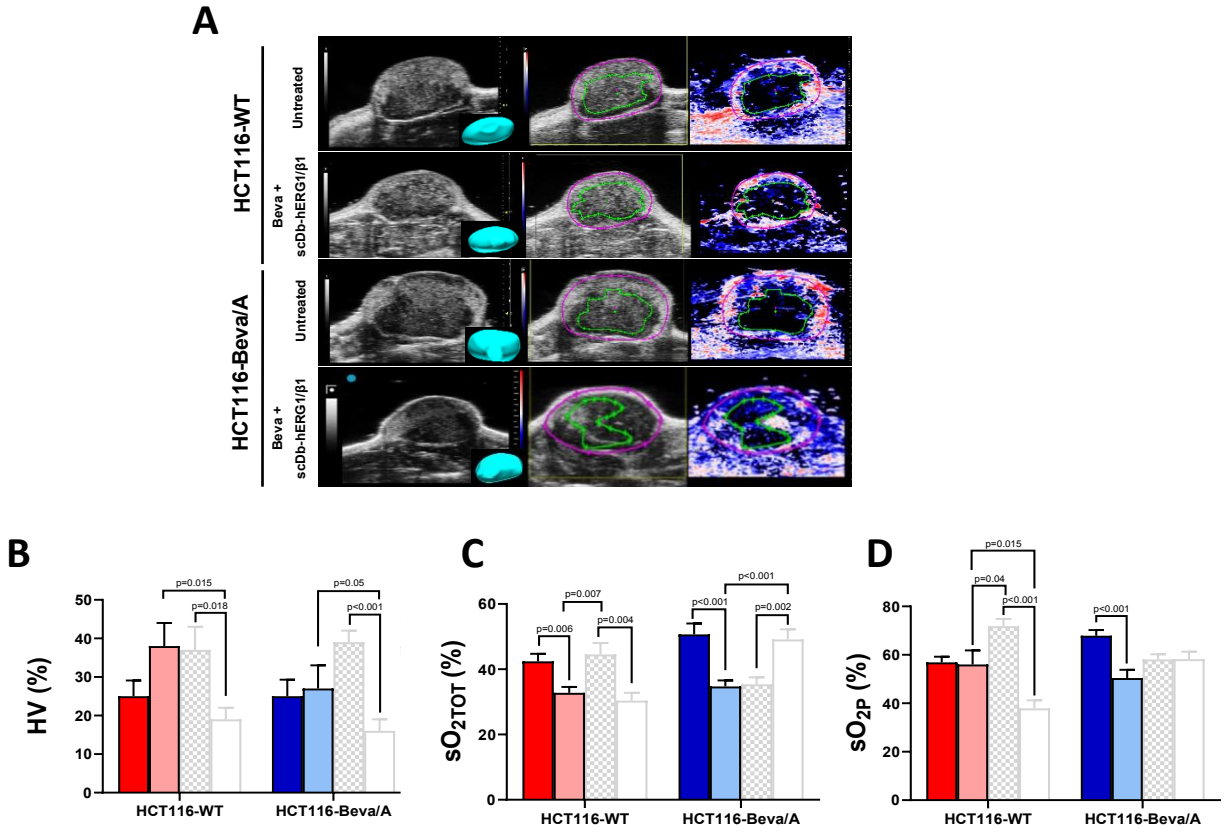

Figure 38 (A) US and PA imaging for HCT116-WT and HCT116-Beva/A: Imaging comparison of untreated vs treated. Barplot comparison between untreated and scDb-hERG1/ β1 +Beva treated on both Tumor models for HV (B), sO_{2TOT} (c), and sO_{2P} (d). Dark red and blue bar represents untreated group of HCT116-WT and HCT116-Beva/A respectively, while the lighter bar the scDb-hERG1/ β1 +Beva treatment. Grey bar represents treatments alone: scDb-hERG1/ β1 (filled bar), Bevacizumab (empty bar).

compared to monotherapy, there were two distinct trends: the combination treatment showed a decrease in HV (from 39% to 27%, p=0.07) when compared to scDb-hERG1/β1 alone, but an increase in HV (from 16.5% to 27%, p=0.05) when compared to Bevacizumab (*Fig.38B*).

Moreover, the mice's masses from the combined treatment group of HCT116-WT demonstrated a statistically significant decrease in sO_{2P} (sO_{2P} = 56%) when compared to the scDb-hERG1/β1 group (sO_{2P} = 71.8%; p=0.037) and a significant increase in oxygenation when compared to the Bevacizumab group (sO_{2P} = 37.9%; p=0.015), but no difference when compared to the untreated group (sO_{2P} = 56.9%) (*Fig.38D*). Looking at sO_{2TOT}, the oxygenation decreases when comparing combinatory treatments (sO_{2TOT} = 32.7%) with the scDb-hERG1/β1 group (sO_{2TOT} = 44.5%; p=0.007), while no differences emerged with Bevacizumab alone (sO_{2TOT} = 30.4%). In that case, also we register a significantly decrease in sO_{2TOT} by comparing to the untreated group (sO_{2TOT} = 42.4%; p=0.006) (*Fig.38C*).

On the contrary, the combined treatment with scDb-hERG1/β1 and Beva decreased sO_{2P} in masses obtained from HCT 116-Beva/A cells (sO_{2P} = 50.4%, compared to all the other conditions (sO_{2P}: untreated=67.9%; scDb-hERG1/β1 = 58.1%; Bevacizumab = 58.2%), despite the significant is only registered in comparison with untreated group (p<0.001) (*Fig.38D*). Looking at the sO_{2TOT} (sO_{2TOT} = 34.7%), we observed a higher reduction effect, and we reached significance by comparison with untreated (sO_{2TOT} = 50.7%; p<0.001) and Beva group (sO_{2TOT} = 49.1%; p<0.001) (*Fig.38C*).

These diverging results would indicate that, besides all else, combined treatment efficacy with scDb-hERG1/β1 and Bevacizumab depends likewise on whether a tumor is resistant or sensitive to Bevacizumab. Indeed, in the Bevacizumab-resistant HCT 116-Beva/A, the combined treatment caused a more pronounced decline of the tumor volume and significant diminution of both peripheral and total oxygenation compared with the untreated and single-agent-treated groups, thus suggesting a higher impact of oxygen depletion. Conversely, the combination therapy in Bevacizumab-sensitive HCT 116-WT tumors does not provide a substantial improvement in tumor reduction

or oxygenation compared to the individual treatments, underscoring the influence of Bevacizumab resistance on the therapeutic response.

Moving on to the perfusion parameters, in masses derived from HCT 116-WT cells, the combined treatment with scDb-hERG1/β1 and Beva had nearly no impact on perfusion metrics compared to untreated circumstances. However, a reduction in TTP and PI has been observed, as compared to the other treatments, which were either Beva or scDb-hERG1/β1 alone.

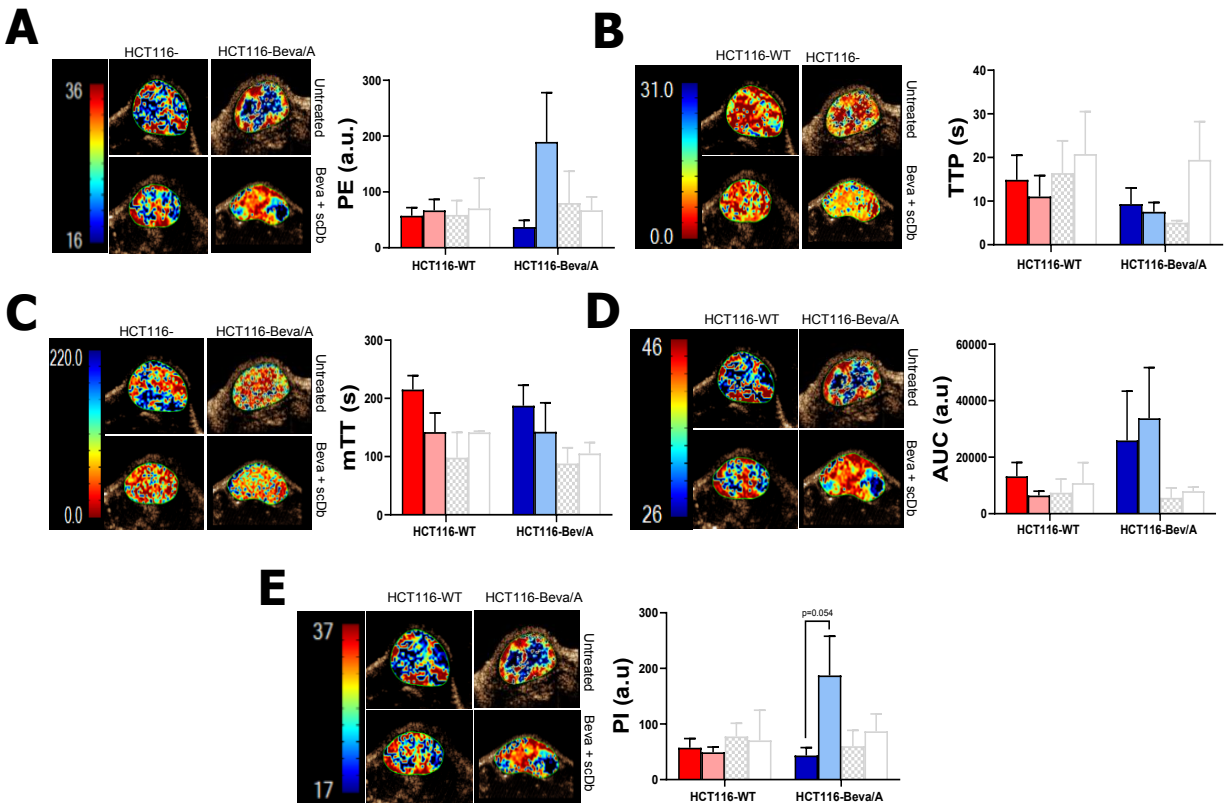

Figure 39 Nonlinear contrast imaging on HCT116-WT and HCT116-Beva/A cell lines treated with scDb-hERG1/ β1 + Bevacizumab. For each parameters obtained, a representative image and the comparison between the two tumors-derived cell lines have been reported. (A) Peak Enhancement (PE); (B) Time to Peak (TTP);(C) Mean Transit Time (mTT); (D) the Area under the curve; (E) Perfusion Index (PI). Dark red and blue represent HCT116-WT and HCT116-Beva/A untreated, while the lighter colors represent their treated counterpart. Grey bar represents treatments alone: scDb-hERG1/ β1 (filled bar), Bevacizumab (empty bar).

Conversely, the combination treatment of Beva and scDb-hERG1/β1 had significant effects on masses derived from HCT 116-Beva/A cells. Specifically, there was an

increase in PI and PE (PE: untreated=37.4 a.u, scDb-hERG1/β1+Bevacizumab= 189.6) (*Fig.39A,E*) and, to a lesser degree, in AUC compared to all the groups (*Fig.39D*). For PI, we reach also statistically significant differences by comparing them to the untreated group (PI: untreated= 43.3 a. u, scDb-hERG1/β1+Bevacizumab= 187.5 a.u; p=0.05). A decrease in TTP and mTT also emerged (*Fig.39B,C*). All those data suggest an increase in blood flow efficiency and improved perfusion, especially in HCT116-Beva/A tumoral models in response to combinatory treatment, where an additive effect can be observed in PE and PI.

5. Discussion

Preclinical studies play a vital role in cancer research; however, about 90% of drugs fail during trials[21,25]. Much stricter standards should be set in preclinical settings to reduce failure rates. These are the development of *in vivo* models that recapitulate hallmarks of cancer[66,70], new therapeutic interventions[46,185,186], and valid methods for the identification and follow-up of tumors[131,132,141,143,150].
In this research, we focused on these challenges using the Vevo F2 LAZR-X system, a multimodal imaging station that combines photoacoustic and ultrasound technology, to generate new orthotopic mouse models a monitor the effect of innovative therapeutic strategies.
We established models of both pancreatic ductal adenocarcinoma (PDAC)[14,176] and colorectal cancer (CRC)[15,17], as these are highly lethal and aggressive malignancies with a high unmet clinical need.

Initially, we established orthotopic xenograft PDAC models using ultrasound-guided injection of PANC-1 tumor cells into the pancreas of athymic nude mice. These models exhibit several advantages, most notably slow cellular engraftment and slow growth of tumor masses. This makes them excellent models for drug testing, as they allow the identification of the starting point for therapy and adequate monitoring over time. The procedure that was performed is also consistent with the 3R principle[187], as we have improvements in reduction, due to improved statistics with a small group of animals, and refinement, due to a minimally invasive technique that is easier to perform than classical surgery. This approach successfully generated tumors in 80% of the mice, offering a reliable platform for therapeutic evaluation.

Therefore, these new models were used to test a new therapeutic strategy, scDb-hERG/β1 in combination with sub-therapeutic doses of gemcitabine to evaluate its impact on tumor growth. Photoacoustic imaging outcomes demonstrated that the

scDb-hERG1/β1 antibody effectively targeted PDAC tumors when conjugated with ICG, further validating its potential as a precision therapeutic approach. The target specificity observed *in vivo* supports the feasibility of integrating therapeutic strategies with scDb-hERG1/β1, prompting us to test the antibody in the PDAC mouse model. scDb-hERG1/β1 showed promising results if administrated in combination with sub-therapeutic doses of gemcitabine (5 mg/kg), the standard of care for PDAC treatment. While gemcitabine alone at lower doses exhibited limited efficacy, the combination therapy showed antitumor effects comparable to the therapeutic dose of gemcitabine (25 mg/kg), reducing tumor growth.

We also observed an effect on survival. Mice treated with 25 mg/kg of Gemcitabine showed severe signs of suffering, and at the endpoint, displayed ascites and abnormal liver in 30% of cases, confirming the side-effects of the treatment. In the groups treated with scDb-hERG1-β1 alone and in combination with 5 mg/kg Gemcitabine, no cases of ascites or abnormal liver were observed. In addition, general signs of distress, such as abnormal posture and reduced mobility, were observed later than in the control group and the 25 mg/kg Gemcitabine group.

However, the orthotopic PANC-1 mouse model allowed for successful therapeutic evaluation, it lacked the representation desmoplastic stroma of PDAC, an essential feature of the tumor microenvironment that strongly contributes to therapeutic resistance and disease progression[182,183]. To better mimic the TME, we developed an improved model that include both tumor cells (PANC-1) and stromal cells (RLT-PSC) To this purpose we performed US-guided injection of a bolus containing PANC-1 and RLT-PSC cells. The RLT-PSC cells support the TME through their secretion of collagen, fibronectin and other components of the extracellular matrix, providing nutritional support and promoting metastatic events. Therefore, RLT-PSC cells recapitulate the dense stroma characteristic of human PDAC through which it assembles collagen, thus establishing a hypoxic treatment-resistant tumor microenvironment[188].

On account of that, we established four groups of orthotopic PDACs which differ in PANC-1 and RLT-PSC cell content (i) PANC-1; (ii) RLT-PSC; (iii) a 1:1 ratio of PANC-1 and RLT-PSC and a 1:5 ratio of PANC-1 and RLT-PSC. All the tumors developed from the injection exhibited similar growth rate, while those derived from PANC-1/RLT-PSC cells in a 1:5 ratio tended to grow more slowly. Furthermore, sO_2% values for those mixed tumors were the lowest among the groups, indicating a higher level of tumor hypoxia.

Therefore, when the tumor perfusion index was analyzed through CE-US, a coherent relation between hypoxia data and tumor perfusion could be established. The tumors developed by the PANC-1/RLT-PSC 1:5 ratio, having lower tumor oxygen saturation, also had lower blood perfusion in the mass. Moreover, the metastatic capability of PANC-1 cells *in vivo* appears to be enhanced by the presence of stellate cells, where both PANC1/RLT-PSC ratio 1:1 and 1:5 groups showed distance metastasis beyond just the local disease. In particular, lesions were detected in the liver, a site commonly affected in PDAC patients.

This novel US-guided injection of a mixed cell population, comprising both tumor cells and stromal cells, represents an advance in the orthotopic PDAC modelas it closely resemble the physiological and pathological condition of pancreatic cancer.

Our next step was to evaluate the effectiveness of the scDb-hERG/β1 antibody as a novel strategy targeting angiogenesis in colorectal cancer (CRC). The hERG1/β1 complex, through the activation of the PI3K-Akt pathway, which in turn results in an increased expression of proinflammatory cytokines like VEGF-A and other genes involved in tumor progression, has also been linked to angiogenesis in CRC[178,189]. Anti-VEGF-A monoclonal antibody Bevacizumab has been the oldest applied angiogenesis treatments in several cancers, including CRC[36,190]. In the great majority of such treatments, however, resistance mechanisms eventually manifest themselves.

Herein, we utilized the HCT116-WT and HCT116-Beva/A (Bevacizumab-adapted) cell line pairs for the evaluation of changes in angiogenesis-related signaling upon various treatments

By analyzing the two cell lines *in vitro* for key genes involved during angiogenesis we obtained similar results. Although Bevacizumab-resistant lines were used, there were no differences in mRNA or protein expression of either, suggesting that adaptation to Bevacizumab did not significantly alter key regulatory mechanisms. This stability suggests that although HCT116-Beva/A cells may be resistant to the anti-angiogenic effects of Bevacizumab, the fundamental mechanisms driving angiogenesis remain intact. The introduction of scDb-hERG/β1 caused a significant increase in VEGF-A secretion when analyzed with ELISA, especially in the Bevacizumab-adapted HCT116-Beva/A cells, where VEGF-A levels almost doubled compared to the untreated counterpart. Combinations with Bevacizumab further diminished VEGF-A expression in both cell lines, suggesting that these two agents may complement. These findings provide insight into how the cells behave *in vitro*, exhibiting nearly identical circumstances in terms of angiogenesis-related gene expression and treatment response.

Despite that, passing on *in vivo* conditions we highlight differences between the two cellular models and their response to anti-angiogenic therapies. Although subcutaneous mouse models for HCT116-WT and HCT116-Beva/A display similar tumor growth in time, reaching also the same mean Tumor volume at the endpoint (day 22), the oxygenation status of the tumors displayed important differences. HCT116-Beva/A tumors exhibited higher values for both sO_{2TOT} and sO_{2P} compared to HCT116-WT. The increase in sO_{2P} approached statistical significance ($p=0.01$), suggesting that Bevacizumab adaptation may enhance oxygenation in the periphery of the tumor.

Ex vivo analysis for HIF-1α and VEGF-A expression reinforced this finding, revealing that the Bevacizumab-resistant tumors had lower HIF-1α and VEGF-A levels compared to the wild-type counterpart. The significant correlation between HIF-1α and VEGF-A expression indicates that hypoxia-driven signaling persists as a dominant driver of

angiogenesis in HCT116. Looking at the total hemoglobin content within the tumor masses we observed the same amount between the two tumoral models, suggesting that, as HCT116-Beva/A displays a more peripheral oxygenated region, vascular network might be altered in the structure and function of blood vessels, and this seems to fit with perfusion parameters, where the general trend of lower PE, PI, TTP, and mTT values suggests a potential reduction in blood flow efficiency. The lack of differences in the number of vessels between the two models' data indicates the possibility that the variation is caused by more leaky, branching or unstable vessels, supported by the oxygenation and perfusion parameters. Also, combining IHC with CE-US information, higher HIF-1α and VEGF-A levels, and PE, PI, TTP, and mTT in HCT116-WT evidence not only a better-perfused situation, but in contrast an increase in the complex and the disorganization of the vascular network, probably as the result of the action of VEGF-A which influenced increased permeability and the formation of new tortuous capillaries.

These data emphasize the importance of evaluating angiogenesis *in vivo* in tumor models. Tumor microenvironmental factors, such as vessel leakiness or oxygen status are key determinants that cannot be properly recapitulated *in vitro*, where differences don't emerge. Also, photoacoustic imaging and CE-US played a key role in detecting the subtle changes in tumor oxygenation, hemoglobin content, and perfusion parameters between the two models, elucidating the impact of acquired Bevacizumab resistance on the tumor vasculature. The integrated analysis of multiple parameters that characterize primary aspects of tumor development (such as neoangiogenesis and hypoxia), through the study of tumor perfusion or oxygen saturation, may lead to a better characterization of aspects that promote tumor aggressiveness and allow the identification of multifactorial targets to develop new therapeutic approaches[112,126,140,191].

As the models showed differences, both were analysed for response to different types of treatment: Bevacizumab, scDb-hERG1/β1, and the combination.

As expected, Bevacizumab administered as monotherapy resulted in reduced tumor mass growth for both lines, consistent with the fact that Bevacizumab reduces formation and normalizes vessels. Noteworthy, although it has an effect on Bevacizumab-resistant tumors, its effect is significantly less, and this presumably results from adaptation mechanisms to Bevacizumab that are mitigated *in vivo* This is also appreciated observing the oxygen saturation and necrotic volume, that are mainteinedat high levels in the peripheral area and on the entire tumor, moreover, has been observed a greater reduction in necrotic volume.
In the wild-type model, Bevacizumab knocks down both peripheral and total oxygenation, highlighting that Bevacizumab-resistant tumors maintain a more robust vascular network, potentially through alternative pro-angiogenic pathways. From perfusion outcomes, we see that the impact of treatment is nonetheless similar, as there are no differences between the two lines among the various parameters analyzed, and statistically significant differences within the treatment itself. Although, the increase in PI, PE and reduced mTT indicate the role of Bevacizumab in improving tumoral perfusion (PI and PE) and in normalizing vessels (mTT)[185].

Conversely, monotherapy with the scDb-hERG1/β1 showed different effects when comparing the two models. In the Bevacizumab-resistant HCT116-Beva/A tumors, scDb-hERG1/β1 showed a reduced impact on tumor growth but increased tumor oxygenation. This could suggest that while scDb-hERG1/β1 effectively targets angiogenic pathways, Bevacizumab-resistant tumors have alternative mechanisms sustaining their growth and vascular supply.
Perfusion parameters show the same changes as seen for Bevacizumab treatment, with an increase in PE, PI, and a decrease in mTT, evidence that scDb-hERG1/ β1 is still affecting tumor vascular function and underlying an improvement in overall perfusion.

The combination of Bevacizumab/scDb-hERG1/β1 was tried in search of a possible synergistic or combinatory action, especially in Bevacizumab-resistant tumors. In HCT116-WT, we obtained a reduced tumor volume of 54.7 mm^3; however, this difference was not statistically significant when compared to the effect of either Bevacizumab or scDb-hERG1/β1 alone, demonstrating poor additional benefit in Bevacizumab-sensitive tumors. In the case of the combination treatment in HCT116-Beva/A, tumor volume was reduced to 90.3 mm^3, encountering statistical significance when compared to all the other treatment groups; this suggests that such a combination may overcome the resistance to Bevacizumab. Noteworthy, oxygenation parameters yielded striking differences with combination therapy. This had a more profound effect in the HCT116-Beva/A tumors on the sO_{2TOT} and sO_{2P} values: both of these decreased significantly, indicative of increased tumor hypoxia consequent to increased tumor cell death with subsequent abnormal vessel collapse. This is further supported by the perfusion parameters that had shown the effect of the combination treatment in Bevacizumab-resistant tumors.

Increased values for both PE and PI suggested improved blood flow upon treatment, possibly as a consequence of vascular remodeling action because of combined inhibition of the angiogenesis pathways. A slight reduction in mTT and TTP also suggests improved blood flow efficiency in the tumor. Noteworthy, if compared to monotherapy, combinatory treatment provides a higher increase in the differences in all the parameters, showing how it can be a useful set-up to increase overall perfusion and efficient blood flow, restoring normal vasculature. Since the combined treatment (scDb-hERG1/β1+Bevacizumab) increases tumor perfusion in Bevacizumab adapted tumors, this type of treatment can be considered in combination therapy with chemotherapeutic agents to promote greater transport of the chemotherapeutic agent within the tumor and improve its effect.

These data show the translational value of novel imaging modalities, such as US and PAI for the testing of new therapeutic approaches against PDAC and CRC[126,131]. The

use of scDb-hERG1/β1 in combination with current therapies is the most promising approach, in particular in those conditions characterized by resistance to traditional treatments such as Gemcitabine or Bevacizumab[31,192].

Ultrasound imaging, exploiting different modes (B-Mode and CE-US) allows to obtain more sophisticated and representative *in vivo* models with a higher degree of complexity regarding the tumor microenvironment. Also, they allow for the real-time monitoring of tumor growth providing important insights into underlying biological processes such as angiogenesis and vascular dynamics-areas that are especially difficult to investigate using *in vitro* methods. The introduction of r contrast agents allows for a deeper investigation of the tumor's characteristics. Parameters such as oxygenation, perfusion dynamics, and vascular integrity provide a deeper interpretation of therapeutic effects and mechanisms of action of treatments, opening new perspectives in therapeutic approaches and preclinical testing, offering more insight and more reliable prediction of clinical outcomes.

6. Bibliography

1. WHO report on cancer: setting priorities, investing wisely and providing ... - World Health Organization - Google Libri. Accessed August 19, 2024. https://books.google.it/books?hl=it&lr=&id=anYOEQAAQBAJ&oi=fnd&pg=PA6&ots=N3E_nDH2MI&sig=ZyIsvbEeQ7gqOVuijvI6Tjj0kwE&redir_esc=y#v=onepage&q&f=false
2. Bray Bsc F, Laversanne | Mathieu, Hyuna |, et al. Global cancer statistics 2022: GLOBOCAN estimates of incidence and mortality worldwide for 36 cancers in 185 countries. *CA Cancer J Clin*. 2024;74(3):229-263. doi:10.3322/CAAC.21834
3. Fitzgerald RC, Antoniou AC, Fruk L, Rosenfeld N. The future of early cancer detection. doi:10.1038/s41591-022-01746-x
4. Gheorghe G, Bungau S, Ilie M, et al. diagnostics Early Diagnosis of Pancreatic Cancer: The Key for Survival. doi:10.3390/diagnostics10110869
5. Das S, Kundu M, Jena BC, Mandal M. Causes of cancer: physical, chemical, biological carcinogens, and viruses. *Biomaterials for 3D Tumor Modeling*. Published online January 1, 2020:607-641. doi:10.1016/B978-0-12-818128-7.00025-3
6. Stein CJ, Colditz GA. Modifiable risk factors for cancer. *Br J Cancer*. 2004;90(2):299. doi:10.1038/SJ.BJC.6601509
7. Moleyar-Narayana P, Leslie SW, Ranganathan S. Cancer Screening. *StatPearls*. Published online May 31, 2024. Accessed August 19, 2024. https://www.ncbi.nlm.nih.gov/books/NBK563138/
8. Debela DT, Muzazu SGY, Heraro KD, et al. New approaches and procedures for cancer treatment: Current perspectives. *SAGE Open Med*. 2021;9. doi:10.1177/20503121211034366
9. Kern SE, Hruban RH, Hidalgo M, Yeo CJ. An Introduction to Pancreatic Adenocarcinoma Genetics, Pathology and Therapy. *Cancer Biol Ther*. 2002;1(6):607-613. doi:10.4161/cbt.307
10. Nakaoka K, Ohno E, Kawabe N, et al. Current Status of the Diagnosis of Early-Stage Pancreatic Ductal Adenocarcinoma. *Diagnostics*. 2023;13(2). doi:10.3390/DIAGNOSTICS13020215
11. Guillén-Ponce C, Blázquez J, González I, de-Madaria E, Montáns J, Carrato A. Diagnosis and staging of pancreatic ductal adenocarcinoma. *Clinical and Translational Oncology*. 2017;19(10):1205-1216. doi:10.1007/s12094-017-1681-7
12. Zhen DB, Rabe KG, Gallinger S, et al. BRCA1, BRCA2, PALB2, and CDKN2A mutations in familial pancreatic cancer: a PACGENE study. *Genetics in Medicine*. 2015;17(7):569-577. doi:10.1038/gim.2014.153
13. Khomiak A, Brunner M, Kordes M, et al. Recent Discoveries of Diagnostic, Prognostic and Predictive Biomarkers for Pancreatic Cancer. *Cancers (Basel)*. 2020;12(11):3234. doi:10.3390/cancers12113234
14. Collisson EA, Bailey P, Chang DK, Biankin A V. Molecular subtypes of pancreatic cancer. *Nat Rev Gastroenterol Hepatol*. 2019;16(4):207-220. doi:10.1038/s41575-019-0109-y

15. Duan B, Zhao Y, Bai J, et al. Colorectal Cancer: An Overview. *Gastrointestinal Cancers*. Published online September 30, 2022:1-12. doi:10.36255/EXON-PUBLICATIONS-GASTROINTESTINAL-CANCERS-COLORECTAL-CANCER
16. Baran B, Mert Ozupek N, Yerli Tetik N, Acar E, Bekcioglu O, Baskin Y. Difference Between Left-Sided and Right-Sided Colorectal Cancer: A Focused Review of Literature. *Gastroenterology Res*. 2018;11(4):264-273. doi:10.14740/gr1062w
17. Colorectal Cancer Stages | Rectal Cancer Staging | Colon Cancer Staging | American Cancer Society. Accessed September 19, 2024. https://www.cancer.org/cancer/types/colon-rectal-cancer/detection-diagnosis-staging/staged.html
18. Zhang L, Shay JW. Multiple Roles of APC and its Therapeutic Implications in Colorectal Cancer. Published online 2017. doi:10.1093/jnci/djw332
19. Poulogiannis G, Frayling IM, Arends MJ. DNA mismatch repair deficiency in sporadic colorectal cancer and Lynch syndrome. *Histopathology*. 2010;56(2):167-179. doi:10.1111/j.1365-2559.2009.03392.x
20. Yang Z, Zhang X, Bai X, Xi X, Liu W, Zhong W. Anti-angiogenesis in colorectal cancer therapy. *Cancer Sci*. 2024;115(3):734-751. doi:10.1111/cas.16063
21. Sun D, Gao W, Hu H, Zhou S. Why 90% of clinical drug development fails and how to improve it? *Acta Pharm Sin B*. 2022;12(7):3049-3062. doi:10.1016/j.apsb.2022.02.002
22. Takebe T, Imai R, Ono S. The Current Status of Drug Discovery and Development as Originated in United States Academia: The Influence of Industrial and Academic Collaboration on Drug Discovery and Development. *Clin Transl Sci*. 2018;11(6):597. doi:10.1111/CTS.12577
23. Dowden H, Munro J. Trends in clinical success rates and therapeutic focus. *Nat Rev Drug Discov*. 2019;18(7):495-496. doi:10.1038/D41573-019-00074-Z
24. Hingorani AD, Kuan V, Finan C, et al. improving the odds of drug development success through human genomics: modelling study. *Scientific RepoRtS* /. 2019;9:18911. doi:10.1038/s41598-019-54849-w
25. Mahalmani V, Sinha S, Prakash A, Medhi B. Translational research: Bridging the gap between preclinical and clinical research. *Indian J Pharmacol*. 2022;54(6):393-396. doi:10.4103/ijp.ijp_860_22
26. Lisa AVE, Vinci V, Galtelli L, et al. Outpatient Nonmelanoma Skin Cancer Excision and Reconstruction: A Clinical, Economical, and Patient Perception Analysis. *Plast Reconstr Surg Glob Open*. 2022;10(1):e3925-e3925. doi:10.1097/GOX.0000000000003925
27. Vasan N, Baselga J, Hyman DM. A view on drug resistance in cancer. *Nature 2019 575:7782*. 2019;575(7782):299-309. doi:10.1038/s41586-019-1730-1
28. Mokhtari RB, Homayouni TS, Baluch N, et al. Combination therapy in combating cancer. *Oncotarget*. 2017;8(23):38022. doi:10.18632/ONCOTARGET.16723
29. Tong H, Fan Z, Liu B, Lu T. The benefits of modified FOLFIRINOX for advanced pancreatic cancer and its induced adverse events: a systematic review and meta-analysis OPEN. *Scientific RepoRts* /. 2018;8:8666. doi:10.1038/s41598-018-26811-9
30. Thibodeau S, Voutsadakis IA. FOLFIRINOX Chemotherapy in Metastatic Pancreatic Cancer: A Systematic Review and Meta-Analysis of Retrospective and Phase II Studies. *J Clin Med*. 2018;7(1). doi:10.3390/JCM7010007

31. Principe DR, Underwood PW, Korc M, Trevino JG, Munshi HG, Rana A. The Current Treatment Paradigm for Pancreatic Ductal Adenocarcinoma and Barriers to Therapeutic Efficacy. *Front Oncol*. 2021;11:688377. doi:10.3389/FONC.2021.688377/BIBTEX
32. Law MF, Chan HN, Kong SY, et al. Clinical outcomes of patients with acute lymphoblastic leukemia receiving the hyper-CVAD regimen and assessment of the risk of hepatitis flares due to hepatitis B virus reactivation after chemotherapy. *Arch Med Sci*. 2022;18(1):121. doi:10.5114/AOMS/103606
33. Schuster C, Eikesdal HP, Puntervoll H, et al. Clinical Efficacy and Safety of Bevacizumab Monotherapy in Patients with Metastatic Melanoma: Predictive Importance of Induced Early Hypertension. doi:10.1371/journal.pone.0038364
34. Cervantes A, Prager GW. FOLFOXIRI plus bevacizumab as standard of care for first-line treatment in patients with advanced colon cancer. *ESMO Open*. 2023;8(2):100883. doi:10.1016/j.esmoop.2023.100883
35. Garcia J, Hurwitz HI, Sandler AB, et al. Bevacizumab (Avastin®) in cancer treatment: A review of 15 years of clinical experience and future outlook. *Cancer Treat Rev*. 2020;86:102017. doi:10.1016/j.ctrv.2020.102017
36. Olive DL. Bevacizumab: antiangiogenic cancer therapy. *Drugs Today (Barc)*. 2005;41(1):23-26. doi:10.1358/DOT.2005.41.1.875776
37. Biller LH, Schrag D. Diagnosis and Treatment of Metastatic Colorectal Cancer: A Review. *JAMA*. 2021;325(7):669-685. doi:10.1001/JAMA.2021.0106
38. Xie YH, Chen YX, Fang JY. Comprehensive review of targeted therapy for colorectal cancer. *Signal Transduction and Targeted Therapy 2020 5:1*. 2020;5(1):1-30. doi:10.1038/s41392-020-0116-z
39. Charmsaz S, Collins DM, Perry AS, Prencipe M. Novel Strategies for Cancer Treatment: Highlights from the 55th IACR Annual Conference. *Cancers (Basel)*. 2019;11(8). doi:10.3390/CANCERS11081125
40. Debela DT, Muzazu SGY, Heraro KD, et al. New approaches and procedures for cancer treatment: Current perspectives. *SAGE Open Med*. 2021;9. doi:10.1177/20503121211034366
41. Fan D, Cao Y, Cao M, Wang Y, Cao Y, Gong T. Nanomedicine in cancer therapy. *Signal Transduction and Targeted Therapy 2023 8:1*. 2023;8(1):1-34. doi:10.1038/s41392-023-01536-y
42. Liu B, Cao W, Cheng J, et al. Human natural killer cells for targeting delivery of gold nanostars and bimodal imaging directed photothermal/photodynamic therapy and immunotherapy. *Cancer Biol Med*. 2019;16(4):756-770. doi:10.20892/j.issn.2095-3941.2019.0112
43. Taher M, Susanti D, Haris MS, et al. PEGylated liposomes enhance the effect of cytotoxic drug: A review. *Heliyon*. 2023;9(3):e13823. doi:10.1016/j.heliyon.2023.e13823
44. Shams F, Golchin A, Azari A, et al. Nanotechnology-based products for cancer immunotherapy. *Mol Biol Rep*. 2022;49(2):1389. doi:10.1007/S11033-021-06876-Y
45. Chehelgerdi M, Chehelgerdi M, Allela OQB, et al. Progressing nanotechnology to improve targeted cancer treatment: overcoming hurdles in its clinical implementation. *Mol Cancer*. 2023;22(1):169. doi:10.1186/S12943-023-01865-0
46. Zahavi D, Weiner L. Monoclonal Antibodies in Cancer Therapy. *Antibodies*. 2020;9(3):1-20. doi:10.3390/ANTIB9030034

47. Lu LL, Suscovich TJ, Fortune SM, Alter G. Beyond binding: antibody effector functions in infectious diseases. *Nature Publishing Group*. 2017;18. doi:10.1038/nri.2017.106
48. Smaglo BG, Aldeghaither D, Weiner LM. The development of immunoconjugates for targeted cancer therapy. doi:10.1038/nrclinonc.2014.159
49. Singh A, Xu J, Mattheolabakis G, Amiji M. EGFR-targeted gelatin nanoparticles for systemic administration of gemcitabine in an orthotopic pancreatic cancer model. *Nanomedicine*. 2016;12(3):589-600. doi:10.1016/J.NANO.2015.11.010
50. Dummer RG, Mony JT, Otsuka A, Seidel JA, Kabashima K. Anti-PD-1 and Anti-CTLA-4 Therapies in Cancer: Mechanisms of Action, efficacy, and Limitations. *Article 86 1 Oncol*. 2018;8:86. doi:10.3389/fonc.2018.00086
51. Pierpont TM, Limper CB, Richards KL. Past, Present, and Future of Rituximab—The World's First Oncology Monoclonal Antibody Therapy. *Front Oncol*. 2018;8(JUN):163. doi:10.3389/FONC.2018.00163
52. Li R, Liang M, Liang X, Yang L, Su M, Lai KP. Chemotherapeutic Effectiveness of Combining Cetuximab for Metastatic Colorectal Cancer Treatment: A System Review and Meta-Analysis. *Front Oncol*. 2020;10:868. doi:10.3389/FONC.2020.00868
53. Pegram MD, Slamon DJ. Combination therapy with trastuzumab (Herceptin) and cisplatin for chemoresistant metastatic breast cancer: evidence for receptor-enhanced chemosensitivity. *Semin Oncol*. 1999;26(4 Suppl 12):89-95.
54. Muñoz-López P, Ribas-Aparicio RM, Becerra-Báez EI, et al. Single-Chain Fragment Variable: Recent Progress in Cancer Diagnosis and Therapy. *Cancers (Basel)*. 2022;14(17). doi:10.3390/CANCERS14174206
55. Barbosa de Aguiar R, de Almeida da Silva T, Andrade Costa B, et al. Generation and functional characterization of a single-chain variable fragment (scFv) of the anti-FGF2 3F12E7 monoclonal antibody. *Scientific Reports* /. 123AD;11:1432. doi:10.1038/s41598-020-80746-8
56. McGonigle P, Ruggeri B. Animal models of human disease: Challenges in enabling translation. *Biochem Pharmacol*. 2014;87(1):162-171. doi:10.1016/j.bcp.2013.08.006
57. Animal Models & Translational Medicine: Quality and Reproducibility of Experimental Design | AISAL Symposium. *Comp Med*. 2018;68(1):84-94.
58. Percie Du Sertid N, Ahluwaliaid A, Alamid S, et al. Reporting animal research: Explanation and elaboration for the ARRIVE guidelines 2.0. Published online 2020. doi:10.1371/journal.pbio.3000411
59. Subramanian U. Validation of Animal Models. In: *Introduction to Basics of Pharmacology and Toxicology*. Springer Nature Singapore; 2022:157-170. doi:10.1007/978-981-19-5343-9_12
60. Willner P. The validity of animal models of depression. *Psychopharmacology (Berl)*. 1984;83(1):1-16. doi:10.1007/BF00427414/METRICS
61. Bailey J. Does the stress of laboratory life and experimentation on animals adversely affect research data? A critical review. *Altern Lab Anim*. 2018;46(5):291-305. doi:10.1177/026119291804600501
62. Samsa G, Samsa L. A Guide to Reproducibility in Preclinical Research. *Acad Med*. 2019;94(1):47-52. doi:10.1097/ACM.0000000000002351

63. Polson AG, Fuji RN. The successes and limitations of preclinical studies in predicting the pharmacodynamics and safety of cell-surface-targeted biological agents in patients. *Br J Pharmacol*. 2012;166(5):1600. doi:10.1111/J.1476-5381.2012.01916.X
64. Grimm H, Biller-Andorno N, Buch T, et al. Advancing the 3Rs: innovation, implementation, ethics and society. *Front Vet Sci*. 2023;10:1185706. doi:10.3389/fvets.2023.1185706
65. Morton CL, Houghton PJ. Establishment of human tumor xenografts in immunodeficient mice. *Nat Protoc*. 2007;2(2):247-250. doi:10.1038/NPROT.2007.25
66. Zhang W, Fan W, Rachagani S, et al. comparative Study of Subcutaneous and orthotopic Mouse Models of prostate cancer: Vascular perfusion, Vasculature Density, Hypoxic Burden and BB2r-Targeting Efficacy. doi:10.1038/s41598-019-47308-z
67. Chicote I, Cámara JA, Palmer HG. Advanced Colorectal Cancer Orthotopic Patient-Derived Xenograft Models for Cancer and Stem Cell Research. *Methods in Molecular Biology*. 2020;2171:321-329. doi:10.1007/978-1-0716-0747-3_22
68. Okano M, Oshi M, Butash A, et al. Orthotopic Implantation Achieves Better Engraftment and Faster Growth Than Subcutaneous Implantation in Breast Cancer Patient-Derived Xenografts. doi:10.1007/s10911-020-09442-7
69. Sharma S, Van der Jeught K, Zhou Z, Zhang X, Lu X. Abstract 13: A non-surgical approach to develop an orthotopic colorectal cancer mouse model. *Cancer Res*. 2023;83(7_Supplement):13-13. doi:10.1158/1538-7445.AM2023-13
70. Kersten K, De Visser KE, Van Miltenburg MH, Jonkers J. Genetically engineered mouse models in oncology research and cancer medicine. doi:10.15252/emmm.201606857
71. Yin L, Wang XJ, Chen DX, Liu XN, Wang XJ. Humanized mouse model: a review on preclinical applications for cancer immunotherapy. *Am J Cancer Res*. 2020;10(12):4568-4584. Accessed August 19, 2024. www.ajcr.us/
72. Liu Y, Wu W, Cai C, Zhang H, Shen H, Han Y. Patient-derived xenograft models in cancer therapy: technologies and applications. doi:10.1038/s41392-023-01419-2
73. Chemotherapy of human tumor xenografts in genetically athymic mice. Accessed August 19, 2024. https://www.annclinlabsci.org/content/8/1/50?ijkey=473119ccf1a7018ed9ca627cfc750ae0204ffe0d&keytype2=tf_ipsecsha
74. Goodale D, Phay C, Postenka CO, Keeney M, Allan AL. Characterization of tumor cell dissemination patterns in preclinlcal models of cancer metastasis using flow cytometry and laser scanning cytometry. *Cytometry Part A*. 2009;75(4):344-355. doi:10.1002/CYTO.A.20657
75. Meng X, Yang F, Dong H, Dou L, Zhang X. Recent advances in optical imaging of biomarkers in vivo. *Nano Today*. 2021;38:101156. doi:10.1016/J.NANTOD.2021.101156
76. Rattner J, Bathe OF. metabolites H OH OH Monitoring for Response to Antineoplastic Drugs: The Potential of a Metabolomic Approach. Published online 2017. doi:10.3390/metabo7040060
77. Collins DJ, Padhani AR. Dynamic magnetic resonance imaging of tumor perfusion. *IEEE Engineering in Medicine and Biology Magazine*. 2004;23(5):65-83. doi:10.1109/MEMB.2004.1360410

78. Schwenck J, Sonanini D, Cotton JM, et al. nature reviews cancer Check for updates Advances in PET imaging of cancer. *Nature Reviews Cancer* /. 2023;23:474-490. doi:10.1038/s41568-023-00576-4
79. Pharaon R, Koczywas MA, Salgia S, Mohanty A, Massarelli E. Biomarkers in immunotherapy: literature review and future directions. *J Thorac Dis*. 2020;12(9):5119-5127. doi:10.21037/JTD.2020.04.15
80. Faivre C, El Cheikh R, Barbolosi D, Barlesi F. Mathematical optimisation of the cisplatin plus etoposide combination for managing extensive-stage small-cell lung cancer patients. Published online 2017. doi:10.1038/bjc.2016.439
81. Andersson E, Hult J, Troein C, et al. Facilitating clinically relevant skin tumor diagnostics with spectroscopy-driven machine learning. *iScience*. 2024;27(5):109653. doi:10.1016/J.ISCI.2024.109653
82. Galldiks N, Kaufmann TJ, Vollmuth P, et al. Challenges, limitations, and pitfalls of PET and advanced MRI in patients with brain tumors: A report of the PET/RANO group. *Neuro Oncol*. 2024;26(7):1181-1194. doi:10.1093/NEUONC/NOAE049
83. Pysz MA, Gambhir SS, Willmann JK. Molecular Imaging: Current Status and Emerging Strategies. *Clin Radiol*. 2010;65(7):500. doi:10.1016/J.CRAD.2010.03.011
84. Mankoff DA. A definition of molecular imaging. *J Nucl Med*. 2007;48(6):18N, 21N.
85. Peterson TE, Manning HC. Molecular imaging: 18F-FDG PET and a whole lot more. *J Nucl Med Technol*. 2009;37(3):151-161. doi:10.2967/jnmt.109.062729
86. Weissleder R, Mahmood U. Molecular Imaging. *Radiology*. 2001;219(2):316-333. doi:10.1148/radiology.219.2.r01ma19316
87. Pysz MA, Gambhir SS, Willmann JK. Molecular imaging: current status and emerging strategies. *Clin Radiol*. 2010;65(7):500-516. doi:10.1016/j.crad.2010.03.011
88. Bai JW, Qiu SQ, Zhang GJ. Molecular and functional imaging in cancer-targeted therapy: current applications and future directions. doi:10.1038/s41392-023-01366-y
89. Israel O, Pellet O, Biassoni L, et al. Two decades of SPECT/CT – the coming of age of a technology: An updated review of literature evidence. *Eur J Nucl Med Mol Imaging*. 2019;46(10):1990. doi:10.1007/S00259-019-04404-6
90. Schwenck J, Sonanini D, Cotton JM, et al. Advances in PET imaging of cancer. *Nature Reviews Cancer 2023 23:7*. 2023;23(7):474-490. doi:10.1038/s41568-023-00576-4
91. Rahmim A, Zaidi H. Pet versus spect: Strengths, limitations and challenges. *Nucl Med Commun*. 2008;29(3):193-207. doi:10.1097/MNM.0B013E3282F3A515
92. Neumann D, Kollorz E. Ultrasound. *Lecture Notes in Computer Science (including subseries Lecture Notes in Artificial Intelligence and Lecture Notes in Bioinformatics)*. 2018;11111 LNCS:237-249. doi:10.1007/978-3-319-96520-8_11
93. Sezer N, Koç M. A comprehensive review on the state-of-the-art of piezoelectric energy harvesting. *Nano Energy*. 2021;80:105567. doi:10.1016/J.NANOEN.2020.105567
94. Carovac A, Smajlovic F, Junuzovic dzelaludin. Application of Ultrasound in Medicine. *Medicine Review | AIM*. 2011;19(3):168-171. doi:10.5455/aim.2011.19.168-171
95. Patey SJ, Corcoran JP. Physics of ultrasound. *Anaesthesia & Intensive Care Medicine*. 2021;22(1):58-63. doi:10.1016/J.MPAIC.2020.11.012

96. Hooi FM, Kripfgans O, Carson PL. Acoustic attenuation imaging of tissue bulk properties with a priori information. *J Acoust Soc Am*. 2016;140(3):2113. doi:10.1121/1.4962983
97. Suetens P. Ultrasound imaging. *Fundamentals of Medical Imaging*. Published online August 6, 2009:128-158. doi:10.1017/CBO9780511596803.007
98. Stecco A, Pirri C, Caro R De, Raghavan P. Stiffness and echogenicity: Development of a stiffness-echogenicity matrix for clinical problem solving. *Eur J Transl Myol*. 2019;29(3):8476. doi:10.4081/ejtm.2019.8476
99. What Does Echogenic Mean On Ultrasound? – Radiology In Plain English. Accessed August 19, 2024. https://radiologyinplainenglish.com/echogenic-ultrasound/
100. Ihnatsenka B, Boezaart AP. Ultrasound: Basic understanding and learning the language. *Int J Shoulder Surg*. 2010;4(3):55. doi:10.4103/0973-6042.76960
101. Bianchi S. Ultrasound and bone: a pictorial review. *J Ultrasound*. 2020;23:227-257. doi:10.1007/s40477-020-00477-4
102. Smereczyński A, Kołaczyk K. Pitfalls in ultrasound imaging of the stomach and the intestines. *J Ultrason*. 2018;18:207-211. doi:10.15557/JoU.2018.0031
103. Das N, Kumar Praharaj M, Panda S. Exploring ultrasonic wave transmission in liquids and liquid mixtures: A comprehensive overview. *J Mol Liq*. 2024;403:124841. doi:10.1016/j.molliq.2024.124841
104. Frinking PJA, Bouakaz A, Kirkhorn J, Ten Cate FJ, De Jong N. Ultrasound contrast imaging: current and new potential methods. *Ultrasound Med Biol*. 2000;26(6):965-975. doi:10.1016/S0301-5629(00)00229-5
105. Bruce M, Hannah A, Hammond R, et al. High-Frequency Nonlinear Doppler Contrast-Enhanced Ultrasound Imaging of Blood Flow. *IEEE Trans Ultrason Ferroelectr Freq Control*. 2020;67(9):1776-1784. doi:10.1109/TUFFC.2020.2986486
106. Shah A, Irshad A. Sonography Doppler Flow Imaging Instrumentation. *StatPearls*. Published online May 1, 2023. Accessed August 20, 2024. https://www.ncbi.nlm.nih.gov/books/NBK580539/
107. Magee P. Essential notes on the physics of Doppler ultrasound. *BJA Educ*. 2020;20(4):112. doi:10.1016/J.BJAE.2020.01.003
108. Oglat AA, Matjafri MZ, Suardi N, Oqlat MA, Abdelrahman MA, Oqlat AA. A Review of Medical Doppler Ultrasonography of Blood Flow in General and Especially in Common Carotid Artery. *J Med Ultrasound*. 2018;26(1):3-13. doi:10.4103/JMU.JMU_11_17
109. Bruce M, Hannah A, Hammond R, et al. High-Frequency Nonlinear Doppler Contrast-Enhanced Ultrasound Imaging of Blood Flow. *IEEE Trans Ultrason Ferroelectr Freq Control*. 2020;67(9):1776-1784. doi:10.1109/TUFFC.2020.2986486
110. Averkiou MA, Bruce MF, Powers JE, Sheeran PS, Burns PN. Imaging Methods for Ultrasound Contrast Agents. *Ultrasound Med Biol*. 2020;46(3):498-517. doi:10.1016/J.ULTRASMEDBIO.2019.11.004
111. Eisenbrey JR, Sridharan A, Liu J Bin, Forsberg F. Recent Experiences and Advances in Contrast-Enhanced Subharmonic Ultrasound. *Biomed Res Int*. 2015;2015. doi:10.1155/2015/640397
112. Cosgrove D, Lassau N. Imaging of perfusion using ultrasound. *Eur J Nucl Med Mol Imaging*. 2010;37(S1):65-85. doi:10.1007/s00259-010-1537-7

113. McDonald DM, Choyke PL. Imaging of angiogenesis: from microscope to clinic. *Nature Medicine 2003 9:6*. 2003;9(6):713-725. doi:10.1038/nm0603-713
114. Siphanto RI, Thumma KK, Kolkman RGM, et al. Serial noninvasive photoacoustic imaging of neovascularization in tumor angiogenesis. *Opt Express*. 2005;13(1):89-95. doi:10.1364/opex.13.000089
115. Ferrara KW, Merritt CR, Burns PN, Foster FS, Mattrey RF, Wickline SA. Evaluation of tumor angiogenesis with US: imaging, Doppler, and contrast agents. *Acad Radiol*. 2000;7(10):824-839. doi:10.1016/s1076-6332(00)80631-5
116. Farajollahi A, Baharvand M. Advancements in photoacoustic imaging for cancer diagnosis and treatment. *Int J Pharm*. 2024;665:124736. doi:10.1016/J.IJPHARM.2024.124736
117. Lin L, Wang L V. The emerging role of photoacoustic imaging in clinical oncology. *Nature Reviews Clinical Oncology 2022 19:6*. 2022;19(6):365-384. doi:10.1038/s41571-022-00615-3
118. Liu X, Li H, Pang M, et al. Photoacoustic imaging in brain disorders: Current progress and clinical applications. *View*. 2024;5(4):20240023. doi:10.1002/VIW.20240023
119. Lin L, Wang L V. The emerging role of photoacoustic imaging in clinical oncology. *Nature Reviews Clinical Oncology 2022 19:6*. 2022;19(6):365-384. doi:10.1038/s41571-022-00615-3
120. Gargiulo S, Albanese S, Mancini M. State-of-the-Art Preclinical Photoacoustic Imaging in Oncology: Recent Advances in Cancer Theranostics. *Contrast Media Mol Imaging*. 2019;2019. doi:10.1155/2019/5080267
121. Valluru KS, Wilson KE, Willmann JK. Photoacoustic Imaging in Oncology: Translational Preclinical and Early Clinical Experience. *Radiology*. 2016;280(2):332. doi:10.1148/RADIOL.16151414
122. Steinberg I, Huland DM, Vermesh O, Frostig HE, Tummers WS, Gambhir SS. Photoacoustic clinical imaging. *Photoacoustics*. 2019;14:77. doi:10.1016/J.PACS.2019.05.001
123. Lin L, Wang L V. The emerging role of photoacoustic imaging in clinical oncology. *Nature Reviews Clinical Oncology 2022 19:6*. 2022;19(6):365-384. doi:10.1038/s41571-022-00615-3
124. Tsang VTC, Li X, Wong TTW. A Review of Endogenous and Exogenous Contrast Agents Used in Photoacoustic Tomography with Different Sensing Configurations. doi:10.3390/s20195595
125. Siphanto RI, Thumma KK, Kolkman RGM, et al. Serial noninvasive photoacoustic imaging of neovascularization in tumor angiogenesis. *Optics Express, Vol 13, Issue 1, pp 89-95*. 2005;13(1):89-95. doi:10.1364/OPEX.13.000089
126. Gerling M, Zhao Y, Nania S, et al. Real-time assessment of tissue hypoxia in vivo with combined photoacoustics and high-frequency ultrasound. *Theranostics*. 2014;4(6):604-613. doi:10.7150/thno.7996
127. Fakhoury JW, Lara JB, Manwar R, et al. Photoacoustic imaging for cutaneous melanoma assessment: a comprehensive review. *J Biomed Opt*. 2024;29(Suppl 1). doi:10.1117/1.JBO.29.S1.S11518
128. Lavaud J, Henry M, Gayet P, et al. Noninvasive monitoring of liver metastasis development via combined multispectral photoacoustic imaging and fluorescence diffuse optical tomography. *Int J Biol Sci*. 2020;16(9):1616. doi:10.7150/IJBS.40896
129. Sano K, Ohashi M, Kanazaki K, et al. In vivo photoacoustic imaging of cancer using indocyanine green-labeled monoclonal antibody targeting the epidermal growth factor receptor. *Biochem Biophys Res Commun*. 2015;464(3):820-825. doi:10.1016/J.BBRC.2015.07.042

130. Zanganeh S, Li H, Kumavor PD, et al. Photoacoustic imaging enhanced by indocyanine green-conjugated single-wall carbon nanotubes. *J Biomed Opt*. 2013;18(9):096006. doi:10.1117/1.JBO.18.9.096006
131. Mallidi S, Watanabe K, Timerman D, Schoenfeld D, Hasan T. Prediction of Tumor Recurrence and Therapy Monitoring Using Ultrasound-Guided Photoacoustic Imaging. *Theranostics*. 2015;5(3):289-301. doi:10.7150/THNO.10155
132. Rich LJ, Seshadri M. Photoacoustic monitoring of tumor and normal tissue response to radiation. *Sci Rep*. 2016;6. doi:10.1038/SREP21237
133. Jin Y, Yin Y, Li C, Liu H, Shi J. Non-Invasive Monitoring of Human Health by Photoacoustic Spectroscopy. *Sensors (Basel)*. 2022;22(3). doi:10.3390/S22031155
134. Capozza M, Blasi F, Valbusa G, et al. Photoacoustic imaging of integrin-overexpressing tumors using a novel ICG-based contrast agent in mice. *Photoacoustics*. 2018;11:36-45. doi:10.1016/J.PACS.2018.07.007
135. Valluru KS, Willmann JK. Clinical photoacoustic imaging of cancer. *Ultrasonography*. 2016;35(4):267-280. doi:10.14366/USG.16035
136. Gerling M, Zhao Y, Nania S, et al. Real-time assessment of tissue hypoxia in vivo with combined photoacoustics and high-frequency ultrasound. *Theranostics*. 2014;4(6):604-613. doi:10.7150/thno.7996
137. Yang J, Zhang G, Li Q, et al. Photoacoustic imaging for the evaluation of early tumor response to antivascular treatment. *Quant Imaging Med Surg*. 2019;9(2):160. doi:10.21037/QIMS.2018.11.06
138. Lugano R, Ramachandran M, Dimberg A. Tumor angiogenesis: causes, consequences, challenges and opportunities. *Cell Mol Life Sci*. 2020;77(9):1745. doi:10.1007/S00018-019-03351-7
139. Teleanu RI, Chircov C, Grumezescu AM, Teleanu DM. Tumor Angiogenesis and Anti-Angiogenic Strategies for Cancer Treatment. *J Clin Med*. 2019;9(1):84. doi:10.3390/jcm9010084
140. Zhang W, Fan W, Rachagani S, et al. Comparative Study of Subcutaneous and Orthotopic Mouse Models of Prostate Cancer: Vascular Perfusion, Vasculature Density, Hypoxic Burden and BB2r-Targeting Efficacy. *Scientific Reports 2019 9:1*. 2019;9(1):1-10. doi:10.1038/s41598-019-47308-z
141. Liu X, Gao R, Chen · Chiyun, et al. Noninvasive photoacoustic computed tomography/ultrasound imaging for the identification of high-risk atherosclerotic plaques. *Eur J Nucl Med Mol Imaging*. doi:10.1007/s00259-022-05911-9
142. Kuczynski EA, Yin M, Bar-Zion A, et al. Co-option of Liver Vessels and Not Sprouting Angiogenesis Drives Acquired Sorafenib Resistance in Hepatocellular Carcinoma. Published online 2016. doi:10.1093/jnci/djw030
143. Zhou HC, Chen N, Zhao H, et al. Optical-resolution photoacoustic microscopy for monitoring vascular normalization during anti-angiogenic therapy. *Photoacoustics*. 2019;15:100143. doi:10.1016/J.PACS.2019.100143
144. Pan D, Pramanik M, Senpan A, et al. Molecular photoacoustic imaging of angiogenesis with integrin-targeted gold nanobeacons. *The FASEB Journal • Research Communication*. doi:10.1096/fj.10-171728
145. Menger MM, Bauer D, Bleimehl M, et al. Sildenafil, a phosphodiesterase-5 inhibitor, stimulates angiogenesis and bone regeneration in an atrophic non-union model in mice. *J Transl Med*. 2023;21(1):1-16. doi:10.1186/S12967-023-04441-8/FIGURES/9

146. Okumura K, Yoshida K, Yoshioka K, et al. Photoacoustic imaging of tumour vascular permeability with indocyanine green in a mouse model. doi:10.1186/s41747-018-0036-7
147. Xu Z, Pan Y, Chen N, et al. Visualizing tumor angiogenesis and boundary with polygon-scanning multiscale photoacoustic microscopy. *Photoacoustics*. 2022;26:100342. doi:10.1016/J.PACS.2022.100342
148. Weinman O, Babic D, Regli L, et al. Quantitative assessment of angiogenesis, perfused blood vessels and endothelial tip cells in the postnatal mouse brain. *Nat Protoc*. Published online 2014. doi:10.1038/nprot.2015.002
149. Gao X, Gao M, Gorecka J, et al. Human-Induced Pluripotent Stem-Cell-Derived Smooth Muscle Cells Increase Angiogenesis to Treat Hindlimb Ischemia. 2021;10:792. doi:10.3390/cells10040792
150. Mueller-Diesing F, Lederle W, Rix A, et al. Molecular Ultrasound Imaging Depicts the Modulation of Tumor Angiogenesis by Acetylsalicylic Acid. *Int J Mol Sci*. 2023;24(8):7060. doi:10.3390/ijms24087060
151. Wang T, Dong Y, Huang Z, et al. Antioxidants stimulate BACH1-dependent tumor angiogenesis. *J Clin Invest*. 2023;133(20). doi:10.1172/JCI169671
152. Aronson JK, Ferner RE. Biomarkers—A General Review. *Curr Protoc Pharmacol*. 2017;76(1). doi:10.1002/cpph.19
153. Strimbu K, Tavel JA. What are Biomarkers? *Curr Opin HIV AIDS*. 2010;5(6):463. doi:10.1097/COH.0B013E32833ED177
154. Luo G, Jin K, Deng S, et al. Roles of CA19-9 in pancreatic cancer: Biomarker, predictor and promoter. *Biochim Biophys Acta Rev Cancer*. 2021;1875(2). doi:10.1016/J.BBCAN.2020.188409
155. Gao Y, Wang J, Zhou Y, Sheng S, Qian SY, Huo X. Evaluation of Serum CEA, CA19-9, CA72-4, CA125 and Ferritin as Diagnostic Markers and Factors of Clinical Parameters for Colorectal Cancer. *Scientific Reports 2018 8:1*. 2018;8(1):1-9. doi:10.1038/s41598-018-21048-y
156. Lakemeyer L, Sander S, Wittau M, Henne-Bruns D, Kornmann M, Lemke J. Diagnostic and Prognostic Value of CEA and CA19-9 in Colorectal Cancer. *Diseases*. 2021;9(1). doi:10.3390/DISEASES9010021
157. Ogunwobi OO, Mahmood F, Akingboye A. Biomarkers in Colorectal Cancer: Current Research and Future Prospects. *Int J Mol Sci*. 2020;21(15):1-20. doi:10.3390/IJMS21155311
158. Alexander S, Mathie A, Peters J. Ion Channels. *Br J Pharmacol*. 2011;164(Suppl 1):S137. doi:10.1111/J.1476-5381.2011.01649_5.X
159. Lastraioli E, Iorio J, Arcangeli A. Ion channel expression as promising cancer biomarker. *Biochim Biophys Acta*. 2015;1848(10 Pt B):2685-2702. doi:10.1016/J.BBAMEM.2014.12.016
160. He S, Moutaoufik MT, Islam S, et al. HERG channel and cancer: A mechanistic review of carcinogenic processes and therapeutic potential. *Biochimica et Biophysica Acta (BBA) - Reviews on Cancer*. 2020;1873(2):188355. doi:10.1016/J.BBCAN.2020.188355
161. Curran ME, Splawski I, Timothy KW, Vincen GM, Green ED, Keating MT. A molecular basis for cardiac arrhythmia: HERG mutations cause long QT syndrome. *Cell*. 1995;80(5):795-803. doi:10.1016/0092-8674(95)90358-5
162. Sanguinetti MC. HERG1 channel agonists and cardiac arrhythmia. *Curr Opin Pharmacol*. 2014;15(1):22-27. doi:10.1016/J.COPH.2013.11.006

163. Arcangeli A. Expression and role of hERG channels in cancer cells. *Novartis Found Symp*. 2005;266:225-232. doi:10.1002/047002142x.ch17
164. Lastraioli E, Lottini T, Bencini L, Bernini M, Arcangeli A. hERG1 Potassium Channels: Novel Biomarkers in Human Solid Cancers. *Biomed Res Int*. 2015;2015. doi:10.1155/2015/896432
165. Muratori L, Petroni G, Antonuzzo L, et al. hERG1 positivity and Glut-1 negativity identifies high-risk TNM stage I and II colorectal cancer patients, regardless of adjuvant chemotherapy. *Onco Targets Ther*. 2016;9:6325-6332. doi:10.2147/OTT.S114090
166. Liu F, Wu Q, Dong Z, Liu K. Integrins in cancer: Emerging mechanisms and therapeutic opportunities. *Pharmacol Ther*. 2023;247:108458. doi:10.1016/J.PHARMTHERA.2023.108458
167. Sun L, Guo S, Xie Y, Yao Y. The characteristics and the multiple functions of integrin β1 in human cancers. *J Transl Med*. 2023;21(1):787. doi:10.1186/s12967-023-04696-1
168. Becchetti A, Crescioli S, Zanieri F, et al. The conformational state of hERG1 channels determines integrin association, downstream signaling, and cancer progression. *Sci Signal*. 2017;10(473). doi:10.1126/SCISIGNAL.AAF3236
169. Becchetti A, Petroni G, Arcangeli A. Ion Channel Conformations Regulate Integrin-Dependent Signaling. *Trends Cell Biol*. 2019;29(4):298-307. doi:10.1016/j.tcb.2018.12.005
170. Feng J, Yu J, Pan X, et al. HERG1 functions as an oncogene in pancreatic cancer and is downregulated by miR-96. *Oncotarget*. 2014;5(14):5832-5844. doi:10.18632/ONCOTARGET.2200
171. Crociani O, Zanieri F, Pillozzi S, et al. hERG1 channels modulate integrin signaling to trigger angiogenesis and tumor progression in colorectal cancer. *Sci Rep*. 2013;3. doi:10.1038/SREP03308
172. Su L, Hu Z, Yang YG. Role of CXCR4 in the progression and therapy of acute leukaemia. *Cell Prolif*. 2021;54(7). doi:10.1111/CPR.13076
173. Arcangeli A, Iorio J, Duranti C. Targeting the hERG1 and β1 integrin complex for cancer treatment. *Expert Opin Ther Targets*. 2024;28(3):145-157. doi:10.1080/14728222.2024.2318449
174. Arcangeli A, Crociani O, Lastraioli E, Masi A, Pillozzi S, Becchetti A. Targeting Ion Channels in Cancer: A Novel Frontier in Antineoplastic Therapy. *Curr Med Chem*. 2008;16(1):66-93. doi:10.2174/092986709787002835
175. Duranti C, Iorio J, Lottini T, et al. Harnessing the hERG1/β1 Integrin Complex via a Novel Bispecific Single-chain Antibody: An Effective Strategy against Solid Cancers. *Mol Cancer Ther*. 2021;20(8):1338-1350. doi:10.1158/1535-7163.MCT-20-1111
176. Xie D, Xie K. Pancreatic cancer stromal biology and therapy. *Genes Dis*. 2015;2(2):133. doi:10.1016/J.GENDIS.2015.01.002
177. She X, Xu J, Zhang H, et al. ETHE1 dampens colorectal cancer angiogenesis by promoting TC45 Dephosphorylation of STAT3 to inhibit VEGF-A expression. *Cell Death & Disease 2024 15:8*. 2024;15(8):1-14. doi:10.1038/s41419-024-07021-w
178. Becchetti A, Crescioli S, Zanieri F, et al. The conformational state of hERG1 channels determines integrin association, downstream signaling, and cancer progression. *Sci Signal*. 2017;10(473). doi:10.1126/SCISIGNAL.AAF3236/SUPPL_FILE/AAF3236_SM.PDF

179. Lastraioli E, Perrone G, Sette A, et al. hERG1 channels drive tumour malignancy and may serve as prognostic factor in pancreatic ductal adenocarcinoma. Published online 2015. doi:10.1038/bjc.2015.28
180. Duranti C, Iorio J, Lottini T, et al. Harnessing the hERG1/b1 integrin complex via a novel bispecific single-chain antibody: An effective strategy against solid cancers. *Mol Cancer Ther*. 2021;20(8):1338-1350. doi:10.1158/1535-7163.MCT-20-1111/673414/AM/HARNESSING-THE-HERG1-1-INTEGRIN-COMPLEX-VIA-A
181. Lottini T, Duranti C, Iorio J, et al. Combination Therapy with a Bispecific Antibody Targeting the hERG1/β1 Integrin Complex and Gemcitabine in Pancreatic Ductal Adenocarcinoma. *Cancers (Basel)*. 2023;15(7). doi:10.3390/cancers15072013
182. Perez VM, Kearney JF, Yeh JJ. The PDAC Extracellular Matrix: A Review of the ECM Protein Composition, Tumor Cell Interaction, and Therapeutic Strategies. *Front Oncol*. 2021;11. doi:10.3389/FONC.2021.751311
183. Zhang T, Ren Y, Yang P, Wang J, Zhou H. Cancer-associated fibroblasts in pancreatic ductal adenocarcinoma. *Cell Death & Disease 2022 13:10*. 2022;13(10):1-11. doi:10.1038/s41419-022-05351-1
184. Fan F, Samuel S, Gaur P, et al. Chronic exposure of colorectal cancer cells to bevacizumab promotes compensatory pathways that mediate tumour cell migration. *Br J Cancer*. Published online 2011. doi:10.1038/bjc.2011.81
185. Arjaans M, Munnink THO, Oosting SF, et al. Bevacizumab-induced normalization of blood vessels in tumors hampers antibody uptake. *Cancer Res*. 2013;73(11):3347-3355. doi:10.1158/0008-5472.CAN-12-3518
186. Atkins MB, Tannir NM. Current and emerging therapies for first-line treatment of metastatic clear cell renal cell carcinoma. *Cancer Treat Rev*. 2018;70:127-137. doi:10.1016/J.CTRV.2018.07.009
187. Hubrecht RC, Carter E. The 3Rs and Humane Experimental Technique: Implementing Change. *Animals (Basel)*. 2019;9(10):754. doi:10.3390/ANI9100754
188. Lenggenhager D, Amrutkar M, Sántha P, et al. Commonly Used Pancreatic Stellate Cell Cultures Differ Phenotypically and in Their Interactions with Pancreatic Cancer Cells. *Cells*. 2019;8(1):23. doi:10.3390/CELLS8010023
189. Crociani O, Lastraioli E, Boni L, et al. hERG1 channels regulate VEGF-A secretion in human gastric cancer: clinicopathological correlations and therapeutical implications. *Clin Cancer Res*. 2014;20(6):1502-1512. doi:10.1158/1078-0432.CCR-13-2633
190. Garcia J, Hurwitz HI, Sandler AB, et al. Bevacizumab (Avastin®) in cancer treatment: A review of 15 years of clinical experience and future outlook. *Cancer Treat Rev*. 2020;86:102017. doi:10.1016/J.CTRV.2020.102017
191. Keša P, Pokorná E, Grajciarová M, et al. Quantitative In Vivo Monitoring of Hypoxia and Vascularization of Patient-Derived Murine Xenografts of Mantle Cell Lymphoma Using Photoacoustic and Ultrasound Imaging. *Ultrasound Med Biol*. 2021;47(4):1099-1107. doi:10.1016/j.ultrasmedbio.2020.12.010
192. Garcia J, Hurwitz HI, Sandler AB, et al. Bevacizumab (Avastin®) in cancer treatment: A review of 15 years of clinical experience and future outlook. *Cancer Treat Rev*. 2020;86:102017. doi:10.1016/j.ctrv.2020.102017